

Quarterly Technical Report

Solid State Research

1990:4

Lincoln Laboratory

MASSACHUSETTS INSTITUTE OF TECHNOLOGY

LEXINGTON, MASSACHUSETTS



Prepared under Air Force Contract F19628-90-C-0002.

Approved for public release; distribution is unlimited.

ADA238427

This report is based on studies performed at Lincoln Laboratory, a center for research operated by Massachusetts Institute of Technology. The work was sponsored by the Department of the Air Force under Contract F19628-90-C-0002.

This report may be reproduced to satisfy needs of U.S. Government agencies.

The ESD Public Affairs Office has reviewed this report, and it is releasable to the National Technical Information Service, where it will be available to the general public, including foreign nationals.

This technical report has been reviewed and is approved for publication.

FOR THE COMMANDER

Hugh L. Southall

Hugh L. Southall, Lt. Col., USAF
Chief, ESD Lincoln Laboratory Project Office

Non-Lincoln Recipients

PLEASE DO NOT RETURN

Permission is given to destroy this document
when it is no longer needed.

MASSACHUSETTS INSTITUTE OF TECHNOLOGY
LINCOLN LABORATORY

SOLID STATE RESEARCH

QUARTERLY TECHNICAL REPORT

1 AUGUST — 31 OCTOBER 1990

ISSUED 5 APRIL 1991

Approved for public release; distribution is unlimited.

ABSTRACT

This report covers in detail the research work of the Solid State Division at Lincoln Laboratory for the period 1 August through 31 October 1990. The topics covered are Electrooptical Devices, Quantum Electronics, Materials Research, Submicrometer Technology, Microelectronics, and Analog Device Technology. Funding is provided primarily by the Air Force, with additional support provided by the Army, DARPA, Navy, SDIO, NASA, and DOE.

TABLE OF CONTENTS

Abstract	iii
List of Illustrations	vii
List of Tables	xiii
Introduction	xv
Reports on Solid State Research	xix
Organization	xxvii
 1. ELECTROOPTICAL DEVICES	 1
1.1 Microchannel Heat Sink with Alternate Directions of Water Flow in Adjacent Channels	1
1.2 Studies of Multiple Quantum Wells Produced by Growth Interruption	5
1.3 Measurements of Trimethylindium Source Efficiency and Stability	9
 2. QUANTUM ELECTRONICS	 17
2.1 Fundamental Linewidth of Microchip Lasers	17
2.2 Q-Switched Microchip Lasers	18
2.3 Polarization Switching of Microchip Lasers	21
2.4 Frequency-Modulated Nd:YAG Laser	23
2.5 Room-Temperature InGaAs-Pumped Yb:YAG Laser	27
2.6 Single-Transverse-Mode Optically Pumped GaAs Laser with 500-W Peak Power	29
2.7 Efficient Coupling of Multiple High-Power Diode Laser Arrays into a Multimode Optical Fiber	31
 3. MATERIALS RESEARCH	 37
3.1 AlInGaAs/AlGaAs Separate-Confinement Heterostructure Strained Single-Quantum-Well Diode Lasers	37
3.2 Time Dependence of AlGaAs MBE Growth Rates Determined by Frequency-Domain Analysis of RHEED Oscillation Data	41
 4. SUBMICROMETER TECHNOLOGY	 47
4.1 Diffusion Processes During Resist Silylation	47
4.2 Excimer-Laser-Induced Changes in Fused Silica	51
 5. HIGH SPEED ELECTRONICS	 57
5.1 Quasioptical Locking of a Millimeter-Wave Resonant-Tunneling Diode Oscillator	57

6.	MICROELECTRONICS	61
6.1	Reduction of Trapping Effects at Low Signal Levels in a Buried-Channel CCD Imager	61
6.2	Quantum-Efficiency Model for a Back-Illuminated CCD Imager	64
7.	ANALOG DEVICE TECHNOLOGY	71
7.1	Surface Impedance Measurements of $\text{YBa}_2\text{Cu}_3\text{O}_{7-x}$ Thin Films in Stripline Resonators	71
7.2	High-Temperature Superconductive Chirp Filter	74
7.3	Serial-Parallel-Serial CCD for High-Speed Signal Acquisition	78

LIST OF ILLUSTRATIONS

Figure No.	Page
1-1 Alternate channel flow design. (a) Schematic of silicon microchannel fins showing dimensions and coolant flow directions. (b) Schematic of manifold plate showing alignment with microchannels and inlet and outlet plenums.	1
1-2 Experimental and theoretical temperature profiles for ACF heat sinks at two flow conditions together with the results for conventional flow in one direction through half of the channels.	3
1-3 Calculated temperature distributions for a 10×10 -cm heat sink with 100-W/cm^2 heat flux. (a) Streamwise profiles of heat sink surface temperature rise and average water temperature rise above the inlet water temperature. (b) Flux plot for a fin at the inlet/outlet position showing isotherms and adiabats. The inlet and outlet water temperatures T_1 and T_2 and the heat sink surface temperature T_s directly above the fin are indicated. Isotherms are shown in increments of 0.25°C .	4
1-4 Simulated (004) rocking curve for a ten-period structure, with each unit consisting of a $500\text{-}\text{\AA}$ GaInP layer and a $3\text{-}\text{\AA}$ InP layer. For visualization reasons, the composition of the GaInP is chosen to give a slight mismatch from the GaAs substrate.	6
1-5 Rocking curve of a sample grown with ten periodic interruptions to GaInP growth. The PH_3 flow was maintained during the 2-s interruption. Two separate peaks due to the GaInP in a buffer layer and in the interrupted-growth layer complicate the curve, but there is no evidence of the periodic structure attributable to an MQW.	7
1-6 Photoluminescence at room temperature from growth-interrupted structures. The solid curve is for the structure of Figure 1-5 and shows only a peak attributable to GaInP and a very weak peak due to the GaAs substrate. The dashed curve is for the sample of Figure 1-7 and shows a strong peak at 1.40 eV .	7
1-7 Rocking curve of a sample grown with ten periodic interruptions to GaInP growth. During the 6-s interruptions the flow sequence was 2-s PH_3 , 2-s AsH_3 , 2-s PH_3 . The rocking curve shows evidence of an MQW with a period of $\sim 600\text{ \AA}$.	8
1-8 Rocking curve of sample grown with ten periodic interruptions to InP growth. During the 6-s interruptions the flow sequence was 2-s PH_3 , 2-s AsH_3 , 2-s PH_3 . The rocking curve shows evidence of an MQW with a period of $\sim 450\text{ \AA}$. Here, 0 arc sec corresponds to the (004) Bragg angle of InP, 31.7° . The x-ray intensity pattern is simpler than that in Figure 1-7 because, other than the interfacial layers, the entire structure including the substrate is InP.	8

Figure No.		Page
1-9	Schematic of TMI source plumbing with specially modified three- and four-way valves for leak testing and purging. The three- and four-way valves are indicated by A and B, respectively.	10
1-10	Source efficiency versus flow rate for three different TMI source cylinders at 25°C in a typical OMVPE growth run. The small decrease in source output for cylinder 2 gives rise to a change in the unstrained $\text{Ga}_{0.51}\text{In}_{0.49}\text{P}$ lattice parameter of $\Delta a/a = -4 \times 10^{-3}$.	12
1-11	Double-crystal x-ray diffraction for 1.2- μm -thick $\text{Ga}_{0.51}\text{In}_{0.49}\text{P}$ epilayers on GaAs substrates grown with stable (solid curve) and unstable (dashed curve) TMI sources. The fluctuations for the unstable source represent a change in the unstrained lattice parameter of $\Delta a/a = 3 \times 10^{-4}$ to 2×10^{-3} .	13
1-12	Time to reach steady-state TMI concentration versus flow rate for a TMI source temperature of 25°C. Cylinder 6 with a volume of 175 cm^3 stabilizes more rapidly than cylinder 4 with a volume of 200 cm^3 . Approximately 20 cylinder volume changes ($\sim 4000 \text{ cm}^3$) are required to reach steady state. The data point (+) represents the total time to reach steady state when the carrier gas is flowed through cylinder 4 at 500 sccm for 10 min and the rate is then dropped to 50 sccm.	14
2-1	Reflectivity of an etalon as a function of frequency. The potential lasing wavelengths of a microchip laser (determined by the cavity modes) are indicated by the tic marks at the top of the figure. For the present device, they are spaced by $\sim 127 \text{ GHz}$. The length of the etalon has been chosen so that its free spectral range is the same as the mode spacing of the microchip laser. The etalon can be tuned to be highly transmitting (solid curve) or highly reflecting (dashed curve) at the potential lasing frequencies of the microchip laser.	19
2-2	Cross section of a piezoelectrically Q-switched microchip laser. In these experiments the Nd:YAG crystal is $0.65 \times 1.0 \times 1.0 \text{ mm}$, and the total distance between the pump mirror and the discrete partially reflecting mirror is $\sim 1.8 \text{ mm}$. The piezoelectric actuator is 2.5 mm thick and has an outer diameter of 20 mm.	19
2-3	Output obtained from a 1.064- μm Q-switched Nd:YAG microchip laser showing (a) a train of pulses and (b) one pulse on an expanded time scale.	20
2-4	Illustration of an all-solid-state polarization-switchable microchip laser. Typical dimensions for such a device would be $1 \times 1 \times 2 \text{ mm}$, with the longest dimension corresponding to the total cavity length.	22
2-5	Traces showing (top) a square wave applied to the polarization-switchable microchip laser and (bottom) the intensity of its output in one polarization.	22

Figure No.		Page
2-6	Traces showing (top) a pseudorandom binary waveform applied to the polarization-switchable microchip laser and (bottom) the intensity of its output in one polarization.	23
2-7	(a) High-voltage step applied to the LiTaO ₃ crystal. The voltage change is 200 V and the electrical rise time is 0.5 ns. (b) Beat signal obtained in heterodyning the frequency-modulated Nd:YAG laser with a Nd:YAG local oscillator. Initially, the two lasers are offset by 1.7 GHz. The voltage step gives rise to a frequency difference of 550 MHz. The undulation of the trace is caused by noise pickup from the pulser.	24
2-8	Schematic of an experiment to measure the linearity of the voltage-to-frequency conversion. The heterodyne signal of a 500-MHz linearly frequency-chirped Nd:YAG laser with a stable local oscillator is compressed with a SAW device to generate a ~ 2.5-ns, 1.3-GHz pulse. The output is mixed to zero frequency, amplified, and filtered.	25
2-9	Compression of a 500-MHz linearly frequency-chirped heterodyne signal. (a) Direct output from the SAW device demonstrating 2.5-ns FWHM pulse width, but with large sidelobes. (b) Output after frequency mixing to dc, amplifying, and filtering. This trace shows broadening and sidelobe rejection caused by the limited bandwidth of the amplifier. The sidelobes are -30 dB of the main peak. The FWHM pulse width is 4 ns.	26
2-10	Diagram of the diode-pumped Yb:YAG laser.	28
2-11	Output power versus input power for the monolithic Yb:YAG laser pumped by a Ti:Al ₂ O ₃ laser and an InGaAs diode laser. The solid line is from the quasi-three-level laser model.	28
2-12	Diagram of a folded-cavity GaAs disk laser.	30
2-13	GaAs laser output power versus input pump power for a 120- μ m-diam. pump spot. Peak power is derived using the measured pulse duration.	30
2-14	(a) Intensity profile of output beam. (b) Cross-sectional intensity profile in the vertical and horizontal axes through the beam center. The dotted curves are Gaussian fits.	32
2-15	Output spectra of the GaAs laser with and without an etalon.	33
2-16	Schematic of a multiple-disk laser.	33
2-17	Schematic of multiple diode laser arrays coupled into a multimode fiber in planes (a) perpendicular and (b) parallel to the junctions of the diode laser arrays.	34
3-1	Dependence on x and y of wavelength corresponding to calculated electron-hole-transition energy for 10-nm-thick Al _{y} In _{x} Ga _{1-x-y} As quantum wells with Al _{0.3} Ga _{0.7} As confining layers.	38

Figure

No.		Page
3-2	Schematic structure and energy diagram of AlInGaAs/AlGaAs SCH SQW diode laser.	39
3-3	Threshold current density J_{th} of GaAs/AlGaAs, Al _{0.18} In _{0.20} GaAs _{0.62} /AlGaAs, and In _{0.2} Ga _{0.8} As/AlGaAs diode lasers as a function of reciprocal cavity length $1/L$.	40
3-4	Reciprocal differential quantum efficiency η_d^{-1} as a function of cavity length L . The solid line is a least-squares fit.	40
3-5	RHEED oscillation frequency versus substrate temperature for growth of AlGaAs. For data represented by circles and squares, frequencies were obtained by frequency-domain and time-domain analyses, respectively.	42
3-6	RHEED oscillation frequency versus substrate temperature for growth of AlGaAs. For data represented by circles and squares, frequencies were obtained by frequency-domain analysis of data collected for 0 to 30 s and 10 to 30 s, respectively, after opening the Al and Ga source shutters.	43
3-7	RHEED oscillation frequency versus time following source-shutter opening for AlGaAs growth at substrate temperatures from 520 to 760°C. Frequencies were obtained by frequency-domain analysis of data collected for 5-s periods.	44
4-1	Schematic of silicon profiles for negative- and positive-tone silylation processes. Regions of crosslinking are shown by diagonal shading, and the silylated areas are represented by vertical shading.	48
4-2	Scanning Auger depth-profile of a grating structure with 5- μ m lines and spaces patterned in FSC resist, exposed at 100 mJ cm ⁻² , and silylated at 100°C for 1 min at 10-Torr pressure. The crosslinked region, denoted by crosshatching, extends 75 nm into the film.	48
4-3	Schematic of swelling constraints imposed by the exposed crosslinked regions. The filled areas represent the crosslinked regions and the diagonal shading denotes the swollen silylated areas.	49
4-4	Comparison of Si yield from RBS spectra for a grating structure with 3- μ m lines and spaces patterned in SAL 601, exposed at doses from 10 to 100 mJ cm ⁻² , and silylated at 90°C for 1 min at 10-Torr pressure. Schematic diagram of diffusion profile based on RBS interpretation is shown at the right, with the diagonal shading denoting crosslinking, the crosshatching representing a higher degree of crosslinking, and the vertical shading denoting silylated areas.	50
4-5	Excimer-laser-induced absorption spectrum in fused silica and (inset) birefringence as evidenced by the transmitted 633-nm light when the sample was placed between two crossed linear polarizers. Note that the birefringent zone surrounds the excimer laser spot.	51

Figure No.		Page
4-6	PMI output mapping the transmission of a 193-nm-irradiated sample of fused silica: (a) top and (b) three-dimensional views of the sample and (c) a two-dimensional trace. Compaction in the $\sim 5 \times 8$ -mm laser spot is clearly seen (the four blank circles are absorptive dots drawn on the sample for visual demarcation of the laser spot).	52
4-7	Interferometrically measured optical path difference versus ~ 215 -nm absorbance for nine samples of fused silica. All samples were irradiated at 193 nm, 78 mJ cm^{-2} per pulse with 2×10^6 pulses. They differ in growth conditions and post-growth annealing conditions. The material processing can have a significant effect on UV absorbance but much less influence on the compaction as measured with an interferometer.	54
5-1	Schematic diagram of quasioptical resonant-tunneling diode oscillator designed to operate in the 100-GHz region.	57
5-2	(a) Power spectrum of the quasioptical oscillator with and without the semiconfocal open resonator. (b) Horizontal expansion of the power spectrum measured with the semiconfocal open resonator.	59
6-1	Schematic of the cross section of (a) conventional and (b) modified CCD channels and the corresponding potential profiles. Shown in (b) is a concept for reducing trapping effects at low signal levels in a CCD by adding a narrow implant along the channel center to confine the charge packet to a reduced volume.	61
6-2	Measured data showing the effects of a narrow trough in reducing the charge-transfer inefficiency due to bulk trapping. Measurements were made both before and after bombardment with high-energy protons.	62
6-3	Design of the trough implant mask in the region of the CCD where the frame store joins the output register.	63
6-4	Cross-sectional diagram of the band structure of a back-illuminated CCD imager.	64
6-5	Measurements of representative doping profile of p^+ surface layer.	65
6-6	Comparison of calculated and measured QE for two different devices, using S_n as a fitting parameter and $X_a \approx 0.1 \text{ mm}$.	68
6-7	Plot of calculated QE versus S_n and X_a .	68
7-1	Measured and calculated values of resonant frequency of the fundamental mode of the resonator versus temperature for sputtered film 3. The calculated values use the two-fluid model. The best fit is obtained with $T_c = 86.4 \text{ K}$ and $\lambda(0) = 0.167 \text{ }\mu\text{m}$.	72
7-2	Surface resistance versus peak RF magnetic field for four different films as indicated. Lines have been drawn to connect the points. For sputtered films 2 and 3, $f = 1.5 \text{ GHz}$. For sputtered film 1 and the postannealed film, $f = 1.6 \text{ GHz}$. All measurements were made at 4.2 K .	73

Figure No.		Page
7-3	Photograph of a superconductive stripline chirp filter. The filters were fabricated on 2-in.-diam. LaAlO_3 substrates using either $\text{YBa}_2\text{Cu}_3\text{O}_{7-x}$ signal lines and silver ground planes or niobium signal lines and niobium ground planes.	75
7-4	Comparison of the designed and measured transmission response of the superconductive chirp filter. The designed response was calculated assuming lossless transmission lines. The measured transmission response at 4.2 K is shown for both $\text{YBa}_2\text{Cu}_3\text{O}_{7-x}$ and niobium versions of the filter.	76
7-5	(a) Downchirp response and (b) upchirp response to a 250-mV step input measured at 4.2 K for the $\text{YBa}_2\text{Cu}_3\text{O}_{7-x}$ filter.	77
7-6	Serial-parallel-serial CCD memory.	79
7-7	Schematic diagram illustrating the operation of the CCD analog buffer memory and the experimental results for a sampling rate of 280 MHz.	80

LIST OF TABLES

Table No.		Page
1-1	Summary of TMI Source Cylinder Characteristics	11
2-1	Power and Efficiency Obtained with Coupling of Diode Laser Arrays to a Fiber	35
6-1	Parameters Used to Calculate Total Internal Quantum Efficiency	67
7-1	Measured Penetration Depth for Sputtered Films	72

INTRODUCTION

1. ELECTROOPTICAL DEVICES

A new microchannel heat sink design has been demonstrated that uses alternate directions of flow of coolant water in adjacent channels. The spatial variation in heat sink temperature obtained was considerably smaller than that of an otherwise equivalent unidirectional flow design.

X-ray and photoluminescence characterization of structures grown with periodic interruptions has provided information about the chemistry of growth interfaces. There is no evidence of In accumulation at the surface during GaInP growth, but it was shown that As can rapidly substitute for P at GaInP/GaAs and InP/InGaAs interfaces.

An ultrasonic monitor has been used to measure the steady-state indium concentration of trimethylindium source cylinders from several different suppliers under typical organometallic vapor phase epitaxy growth conditions. Large source-to-source variations and sudden instabilities of concentration were found, which complicate the growth of $\text{In}_x\text{Ga}_{1-x}\text{As}_y\text{P}_{1-y}$ alloys lattice matched to InP or GaAs.

2. QUANTUM ELECTRONICS

The contributions of spontaneous emission and of thermal fluctuations of cavity length to the fundamental linewidth of microchip lasers have been studied. Thermal fluctuations of cavity length result in a Gaussian power spectrum that is dominant near line center, while spontaneous emission results in a Lorentzian spectrum that determines the shape of the spectral wings.

With the use of a novel Q-switching technique, 6-ns output pulses have been produced from a single-mode Nd:YAG microchip laser pumped with 120 mW of CW optical power. Computer modeling indicates that diode-laser-pumped Nd:YAG microchip lasers can be Q-switched to produce pulses as short as 250 ps, with peak powers of several kilowatts.

A polarization-switchable microchip laser has been achieved by the introduction of a birefringent element between the two partially reflecting mirrors of the tunable etalon in a Q-switched device. The switching time obtained was $< 5 \mu\text{s}$, and much faster times are possible.

Tuning sensitivity of 12 MHz/V has been measured in a frequency-modulated, single-mode Nd:YAG laser constructed with a LiTaO_3 electrooptic phase modulator incorporating acoustic damping. A frequency excursion of 1 GHz was generated with a rise time of $< 1 \text{ ns}$, and the nonlinearity of the voltage-to-frequency conversion for a 570-ns-long, 42-V sawtooth waveform was < 0.5 percent.

An efficient room-temperature ytterbium-doped YAG laser has been developed that operates at $1.03 \mu\text{m}$ and is pumped by an InGaAs strained-layer diode laser emitting at 968 nm. This Yb:YAG laser, which is made using a monolithic cavity design, has an external slope efficiency of 25 percent with 23 mW of output power obtained for 430 mW of incident pump power.

An optically pumped GaAs disk laser has been demonstrated that produces 500-W peak power in a circularly symmetric lowest-order transverse mode, which is 2 orders of magnitude greater peak power than that previously reported for semiconductor lasers. Diode-laser-array pumping was simulated using a gain-switched $\text{Ti:Al}_2\text{O}_3$ laser with a 4-kHz repetition rate; the pump pulse duration was ~ 38 ns, resulting in quasi-CW pumping conditions.

Five high-power diode laser arrays have been coupled with 68 percent efficiency and 2.6-W output through an optical fiber having a $48\text{-}\mu\text{m}$ core-diameter/numerical-aperture product. An increase in the output power should be achievable from the same fiber using more diode arrays, and improvements in the optical system could lead to an efficiency > 80 percent.

3. MATERIALS RESEARCH

Separate-confinement heterostructure diode lasers with a strained $\text{Al}_{0.18}\text{In}_{0.20}\text{Ga}_{0.62}\text{As}$ single-quantum-well active layer and AlGaAs confining layers have been fabricated from structures grown on GaAs substrates by low-pressure organometallic vapor phase epitaxy. Preliminary experiments show that these devices, which have an emission wavelength of 814 nm, are much more reliable than lasers with lattice-matched AlGaAs active layers that emit at about this wavelength.

Frequency-domain techniques have been applied to the analysis of reflection high-energy electron diffraction oscillation data taken during molecular beam epitaxy growth of AlGaAs layers at substrate temperatures from 580 to 790°C and at various V/III ratios. For temperatures above 700°C, the growth rate immediately after opening the Ga and Al source shutters exceeds the steady-state value by an amount that increases with increasing temperature.

4. SUBMICROMETER TECHNOLOGY

The diffusion characteristics of the silylating agent in 193-nm positive-tone surface imaging have been determined. It was shown that proximity effects caused by crosslinking in exposed areas influence the degree of silylation in unexposed areas, thereby affecting the process latitude of this lithographic technique.

Excimer laser irradiation of fused silica has been shown to induce formation of point defects and also changes in density and refractive index. These two types of defects are proportional to each other for any given material, but the constant of proportionality depends strongly on the specific growth and annealing steps.

5. HIGH SPEED ELECTRONICS

A semiconfocal open-cavity resonator has been used to lock a resonant-tunneling diode oscillator at a frequency of 103 GHz. The high quality factor of the open cavity resulted in a locked-oscillator linewidth of 40 kHz, which is about 250 times narrower than the linewidth of previous resonant-tunneling oscillators that used only waveguide resonators.

6. MICROELECTRONICS

Reduced trapping effects have been achieved at low signal levels in a buried-channel charged-coupled device (CCD) by adding a narrow potential well along the center of the CCD channel, thereby confining the charge to a smaller volume. A tenfold decrease in trapping effects was observed in a proton-irradiated device with a 2- μm narrow well in the center of a 21- μm -wide channel.

An analytical model has been developed to predict the quantum efficiency of a back-illuminated CCD imager with a shallow p^+ layer at the back surface, with the surface recombination velocity at the illuminated surface used as the adjustable parameter to obtain a good fit between calculations and measurements. The model suggests a strong dependence of the quantum efficiency on the surface recombination velocity and only a weak dependence on the depth of the p^+ surface layer.

7. ANALOG DEVICE TECHNOLOGY

Measurements of the magnetic penetration depth λ of $\text{YBa}_2\text{Cu}_3\text{O}_{7-x}$ thin films have been made using a stripline resonator. The RF magnetic field dependence of the surface resistance $R_s(H_{\text{rf}})$ of $\text{YBa}_2\text{Cu}_3\text{O}_{7-x}$ films has also been measured, and the values of λ and $R_s(H_{\text{rf}})$ have been related to the conditions used in the film deposition.

A superconductive stripline chirp filter with 2.6-GHz bandwidth has been demonstrated using tapped delay lines patterned from a postannealed thin film of $\text{YBa}_2\text{Cu}_3\text{O}_{7-x}$ on a 2-in.-diam. LaAlO_3 substrate. The filter has 8 ns of dispersive delay and 12 ns of total delay, including impedance transformers, and the total $\text{YBa}_2\text{Cu}_3\text{O}_{7-x}$ line length required is 0.7 m.

The performance of a CCD-based analog memory designed for high-speed data acquisition has been evaluated. The chip has a 128×128 serial-parallel-serial architecture and can sample incoming data at a maximum rate of 280 MHz.

REPORTS ON SOLID STATE RESEARCH

1 August Through 31 October 1990

PUBLICATIONS

High-Performance Optical Analog Links Using External Modulators	G.E. Betts L.M. Johnson C.H. Cox III	<i>Proceedings DoD Fiber Optics Conference '90</i> (Armed Forces Communications and Electronics Association, Fairfax, Va., 1990), p. 309
Room-Temperature Continuous Operation of GaAs/AlGaAs Lasers Grown on Si by Organometallic Vapor-Phase Epitaxy	H.K. Choi C.A. Wang J.C.C. Fan*	<i>J. Appl. Phys.</i> 68 , 1916 (1990)
External-Cavity Coherent Operation of InGaAsP Buried-Heterostructure Laser Array	V. Diadiuk Z.L. Liao J.N. Walpole J.W. Caunt R.C. Williamson	<i>Proc. SPIE</i> 1219 , 366 (1990)
High-Power Hybrid Two-Dimensional Surface-Emitting AlGaAs Diode Laser Arrays	J.P. Donnelly K. Rauschenbach C.A. Wang R.J. Bailey J.N. Walpole L.J. Missaggia J.D. Woodhouse H.K. Choi F.J. O'Donnell V. Diadiuk	<i>Proc. SPIE</i> 1219 , 255 (1990)
Efficient GaInAsSb/AlGaAsSb Diode Lasers Emitting at 2.29 μm	S.J. Eglash H.K. Choi	<i>Appl. Phys. Lett.</i> 57 , 1292 (1990)
Numerical Modeling of Energy-Beam-Induced Localized Melting in Thin Si Films	J.S. Im J.D. Lipman* I.N. Miaoulis* C.K. Chen C.V. Thompson*	<i>Materials Research Society Symposium Proceedings</i> 157 (Materials Research Society, Pittsburgh, 1990), p. 455

*Author not at Lincoln Laboratory.

Measurement of Third-Order Optical Nonlinear Susceptibility Using Four-Wave Mixing in a Single-Mode Ridge Waveguide	H.Q. Le W.D. Goodhue K. Rauschenbach	<i>Opt. Lett.</i> 15 , 1126 (1990)
Fabrication of Microlenses in Compound Semiconductors and Monolithic Integration with Diode Lasers	Z.L. Liao J.N. Walpole V. Diadiuk D.E. Mull L.J. Missaggia	<i>Proc. SPIE</i> 1219 , 276 (1990)
Measurement of the Surface Resistance of $\text{YBa}_2\text{Cu}_3\text{O}_{7-x}$ Thin Films Using Stripline Resonators	D.E. Oates A.C. Anderson P.M. Mankiewich*	<i>J. Superconduct.</i> 3 , 251 (1990)
Amorphous Carbon Films as Planarization Layers Deposited by Plasma-Enhanced Chemical Vapor Deposition	S.W. Pang M.W. Horn	<i>IEEE Electron Device Lett.</i> 11 , 391 (1990)
High- T_c Superconducting Analog Circuits	R.W. Ralston	In <i>Advances in Superconductivity II: Proceedings of the 2nd International Symposium on Superconductivity</i> , T. Ishiguro and K. Kajimura, eds. (Springer-Verlag, Tokyo, 1990), p. 35
Optical Interconnections in Digital Systems—Status and Prospects	D.Z. Tsang	<i>Opt. Photon. News</i> 1 (10), 23 (1990)
Hydrogen Annealing of PtSi-Si Schottky Barrier Contacts	B-Y. Tsaur J.P. Mattia C.K. Chen	<i>Appl. Phys. Lett.</i> 57 , 1111 (1990)
IrSi Schottky-Barrier Infrared Detectors with Wavelength Response Beyond 12 μm	B-Y. Tsaur C.K. Chen B.A. Nechay	<i>IEEE Electron Device Lett.</i> 11 , 415 (1990)
High-Power Surface-Emitting Diode Lasers	J.N. Walpole	<i>Proceedings DoD Fiber Optics Conference '90</i> (Armed Forces Communications and Electronics Association, Fairfax, Va., 1990), p. 145
High- T_c Superconducting Thin Films for Microwave Applications	R.S. Withers A.C. Anderson D.E. Oates	<i>Solid State Technol.</i> 33 (8), 83 (1990)

*Author not at Lincoln Laboratory.

ACCEPTED FOR PUBLICATION

20-GHz Optical Analog Link Using an External Modulator	G.E. Betts C.H. Cox III K.G. Ray	<i>IEEE Photon. Technol. Lett.</i>
Reduced-Confinement GaAlAs Tapered Waveguide Antennas for Enhanced Far-Field Beam Directionality	D.E. Bossi W.D. Goodhue L.M. Johnson R.H. Rediker	<i>IEEE J. Quantum Electron.</i>
Oscillations up to 712 GHz in InAs/AlSb Resonant-Tunneling Diodes at Room Temperature	E.R. Brown J.R. Söderström* C.D. Parker L.J. Mahoney K.M. Molvar T.C. McGill*	<i>Appl. Phys. Lett.</i>
High-Frequency Resonant-Tunneling Oscillators	E.R. Brown C.D. Parker A.R. Calawa M.J. Manfra C.L. Chen L.J. Mahoney W.D. Goodhue J.R. Söderström* T.C. McGill*	<i>Microwave Opt. Technol. Lett.</i>
Effects of Interface Traps on the Transconductance and Drain Current of InP MISFET's	C.L. Chen A.R. Calawa W.E. Courtney L.J. Mahoney S.C. Palmateer M.J. Manfra M.A. Hollis	<i>IEEE Trans. Electron Devices</i>
Starting Dynamics of Additive Pulse Mode-Locking in the Ti:Al ₂ O ₃ Laser	J. Goodberlet* J. Wang* J.G. Fujimoto* P.A. Schulz	<i>Opt. Lett.</i>
Silylation Processes Based on Ultraviolet Laser-Induced Crosslinking	M.A. Hartney M. Rothschild R.R. Kunz D.J. Ehrlich D.C. Shaver	<i>J. Vac. Sci. Technol. B</i>

*Author not at Lincoln Laboratory.

Plasma-Deposited Organosilicon Thin Films as Dry Resists for Deep Ultraviolet Lithography	M.W. Horn S.W. Pang M. Rothschild	<i>J. Vac. Sci. Technol. B</i>
Linearization of an Interferometric Modulator at Microwave Frequencies by Polarization Mixing	L.M. Johnson H.V. Roussell	<i>IEEE Photon. Technol. Lett.</i>
Resistivity of Bulk InP	G.W. Iseler	In <i>Properties of Indium Phosphide</i> , J.L. Sears, ed. (INSPEC, Stevenage, Hertfordshire, England)
Polysilyne Thin Films as Resists for Deep Ultraviolet Lithography	R.R. Kunz M.W. Horn R.B. Goodman P.A. Bianconi* D.A. Smith* C.A. Freed*	<i>J. Vac. Sci. Technol. B</i>
Passive Microwave Device Applications of High- T_c Superconducting Thin Films	W.G. Lyons R.S. Withers	<i>Microwave J.</i>
Magneto-optical Study of Donor Level Crossing in Tipped GaAs/(GaAl)As Quantum Wells	E.R. Mueller* W.D. Goodhue D.M. Larsen* J.W. Bales J. Waldman*	<i>Phys. Rev. B</i>
Plasma-Deposited Amorphous Carbon Films as Planarization Layers	S.W. Pang M.W. Horn	<i>J. Vac. Sci. Technol. B</i>
Lateral-Mode Selectivity in External-Cavity Diode Lasers with Residual Facet Reflectivity	W.F. Sharfin A. Mooradian	<i>IEEE J. Quantum Electron.</i>
Growth and Characterization of High-Current Density, High-Speed InAs/AlSb Resonant-Tunneling Diodes	J.R. Söderström* E.R. Brown C.D. Parker L.J. Mahoney J.Y. Yao* T.G. Anderson* T.C. McGill*	<i>Appl. Phys. Lett.</i>

*Author not at Lincoln Laboratory.

Resonant-Tunneling Diode Oscillator
Using a Slot-Coupled Quasioptical
Open Resonator

K.D. Stephan*
E.R. Brown
C.D. Parker
W.D. Goodhue
C.L. Chen
T.C.L.G. Sollner

IEEE Electron. Lett.

The Effects of Spatial Hole Burning
and Energy Diffusion on the Single-
Mode Operation of Standing-Wave
Lasers

J.J. Zayhowski

IEEE J. Quantum Electron.

PRESENTATIONS[†]

Optical Interconnection Applications
of Diode Lasers

D.Z. Tsang

High Power Semiconductor
Laser Amplifiers

C.D. Nabors
R.L. Aggarwal
H.K. Choi
C.A. Wang
A. Mooradian

New Semiconductor Laser
Devices and Applications,
Monterey, California,
1-3 August 1990

Extremely Uniform PtSi Schottky-
Barrier Focal Plane Arrays for
MWIR Imaging Without Correction

B-Y. Tsaur
C.K. Chen
M.J. Cantella
N.C. Davison III
R.G. Schultz

1990 Meeting of the IRIS
Specialty Group on Infrared
Detectors,
Gaithersburg, Maryland,
13-17 August 1990

High-Frequency Applications of
Resonant-Tunneling Devices

T.C.L.G. Sollner
E.R. Brown
C.D. Parker
W.D. Goodhue

Seminar, Institute for
Problems of Microelectronics,
Chernogolovka, USSR,
24 August 1990

MBE Growth of GaInAsSb/AlGaAsSb
Double Heterostructures for Infrared
Diode Lasers

S.J. Eglash
H.K. Choi
G.W. Turner

Application of Frequency-Domain
Analysis to RHEED Oscillation Data:
Time Dependence of AlGaAs Growth
Rates

G.W. Turner
S.J. Eglash

Sixth International Conference
on Molecular Beam Epitaxy,
La Jolla, California,
27-31 August 1990

*Author not at Lincoln Laboratory.

[†]Titles of presentations are listed for information only. No copies are available for distribution.

High Performance Analog Fiber-Optic Links	C.H. Cox III	XXIIIrd General Assembly of URSI, Prague, Czechoslovakia, 28 August–5 September 1990
Superconductive Analog Electronics for Signal Processing Applications	J.B. Green R.S. Withers	NATO Applied Research Workshop on Superconducting Electronics, Capri, Italy, 3-7 September 1990
Mass Transport in Quaternary Materials for Device Applications	J.N. Walpole	Short Course on III-V Quantum Well Lasers and Related Technology, Zurich, Switzerland, 7 September 1990
High-Efficiency, High-Power GaInAsSb/AlGaAsSb Double-Heterostructure Lasers Emitting at 2.3 μm	H.K. Choi S.J. Eglash	12th IEEE International Semiconductor Laser Conference, Davos, Switzerland, 9-13 September 1990
Improved Mass-Transported GaInP/GaAs Lasers	J.N. Walpole S.H. Groves Z.L. Liao S.C. Palmateer D.Z. Tsang	
Quantum-Well Optoelectronic Switching Devices for Optical Information Processing	B.F. Aull K.B. Nichols C. Mchianian	1990 Topical Meeting on Spatial Light Modulators and Applications, Lake Tahoe, Nevada, 10-12 September 1990
A Comparison of the Link Performance of Directly and Externally Modulated Analog Fiber-Optic Links	C.H. Cox III G.E. Betts L.M. Johnson	20th European Microwave Conference, Budapest, Hungary, 10-13 September 1990
High-Dynamic-Range, Low-Noise Analog Optical Links Using External Modulators: Analysis and Demonstration	G.E. Betts L.M. Johnson C.H. Cox III	SPIE OE/FIBERS'90, San José, California, 16-21 September 1990
Integrated-Optical Modulators for Bandpass Analog Links	L.M. Johnson G.E. Betts H.V. Roussell	

Diamond Transistor Performance and
Fabrication

Positive-Tone Silylation Processes
at 193 nm

Analog Signal Correlator Design and
Operation

High- T_c Superconductive Microwave
Filters

High- T_c Superconductive Delay Line
Structures and Signal Conditioning
Networks

Surface Impedance Measurements
of $\text{YBa}_2\text{Cu}_3\text{O}_{7-x}$ Thin Films in
Stripline Resonators

Microwave Applications of High- T_c
Superconductive Thin Films

Off-Axis Magnetron Sputtering of
YBCO Films: The Influence of
Atomic Oxygen

M.W. Geis

M.A. Hartney
M. Rothschild
R.R. Kunz
D.J. Ehrlich
D.C. Shaver

J.B. Green
M. Bhushan

W.G. Lyons
R.R. Bonetti*
A.E. Williams*
P.M. Mankiewich*
M.L. O'Malley*
J.M. Hamm
A.C. Anderson
R.S. Withers
A. Meulenberg*
R.E. Howard*

W.G. Lyons
R.S. Withers
J. M. Hamm
A.C. Anderson
P.M. Mankiewich*
M.L. O'Malley*
R.E. Howard*

D.E. Oates
A.C. Anderson

R.W. Ralston

A.C. Westerheim
L.S. Yu-Jahnes
A.C. Anderson

International Conference on
Electronic Materials 1990,
Newark, New Jersey,
18 September 1990

Microcircuit Engineering 90,
Leuven, Belgium,
18-21 September 1990

Applied Superconductivity
Conference,
Snowmass Village, Colorado,
24-28 September 1990

*Author not at Lincoln Laboratory.

Silylation Processes Based on UV
Laser-Induced Crosslinking

M.A. Hartney
M. Rothschild
R.R. Kunz
D.J. Ehrlich
D.C. Shaver

Seminar, Philips Laboratory,
Eindhoven, The Netherlands,
26 September 1990

Resonant-Tunneling Devices and
Circuits

T.C.L.G. Sollner

GaAs IC Symposium,
New Orleans, Louisiana,
7-10 October 1990

Dry Developed, Plasma Deposited
Organosilicon Resists for Deep
UV Lithography

M.W. Horn
R.R. Paladugu
R.B. Goodman
R.R. Kunz

Photooxidation of σ -Conjugated
Si-Si Network Polymers

R.R. Kunz
M.W. Horn
P.A. Bianconi*
D.A. Smith*
C.A. Freed*

37th American Vacuum Society
National Symposium,
Toronto, Canada,
8-12 October 1990

High-Power Solid-State Laser
Radar Technology

A. Sanchez

First Fire Control Symposium,
U.S. Air Force Academy,
Colorado Springs, Colorado,
24 October 1990

Heat Driven Cryocoolers for
Satellite Bus Use

R.M. Lerner

International Cryocooler
Conference,
Plymouth, Massachusetts,
25-26 October 1990

Diamond Transistors

M.W. Geis

VLSI Seminar, Massachusetts
Institute of Technology,
Cambridge, Massachusetts,
30 October 1990

*Author not at Lincoln Laboratory.

ORGANIZATION

SOLID STATE DIVISION

A.L. McWhorter, *Head*
I. Melngailis, *Associate Head*
E. Stern, *Associate Head*
J.F. Goodwin, *Assistant*

D.J. Ehrlich, *Senior Staff*
N.L. DeMeo, Jr., *Associate Staff*
J.W. Caunt, *Assistant Staff*
K.J. Challberg, *Administrative Staff*

SUBMICROMETER TECHNOLOGY

D.C. Shaver, *Leader*
M. Rothschild, *Assistant Leader*

Astolfi, D.K.	Hartney, M.A.
Craig, D.M.	Horn, M.W.
Dennis, C.L.	Kunz, R.R.
Doran, S.P.	Lyszczarz, T.M.
Efremow, N.N., Jr.	Maki, P.A.
Forte, A.R.	Melngailis, J. [†]
Gajar, S.A.*	Paladugu, R.R.
Geis, M.W.	Sedlacek, J.H.C.
Goodman, R.B.	Uttaro, R.S.

QUANTUM ELECTRONICS

A. Mooradian, *Leader*
P.L. Kelley, *Associate Leader*
A. Sanchez-Rubio, *Assistant Leader*

Aggarwal, R.L.	Jeys, T.H.
Barch, W.E.	Korn, J.A.
Cook, C.C.	Lacovara, P.
Daneu, V.	Le, H.Q.
DeFeo, W.E.	Menyuk, N. [†]
DiCecca, S.	Nabors, C.D.
Dill, C.D., III	Ochoa, J.R.
Fan, T.Y.	Schulz, P.A.
Hancock, R.C.	Seemungal, W.A.
Henion, S.R.	Sullivan, D.J.
Hotaling, T.C.	Wall, K.F.
Hsu, L.*	Zayhowski, J.J.

ELECTRONIC MATERIALS

A.J. Strauss, *Leader*
B-Y. Tsaur, *Associate Leader*

Anderson, C.H., Jr.	Kolesar, D.F.
Button, M.J.	Krohn, L., Jr.
Chen, C.K.	Mastromattei, E.L.
Choi, H.K.	Marino, S.A.
Clark, H.R., Jr.	Mattia, J.P.*
Connors, M.K.	McGilvary, W.L.
Delaney, E.J.	Nitishin, P.M.
Eglash, S.J.	Pantano, J.V.
Fahey, R.E.	Turner, G.W.
Finn, M.C.	Wang, C.A.
Iseler, G.W.	

HIGH SPEED ELECTRONICS

R.A. Murphy, *Leader*
M.A. Hollis, *Assistant Leader*
R.W. Chick, *Senior Staff*

Actis, R.	Lincoln, G.A., Jr.
Bales, J.W.*	Mahoney, L.J.
Barlas, A.D.	Manfra, M.J.
Bergeron, N.J.	Mathews, R.H.
Bozler, C.O.	McIntosh, K.A.
Brown, E.R.	McMorran, R.A.
Calawa, A.R.	McNamara, M.J.
Chen, C.L.	Nichols, K.B.
Clifton, B.J.	Parker, C.D.
Crenshaw, D.L.*	Rabe, S.
Gladden, D.B. [‡]	Rathman, D.D.
Goodhue, W.D.	Smith, F.W., III
Gray, R.V.	Vera, A.

* Research Assistant

[†] Part Time

[‡] Staff Associate

ELECTROOPTICAL DEVICES

R.C. Williamson, *Leader*
D.L. Spears, *Assistant Leader*
R.H. Rediker, *Senior Staff*

Aull, B.F.[‡]
Bailey, R.J.
Barwick, D.S.*
Betts, G.E.
Corcoran, C.J.*
Cox, C.H., III
Diadiuk, V.
Donnelly, J.P.
Ferrante, G.A.
Groves, S.H.
Harman, T.C.
Hovey, D.L.
Johnson, L.M.
Liau, Z.L.
Lind, T.A.

Missaggia, L.J.
Mull, D.E.
O'Donnell, F.J.
Palmacci, S.T.
Palmateer, S.C.
Pheiffer, B.K.*
Rauschenbach, K.
Reeder, R.E.
Roussell, H.V.
Shiple, S.D.*
Tsang, D.Z.
Walpole, J.N.
Woodhouse, J.D.
Yee, A.C.

ANALOG DEVICE TECHNOLOGY

R.W. Ralston, *Leader*
R.S. Withers, *Associate Leader*
T.C.L.G. Sollner, *Assistant Leader*
R.M. Lerner, *Senior Staff*[†]

Anderson, A.C.
Arsenault, D.R.
Bhushan, M.
Boisvert, R.R.
Brogan, W.T.
Denneno, A.P.
Fitch, G.L.
Green, J.B.
Hamm, J.M.
Holtham, J.H.
Lattes, A.L.

Lyons, W.G.
Macedo, E.M., Jr.
Minnick, R.G.
Munroe, S.C.
Oates, D.E.
Sage, J.P.
Seaver, M.M.
Slattery, R.L.
Westerheim, A.C.*
Whitley, D.B.
Yu-Jahnes, L.S.*

MICROELECTRONICS

E.D. Savoye, *Leader*
B.B. Kosicki, *Assistant Leader*

Burke, B.E.
Chiang, A.M.
Chuang, M.L.*
Collins, I.K.
Cooper, M.J.
Daniels, P.J.
Doherty, C.L., Jr.
Dolat, V.S.

Donahue, T.C.
Durant, G.L.
Felton, B.J.
Gregory, J.A.
Huang, C.M.
Hurley, E.T.
Johnson, B.W.
Johnson, K.F.

LaFranchise, J.R.
McGonagle, W.H.
Mountain, R.W.
Percival, K.A.
Pichler, H.H.
Reich, R.K.
Reinold, J.H., Jr.
Young, D.J.

* Research Assistant

† Part Time

‡ Leave of Absence

1. ELECTROOPTICAL DEVICES

1.1 MICROCHANNEL HEAT SINK WITH ALTERNATE DIRECTIONS OF WATER FLOW IN ADJACENT CHANNELS

Microchannel heat sinks have been developed for extraction of waste heat generated by integrated electronic circuits, two-dimensional diode laser arrays, and other electrooptic devices under conditions of high heat flux density [1]-[6]. Very low thermal resistance has been obtained in these heat sinks. Yet, they have the potential problem of an increase in temperature in the streamwise direction due to an approximately linear temperature rise in the coolant as it is heated along the channel length. Reducing this temperature rise by increasing the coolant flow rate increases the mechanical power dissipated by the flowing coolant, which may greatly raise the overall power consumption. A solution to this problem is described here, which provides for alternate water flow directions in adjacent channels. The spatial variation in heat sink temperature for the alternate channel flow (ACF) design is considerably smaller than that of an otherwise equivalent unidirectional flow design.

The ACF heat sink design is illustrated in Figure 1-1. The heat sink is made from a 1.2-mm-thick Si wafer in which thirty-three 0.18-mm-wide, 1-mm-deep microchannels separated by 0.15 mm are cut with a high-speed dicing saw. A schematic end view of a two-microchannel section of the wafer is shown in

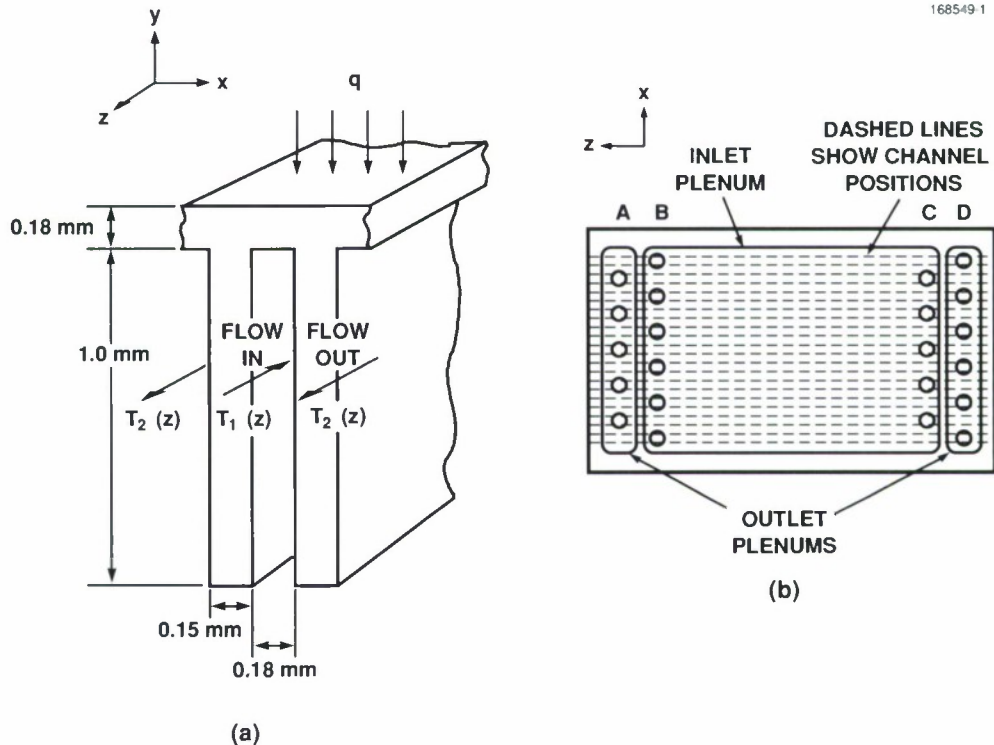


Figure 1-1. Alternate channel flow design. (a) Schematic of silicon microchannel fins showing dimensions and coolant flow directions. (b) Schematic of manifold plate showing alignment with microchannels and inlet and outlet plenums.

Figure 1-1(a). The channel side of the Si wafer is epoxied to a brass manifold plate having 66 holes to direct the flow of water. Figure 1-1(b) is a schematic of the manifold plate, with the dashed lines representing the location of the channels with respect to the 0.3-mm-diam. holes in the plate. For simplicity, only 11 of the 33 channels are shown. Water flows into the microchannels through two columns of holes in the manifold inlet plenum. The water entering the holes in column B exits at column D in one of the outlet plenums, while water entering in column C exits at column A in the opposite outlet plenum. The direction of water flow alternates from channel to channel. Since the unheated inlet water and the maximally heated outlet water are only a channel separation (0.15 mm) apart, the coolant temperature averaged across two channels is nearly constant over the entire heat sink area. Columns B and C are separated by 2.4 cm, which is the effective length of the heat sink.

The ACF microchannel heat sink design was evaluated by applying a uniform heat flux supplied by a large-area thin-film Ti resistor fabricated directly on the surface of the Si heat sink. A 5000-Å layer of SiO₂ beneath the 1000-Å Ti layer provided electrical insulation between the resistor film and the Si. Electrical contacts were formed at each end of the Ti film so as to produce a heated area 2.3 cm in length (streamwise) and 1 cm in width. A thermal image-processing system was intentionally used to determine the temperature rise and uniformity over the heat sink. Relatively small flow rates were used to enhance the temperature variations, which were otherwise difficult to measure accurately. Data were obtained for an applied heat load of 18.6 W/cm² and an initial coolant temperature of 22°C with the heat sink operating at two different coolant flow rates. In case 1, the flow rate was 15.8 cm³/s with a pressure drop across the heat sink of 73 kPa. The flow rate and pressure drop for case 2 were 28 cm³/s and 248 kPa, respectively.

The experimental results are compared with theoretical predictions in Figure 1-2. The theoretical results were obtained from finite-difference calculations with appropriate boundary conditions. The calculated maximum surface temperature rise above the inlet water temperature occurs in the center of the heat sink and for case 1 was 2.6°C, which corresponds to a maximum thermal resistance R_{th} of 0.14°C cm²/W. (Here, thermal resistance is defined as the ratio of the rise in surface temperature above inlet coolant temperature to the heat flux.) Longitudinal diffusion of heat was not included in the calculations, which show very little (< 0.04°C) falloff in temperature at the ends of the heat sink. The measured temperature rise in the center of the device is in agreement with the calculations, but the rapid temperature dropoff at the ends suggests strong longitudinal heat flow at the perimeter of the heat sink into the adjacent brass package. The use of additional heaters at the perimeter to reduce these end effects has been proposed [3]; alternatively, thermal insulation could be used. Except for these end effects, the experimental streamwise surface temperature profile is nearly constant ($\pm 0.1^\circ\text{C}$). Nevertheless, a consistent trend is detectable in the data suggesting a small slope (~ 13 percent/cm in case 1) in the profile at the center of the heat sink. This may be caused by either a gradient in the heat load (i.e., resistor thickness) or a variance in the flow rates in the two directions. For case 2, the measured maximum surface temperature rise was $\sim 2.0^\circ\text{C}$ with a profile similar to that of case 1. The center of the profile is essentially constant with only a small slope (< 6 percent/cm), which suggests that the stronger gradient observed for the lower total flow rate (case 1) is a result of a variance in the flow rates for the two directions. This slope can easily be eliminated by adjustment of the flow rates.

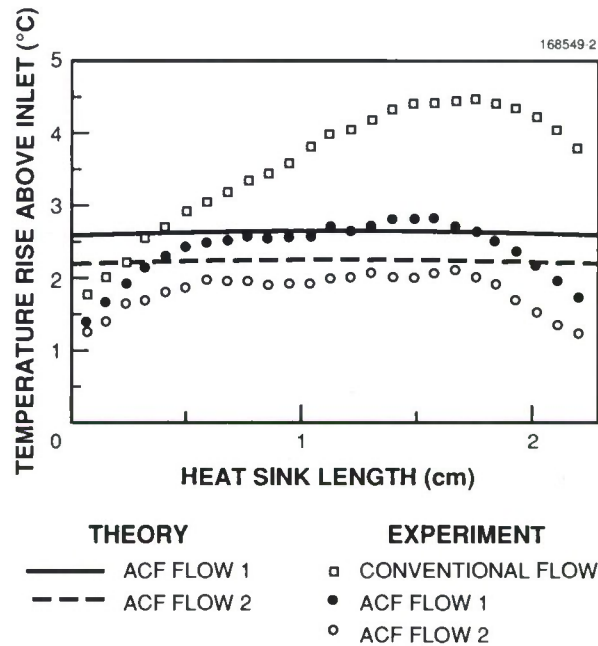


Figure 1-2. Experimental and theoretical temperature profiles for ACF heat sinks at two flow conditions together with the results for conventional flow in one direction through half of the channels.

To demonstrate the effects of the ACF design, the surface temperature for unidirectional flow was also measured. The manifold plate design did not allow for the same direction of flow in all of the channels simultaneously, so the flow in one of the directions was shut down. With unidirectional water flow in half of the channels ($7.9 \text{ cm}^3/\text{s}$ and a pressure drop of 73 kPa, similar to case 1) and stagnant water in the alternate channels, a large streamwise surface temperature gradient of $1.5^\circ\text{C}/\text{cm}$ (or 42 percent/cm) was observed in the center of the heat sink.

The ACF design is particularly attractive for longer channels, and it is interesting to consider a large-area heat sink with high-flow conditions. A $10 \times 10\text{-cm}$ heat sink with 10-cm-long channels was theoretically modeled for a heat flux of $100 \text{ W}/\text{cm}^2$ and a flow rate of $44.4 \text{ cm}^3/\text{s}$, corresponding to a Reynolds number of 2500 (just within the turbulent regime for rectangular channels). The calculated rise in heat sink surface temperature and average increase in water temperature above the inlet water temperature are shown in Figure 1-3(a) as a function of position parallel to the flow. The maximum surface temperature rise and the maximum thermal resistance of the heat sink are 13.3°C and $0.13^\circ\text{C cm}^2/\text{W}$, respectively. The surface temperature differential between the inlet/outlet and the center is only 0.85°C , or 6 percent; again, longitudinal heat diffusion was assumed to be zero. In a 10-cm-long unidirectional-flow heat sink operating at the same total flow rate the maximum surface temperature rise would be $\sim 15.5^\circ\text{C}$ (the maximum R_{th} is $0.155^\circ\text{C cm}^2/\text{W}$), and the streamwise variation in surface temperature would be 6°C , or 39 percent (the R_{th} variation is $0.06^\circ\text{C cm}^2/\text{W}$, and the maximum contribution to R_{th} due to the water temperature rise would be $0.06^\circ\text{C cm}^2/\text{W}$).

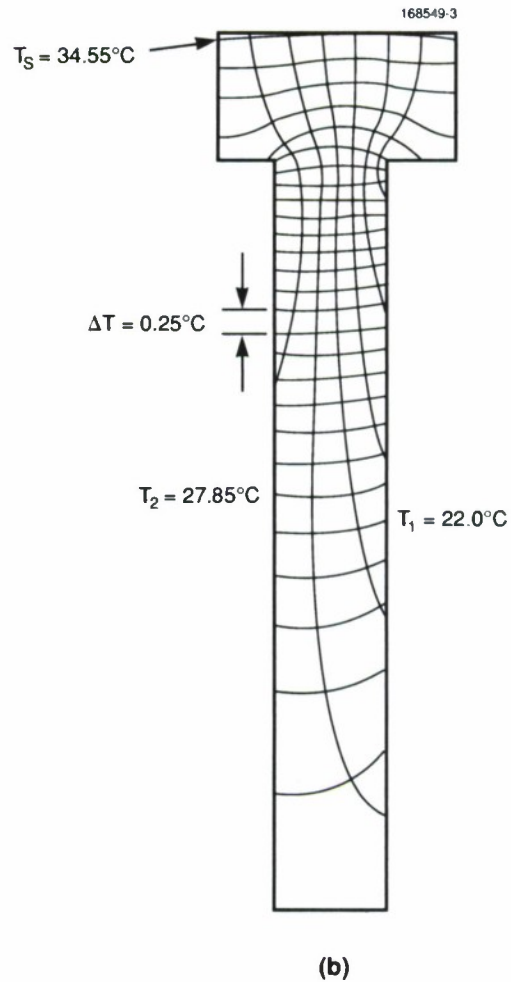
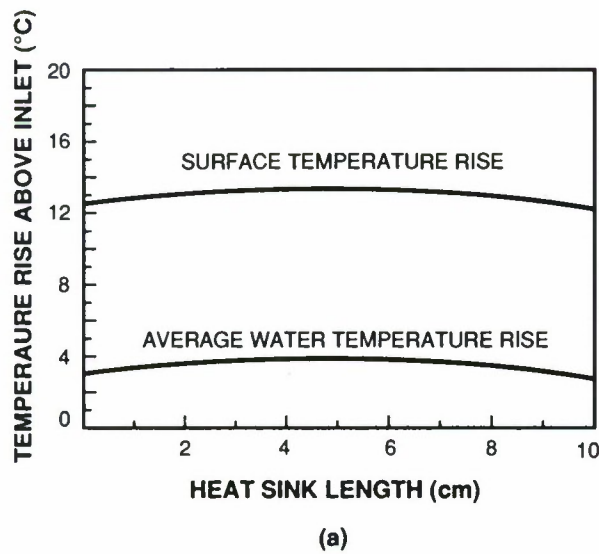


Figure 1-3. Calculated temperature distributions for a 10×10 -cm heat sink with 100-W/cm^2 heat flux. (a) Streamwise profiles of heat sink surface temperature rise and average water temperature rise above the inlet water temperature. (b) Flux plot for a fin at the inlet/outlet position showing isotherms and adiabats. The inlet and outlet water temperatures T_1 and T_2 and the heat sink surface temperature T_S directly above the fin are indicated. Isotherms are shown in increments of 0.25°C .

The finite-difference calculation was also used to generate a heat-flux plot for a cross section of a cooling fin at the inlet/outlet position (where the maximum difference in adjacent channel temperatures occurs), as shown in Figure 1-3(b). Isotherms are drawn for temperature increments of 0.25°C together with adiabatic lines. The lateral temperature variation at the heated top surface of the fin is seen to be < 0.05°C. Most of the heat entering the top of the fin exits to the inlet side, as expected.

The pressure drop created at the 44.4-cm³/s flow rate by friction losses in the 10-cm-long channels was calculated to be 452 kPa. The corresponding mechanical power dissipated by this flow of water through the microchannels would be 2.0 W/cm², which is only 2 percent of the assumed heat load. Hence, the above ACF heat sink cooling projections are conservative, and still lower thermal resistance and better uniformity should be obtainable at higher flow rates.

L.J. Missaggia
J.N. Walpole

1.2 STUDIES OF MULTIPLE QUANTUM WELLS PRODUCED BY GROWTH INTERRUPTION

Anomalously low photoluminescence (PL) energies have been observed from GaAs quantum wells with lattice-matched barriers of Ga_{0.51}In_{0.49}P (GaInP). This material was grown by organometallic vapor phase epitaxy (OMVPE) at 650°C with an atmospheric pressure reactor in the chimney configuration [7]. Differences in PL behavior between thick and thin layer structures give reason to focus on the heterojunction interface as the source of the problem. We have directed our attention to the chemistry at the interface, although impurity level behavior there [8] has not been ruled out. By x-ray and PL studies of structures produced solely by periodic interruptions during growth, we show that the interface problem is not due to In segregation but is caused by substitution of As for P during the brief pause that we usually introduce between the GaInP and GaAs growths. This effect complicates the formation of heterojunction structures in which the composition of the group V sublattice is switched.

Figure 1-4 shows a simulated rocking curve [9] for a ten-unit structure, with each unit consisting of a 500-Å layer of GaInP and a 3-Å layer of InP. The curve simulates the (004) reflection with Cu K α radiation (0 arc see corresponding to a Bragg angle of 33° for GaAs) measured with a double-crystal diffractometer operated in the antiparallel (+,-) configuration. In addition to the large peak at 0 arc see attributable to the substrate, there are a series of peaks, with intensities that should be readily observable, associated with the multiple quantum well (MQW). The motivation for simulating this structure is the following: it has been conjectured that, because of the atomic sizes and/or bond strengths, In tends to segregate to the surface during alloy growth, giving rise to a monolayer or so of In [10]. If this is the case and the growth is terminated by turning off the flows of the Ga and In metallorganics while keeping the flow of PH₃, the final molecular layer should be InP. The simulation, which assumes the InP to be coherent with the InGaP in the growth plane, shows that there is adequate sensitivity with x-ray diffraction to establish the existence of this monomolecular layer.

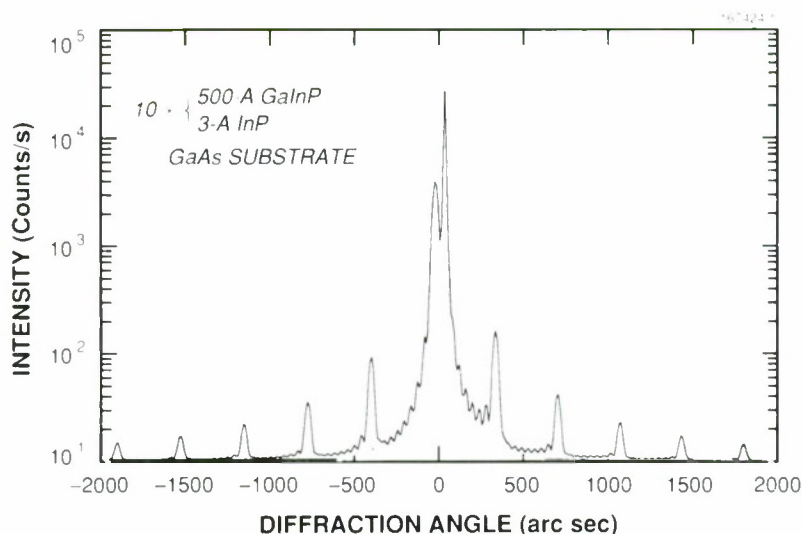


Figure 1-4. Simulated (004) rocking curve for a ten-period structure, with each unit consisting of a 500-Å GaInP layer and a 3-Å InP layer. For visualization reasons, the composition of the GaInP is chosen to give a slight mismatch from the GaAs substrate.

A test structure was made by first growing a 5000-Å GaInP buffer layer and then performing ten sequences of 2-s exposure to PH_3 followed by growth of 500 Å of GaInP. The rocking curve is shown in Figure 1-5. In addition to the substrate peak, there is a peak attributable to the GaInP buffer layer and another to the GaInP of the ten-period structure. Ideally, the two GaInP peaks should be at the same position and somewhat narrower. Difficulties with the In source stability are thought to have caused this nonideal behavior. The important point, however, is that the MQW peaks of Figure 1-4 are absent here, and thus there is no evidence of In accumulation at the growth surface. As further evidence of the absence of an In-rich interface layer, the room-temperature PL, illustrated in Figure 1-6, indicates a peak energy of 1.82 eV. This is the same as that observed for bulk GaInP grown under the same conditions.

To test the stability of the phosphorus-terminated surface, another ten-period test structure was grown with an interruption divided into 2 s of PH_3 flow, 2 s of AsH_3 flow, and 2 s of PH_3 flow. The rocking curve, seen in Figure 1-7, now shows evidence of MQW formation, and the peak PL emission from this structure, seen in Figure 1-6, has dropped to 1.40 eV. Apparently, in the 2 s of AsH_3 exposure, As has replaced some of the P on the surface of the GaInP alloy, and this has not been reversed with the subsequent, but brief, PH_3 flow. The formation of a $\text{GaInAs}_x\text{P}_{1-x}$ alloy, having a narrower bandgap than GaInP, would reduce the PL emission energy, with the exact energy depending on the thickness of the substitution layer and the As-P ratio. No emission is observed from the GaInP because the photoexcited carriers quickly relax to the lower energy wells.

Other combinations have been tried. Interruptions of GaAs growth with PH_3 flowing during the pause fail to produce MQWs. However, an InP surface is readily altered by 2 s of exposure to AsH_3 , as shown by the evidence of MQW peaks in the rocking curve of Figure 1-8.

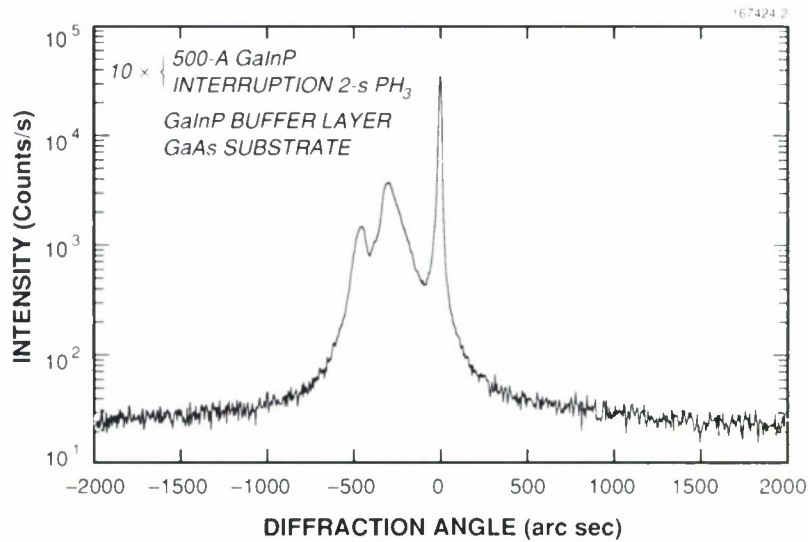


Figure 1-5. Rocking curve of a sample grown with ten periodic interruptions to GaInP growth. The PH_3 flow was maintained during the 2-s interruption. Two separate peaks due to the GaInP in a buffer layer and in the interrupted-growth layer complicate the curve, but there is no evidence of the periodic structure attributable to an MQW.

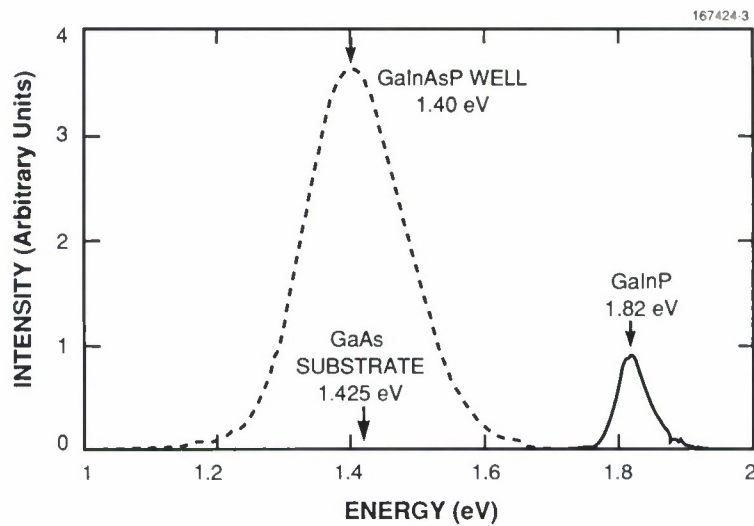


Figure 1-6. Photoluminescence at room temperature from growth-interrupted structures. The solid curve is for the structure of Figure 1-5 and shows only a peak attributable to GaInP and a very weak peak due to the GaAs substrate. The dashed curve is for the sample of Figure 1-7 and shows a strong peak at 1.40 eV.

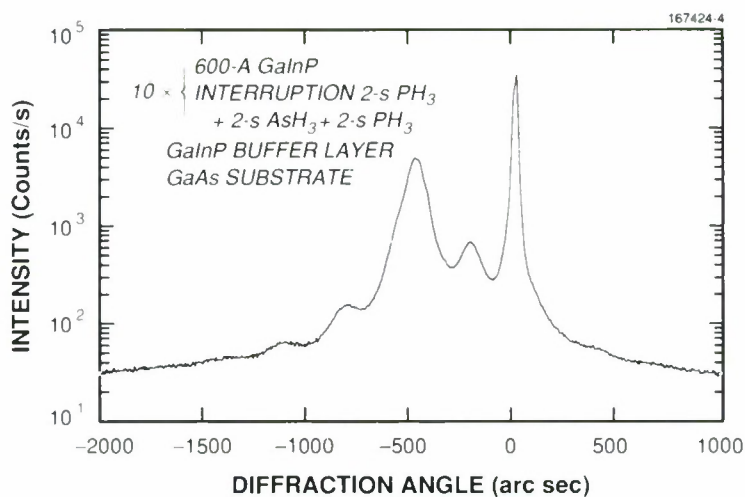


Figure 1-7. Rocking curve of a sample grown with ten periodic interruptions to GaInP growth. During the 6-s interruptions the flow sequence was 2-s PH_3 , 2-s AsH_3 , 2-s PH_3 . The rocking curve shows evidence of an MQW with a period of ~ 600 Å.

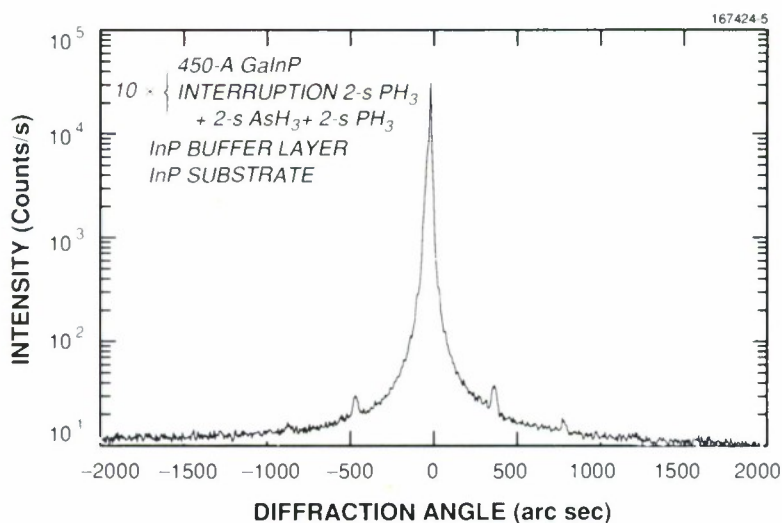


Figure 1-8. Rocking curve of a sample grown with ten periodic interruptions to InP growth. During the 6-s interruptions the flow sequence was 2-s PH_3 , 2-s AsH_3 , 2-s PH_3 . The rocking curve shows evidence of an MQW with a period of ~ 450 Å. Here, 0 arc sec corresponds to the (004) Bragg angle of InP, 31.7° . The x-ray intensity pattern is simpler than that in Figure 1-7 because, other than the interfacial layers, the entire structure including the substrate is InP.

In regard to the anomalous PL of GaAs wells with GaInP barriers mentioned earlier, apparently an interfacial layer of $\text{Ga}_{0.51}\text{In}_{0.49}\text{As}_x\text{P}_{1-x}$ is formed in the pause between GaInP and GaAs growth. For $x > 0.4$, the energy gap of the interfacial alloy will be less than that of GaAs, and the interfacial region will tend to bind carriers and reduce the PL energy. For the case of $\text{In}_{0.53}\text{Ga}_{0.47}\text{As}$ wells with InP barriers, there is no observed lowering of the expected PL emission. This is understandable if the interfacial alloy, $\text{InAs}_x\text{P}_{1-x}$, has $x \leq 0.6$ and thus an energy gap larger than that of $\text{In}_{0.53}\text{Ga}_{0.47}\text{As}$.

In conclusion, this work shows that As will rapidly substitute for P on GaInP and InP surfaces. The fact that the GaAs surface is stable under PH_3 flow, at least for a few seconds, suggests a possible means of dealing with the GaInP/GaAs quantum-well problem. The vapor pressure of P species over GaP at 650°C is about the same as that for As over GaAs and much less than the vapor pressure of P over GaInP or InP. Terminating the growth of the GaInP with GaP should reduce the P loss and the As substitution and should also increase the energy gap of any interfacial layer grown.

These preliminary experiments give a qualitative picture of some of the chemistry that can occur at heterojunctions. They need to be followed by experiments and analysis to give a better idea of the depth and composition of the interfacial layers. Also, these experiments suggest that terminating the GaInP growth with GaP may indeed raise the PL energy. However, more work is needed to fully test this method of growing GaInP/GaAs structures.

S.H. Groves	S.C. Palmateer
D.R. Calawa	P.A. Maki

1.3 MEASUREMENTS OF TRIMETHYLINDIUM SOURCE EFFICIENCY AND STABILITY

The growth of $\text{In}_x\text{Ga}_{1-x}\text{As}_y\text{P}_{1-y}$ alloys which are lattice matched to InP or GaAs by OMVPE requires precise compositional control, which in turn requires precise control of the concentration of the organometallics in the gas entering the OMVPE reactor. Source alkyls are generally held in a temperature-controlled stainless steel cylinder through which carrier gas flows are metered by a mass flow controller (Figure 1-9). The carrier gas becomes saturated by the vapor pressure of the source. The concentration of organometallics in the outflowing carrier gas is generally assumed to be uniquely determined by the alkyl temperature and flow rate.

This assumption may be questioned for trimethylindium (TMI), because it is a solid source at normal operating temperatures ($\text{mp} = 88^\circ\text{C}$) and the published measurements of vapor pressure of TMI exhibit considerable scatter. It has been proposed that these vapor pressure variations are due to the presence of more than one form of TMI or a change in crystalline state (or surface area) with cylinder usage. Approaches to overcome recrystallization of TMI that have been implemented are reversal of gas flow through the cylinder and modification of the internal cylinder design to increase the TMI surface area. The recent technical development and commercial availability of an in situ ultrasonic monitoring device [11] now permit measurements of TMI vapor concentration under typical OMVPE growth conditions [12],[13]. We have used this ultrasonic monitor to measure the vapor concentration of TMI from source cylinders of several suppliers. Large source-to-source variations were found, and sudden concentration instabilities were frequently observed. These variations and instabilities make the controlled growth of lattice-matched $\text{In}_x\text{Ga}_{1-x}\text{As}_y\text{P}_{1-y}$ alloys difficult.

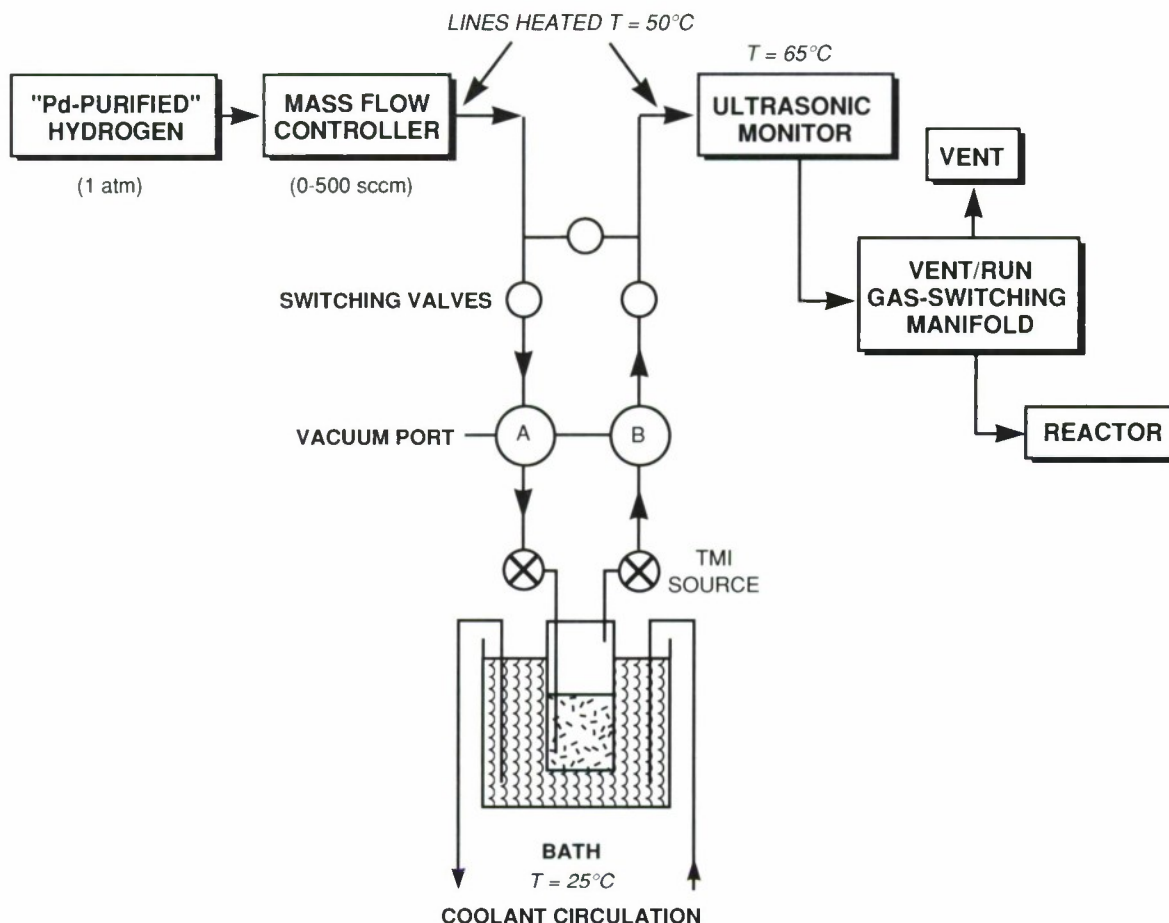


Figure 1-9. Schematic of TMI source plumbing with specially modified three- and four-way valves for leakage testing and purging. The three- and four-way valves are indicated by A and B, respectively.

Measurements were performed on six TMI source cylinders of nominally 200-cm³ volume with 50 or 100 g of TMI, using hydrogen flow rates of 50 to 500 sccm. Bypass valves installed before the source cylinder enabled easy changing and leak testing of a source cylinder. The TMI source is operated at a pressure of 820 Torr and a bath temperature of $25 \pm 0.1^\circ\text{C}$. This bath temperature results in growth rates of 1 to 5 $\mu\text{m/h}$ depending on flow rate and alloy composition. The gas lines downstream from the source are heated to 50°C , and the ultrasonic monitor is maintained at 65°C to avoid condensation of TMI. Volumetric percentage of TMI in H_2 was measured by the ultrasonic monitor [12].

The source history (i.e., cylinder configuration, cylinder preparation, material synthesis, filling technique, and age), operating temperature, and carrier gas flow are all factors that may affect the steady-state TMI concentration. Table 1-1 summarizes the characteristics of the six cylinders measured. We

TABLE 11-1
Summary of TMI Source Cylinder Characteristics

Cylinder Number	Supplier (Filling Technique)	TMI Content (g)	Initial Efficiency at 200 sccm	Flow Dependence Efficiency Decrease from 50 to 500 sccm (%)	Stability and Usage
1	A (Sublimed)	50	0.98	5	10% Efficiency decrease during initial 10 g, then stable until cylinder exhausted Age 24 mo, in use 18 mo
2	A (Sublimed)	100	0.98	4	Stable for initial 50 g, then 10% efficiency decrease and unstable Age 24 mo, in use 24 mo
3	A (Sublimed)	100	0.92	5	Stable for initial 10 g, then 10% efficiency decrease and unstable Age 18 mo, in use 18 mo
4	A (Sublimed)	100	0.98	0	Stable for initial 2 g, then 10% efficiency decrease and unstable Age ~ 11 mo, in use 2 mo
5	B (Crushed)	50	0.79	4	Stable, 1 g used Age 6 mo, in use 0.3 mo
6	C (Sublimed)	100	0.44	47	Stable, 5 g used Age 4 mo, in use 3 mo

define the source efficiency as the ratio of the observed concentration to that predicted from published vapor pressure data, and for the six cylinders measured the initial efficiency at 200 sccm ranged from 0.44 to 0.98. The 19 percent variation in source efficiency for cylinders 1 through 5 required a calibration layer to be grown when a source was changed, but lattice matching was easily achieved by adjusting the mass flow controller setting based on the measured TMI concentration. The low efficiency obtained from cylinder 6 limited the ability to achieve reasonable growth rates at a source temperature of 25°C.

The source efficiency versus flow rate for the three types of behavior observed is shown in Figure 1-10. Source performance ranges from a steady-state TMI concentration independent of flow rate (cylinder 4), to a 4 percent decrease in steady-state TMI concentration with an increase in flow rate from 50 to 500 sccm (cylinder 2), to a 47 percent decrease in concentration with the same flow rate increase (cylinder 6). Cylinders 1, 3, and 5 exhibited behavior similar to that of cylinder 2, as summarized in Table 1-1. Without the ability to characterize source efficiency as a function of flow, it would be impossible to control lattice matching of quaternary alloys. Even with the ability to measure TMI vapor concentration, large changes in source efficiency as a function of flow complicate alloy growth. In more advanced structures, where one wants to grade the quaternary composition in the confinement region of a laser structure, efficiency as a function of flow must be fairly constant.

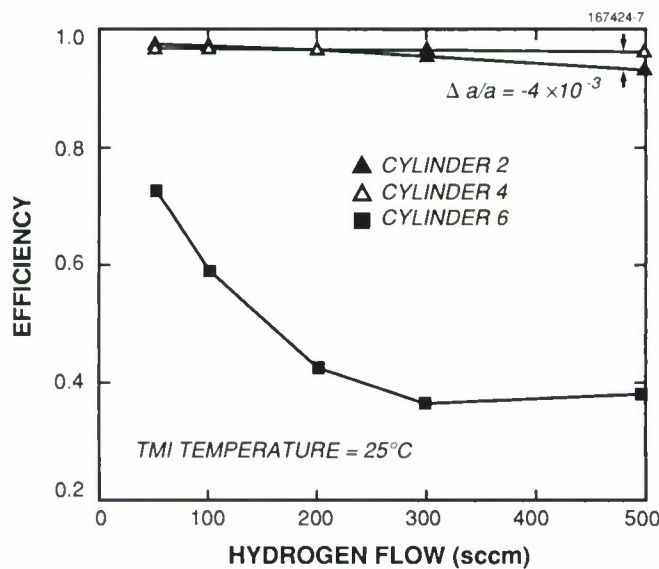


Figure 1-10. Source efficiency versus flow rate for three different TMI source cylinders at 25°C in a typical OMVPE growth run. The small decrease in source output for cylinder 2 gives rise to a change in the unstrained $Ga_{0.51}In_{0.49}P$ lattice parameter of $\Delta a/a = -4 \times 10^{-3}$.

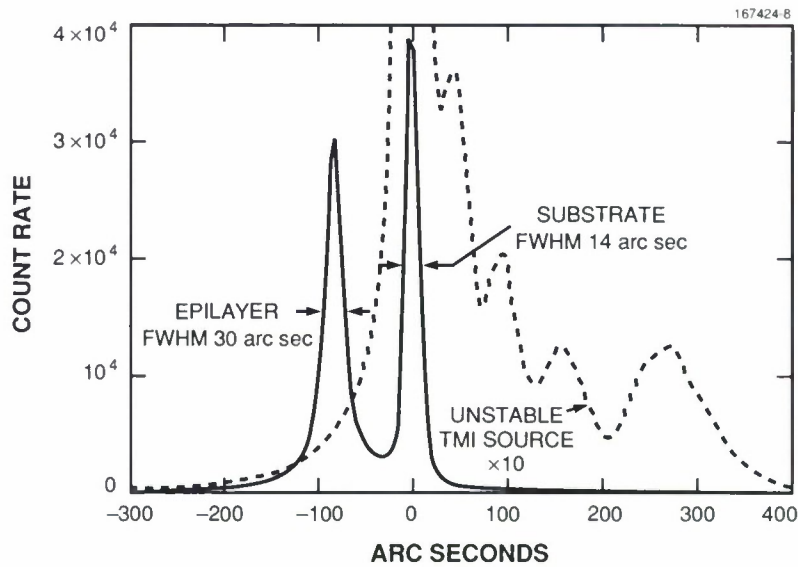


Figure 1-11. Double-crystal x-ray diffraction for 1.2- μm -thick $\text{Ga}_{0.51}\text{In}_{0.49}\text{P}$ epilayers on GaAs substrates grown with stable (solid curve) and unstable (dashed curve) TMI sources. The fluctuations for the unstable source represent a change in the unstrained lattice parameter of $\Delta a/a = 3 \times 10^{-4}$ to 2×10^{-3} .

We believe that the source stability is related to length of time, as the TMI was sublimed and in its crystalline form in the cylinder. The advent of instability does not appear to be related to the amount of TMI consumed. Three sources that were stable for 1 to 2 years suddenly exhibited a 10 percent decrease in steady-state TMI concentration and then became unstable, resulting in compositional fluctuations in the epilayers. Figure 1-11 shows double-crystal x-ray diffraction data for 1.2- μm -thick $\text{Ga}_{0.51}\text{In}_{0.49}\text{P}$ layers grown on GaAs substrates with stable and unstable TMI sources. The diffraction pattern for the stable source shows two peaks with very narrow full width at half-maxima for both the epilayer and substrate. The pattern for the unstable source shows four epilayer peaks indicating that the TMI source operated at four discrete efficiencies. These fluctuations correspond to $\Delta a/a = 3 \times 10^{-4}$ to 2×10^{-3} . We have also observed unstable sources to operate at one discrete, but unpredictable, efficiency during a growth run, which was consistent with the ultrasonic monitor readings.

The stability data for the six sources in these experiments is summarized in Table 1-1. When cylinder 4 became unstable after use of only 2 g, we consumed an additional 5 g, but the instability remained. We then removed the cylinder from the bath, agitated it by continuous rapping with a hammer, and returned it to the system. The source became more stable, but the efficiency was still much lower than the original stable value and continued to exhibit drift. Next, we reversed the flow through the cylinder and found the efficiency unchanged and unstable. Since length of time from sublimation into the cylinder appears to be a possible cause of source instability, it may be important to minimize this time to maximize the useful life of a source. For example, it may be advantageous to purchase sources with only 25 to 50 g of TMI.

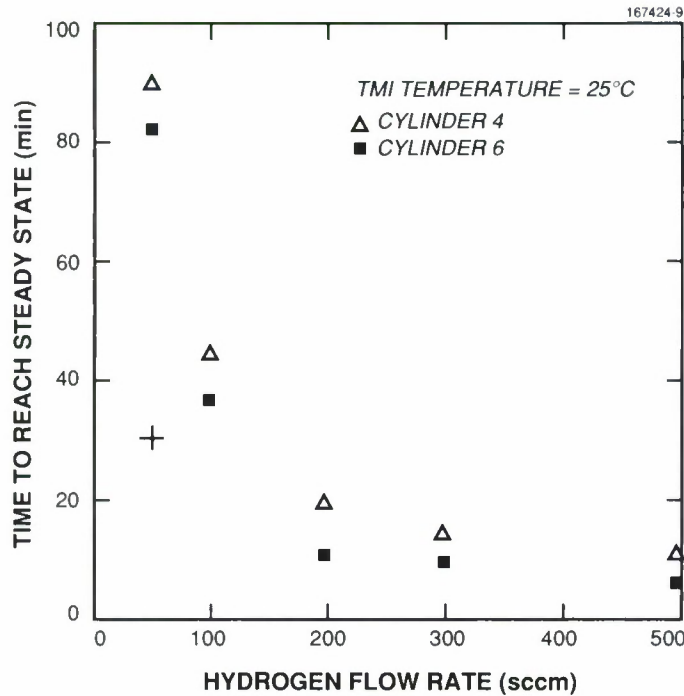


Figure 1-12. Time to reach steady-state TMI concentration versus flow rate for a TMI source temperature of 25°C. Cylinder 6 with a volume of 175 cm³ stabilizes more rapidly than cylinder 4 with a volume of 200 cm³. Approximately 20 cylinder volume changes (~ 4000 cm³) are required to reach steady state. The data point (+) represents the total time to reach steady state when the carrier gas is flowed through cylinder 4 at 500 sccm for 10 min and the rate is then dropped to 50 sccm.

The time to reach a steady-state TMI concentration decreases with increasing flow rate as shown in Figure 1-12 for cylinders 4 and 6. At 50 sccm a steady state is reached in ~ 90 min and at 500 sccm it is attained in ~ 15 min. The stabilization time at low flow rates can be reduced by an initial high flow. After an initial 10-min flow at 500 sccm, the flow at 50 sccm reached steady state within 20 min. Stabilization times were similar for all six cylinders measured and required a total volume flow of ~ 4000 cm³. Reproducible lattice matching of quaternary alloys ($\Delta a/a \leq 3 \times 10^{-4}$) has been achieved by flowing carrier gas through the source for these predetermined stabilization times prior to growth.

An ultrasonic monitor is a powerful in situ diagnostic tool that allows characterization of solid source TMI behavior under typical OMVPE growth conditions without growing and characterizing numerous epitaxial layers. Use of an ultrasonic monitor has enabled us to reproducibly control the composition of quaternary alloys to $\Delta a/a < 3 \times 10^{-4}$ by adjusting the mass flow controller based on TMI concentration measurements. Even so, the large variation in TMI source efficiency and stability makes reproducible growth of quaternary layers difficult. Understanding the reasons for this behavior and improving the consistency of TMI source efficiency and stability are essential for controlled growth of lattice-matched III-V alloys containing In.

S.C. Palmateer A. Napolcone
S.H. Groves

REFERENCES

1. D.B. Tuckermann and R.F. Pease, *IEEE Electron Device Lett.* **EDL-2**, 126 (1981).
2. T. Kishimoto and S. Sasaki, *Electron. Lett.* **23**, 456 (1987).
3. R.J. Phillips, *Lincoln Lab. J.* **1**, 31 (1988).
4. D. Munding, R. Beach, W. Benett, R. Solarz, W. Krupke, R. Staver, and D. Tuckermann, *Appl. Phys. Lett.* **53**, 1030 (1988).
5. L.J. Missaggia, J.N. Walpole, Z.L. Liau, and R.J. Phillips, *IEEE J. Quantum Electron.* **25**, 1988 (1989).
6. J.P. Donnelly, K. Rauschenbach, C.A. Wang, R.J. Bailey, J.N. Walpole, L.J. Missaggia, J.D. Woodhouse, H.K. Choi, F.J. O'Donnell, and V. Diadiuk, *Proc. SPIE* **1219**, 255 (1990).
7. S.C. Palmateer, S.H. Groves, J.W. Caunt, and D.L. Hovey, *J. Electron. Mater.* **18**, 645 (1989).
8. J.D. Dow, S.Y. Ren, J. Shen, R.D. Hong, and R.P. Wang, *J. Electron. Mater.* **19**, 829 (1990).
9. Solid State Research Report, Lincoln Laboratory, MIT, 1990:3, p. 9.
10. J.M. Moison, C. Guille, F. Houzay, F. Barthe, and M. Van Rompay, *Phys. Rev. B* **40**, 6149 (1989).
11. Thomas Swan and Co., Ltd., Cambridge, UK.
12. J.P. Stagg, *Chemtronics* **3**, 44 (1989).
13. B.R. Butler and J.P. Stagg, *J. Cryst. Growth* **94**, 481 (1989).

2. QUANTUM ELECTRONICS

2.1 FUNDAMENTAL LINEWIDTH OF MICROCHIP LASERS

One contribution to the finite spectral width of all lasers, as originally described by Schawlow and Townes [1], is the coupling of spontaneous emission to the oscillating mode [1],[2], which results in a Lorentzian power spectrum. For many lasers, this contribution alone determines the fundamental linewidth, and it is common practice to determine the fundamental linewidth of a laser by fitting the tails of the measured power spectrum to a Lorentzian curve. In the microchip laser, however, another important contribution to the fundamental linewidth is thermal fluctuations of the cavity length at a constant temperature [3]. This contribution is expected to result in a Gaussian power spectrum and, because of the short cavity lengths of microchip lasers, is much larger than the contribution due to spontaneous emission. However, because a Gaussian curve decays more quickly than a Lorentzian curve, the tails of the power spectrum will still correspond to the Lorentzian contribution. Therefore, it is important to understand both the effects of spontaneous emission and thermal fluctuations.

The Lorentzian contribution to the fundamental linewidth of a microchip laser has a full width at half-maximum (FWHM) of

$$\Delta\nu_L = (h\nu_0/16\pi P_o)(c/n\ell)^2(\ln R - 2\alpha_L\ell)\ln R, \quad (2.1)$$

where h is Planck's constant, ν_0 is the center frequency of the laser, P_o is the output power, c is the speed of light in vacuum, n is the refractive index, ℓ is the cavity length, R is the reflectivity of the output coupler, and α_L is the round-trip cavity loss not including transmission through the output coupler. For microchip lasers, $\Delta\nu_L$ from Equation (2.1) is typically a few hertz, which is consistent with experimental measurements [4],[5].

The spectral-broadening effects of thermal fluctuations in cavity length are easily calculated using the principle of equipartition of energy derived from classic mechanics. This principle states that if the energy of a system may be written as a sum of independent terms, each of which is quadratic in the variable representing the associated degree of freedom, then in equilibrium at temperature T , each term (or degree of freedom) contributes $k_B T/2$, where k_B is Boltzmann's constant, to the energy of the system. For the microchip laser, this leads to the expression

$$C_{11}\langle(\Delta\ell/\ell)^2\rangle V = k_B T, \quad (2.2)$$

where C_{11} is the longitudinal elastic constant ($C_{11} = 33 \times 10^{11}$ erg cm⁻³ for YAG), $\Delta\ell$ is the change in the cavity length ℓ , V is the volume of the lasing mode, and the angle brackets indicate averaging over time. Equation (2.2) results in a Gaussian contribution to the fundamental linewidth, with a FWHM of

$$\Delta\nu_G = \nu_0[8\ln(2)k_B T / C_{11}V]^{1/2}. \quad (2.3)$$

For microchip lasers the value of $\Delta\nu_G$ varies with pump power and pump-beam diameter [6]. Under the conditions of our heterodyne measurements [4],[5], $\Delta\nu_G$ from Equation (2.3) is typically between 5 and 7 kHz, which is comparable to our instrument resolution.

J.J. Zayhowski

2.2 Q-SWITCHED MICROCHIP LASERS

The typical cavity lengths of microchip lasers [4],[5] are short (< 1 mm), which results in short cavity lifetimes and the possibility of much shorter gain-switched and Q-switched pulses than can be achieved with conventional solid state lasers. Subnanosecond output pulses have been obtained from gain-switched microchip lasers using a gain-switched $\text{Ti:Al}_2\text{O}_3$ laser as a pump source [5],[7]. In these experiments, however, the peak power of the pump was several kilowatts, a power level not readily attainable with diode lasers. With the use of a 500-mW diode-laser pump, the shortest gain-switched output pulses we achieved had a FWHM of 170 ns [8].

With continuous diode-laser pumping, Q-switched operation of microchip lasers is possible. Computer modeling indicates that with a pump power of 500 mW, Q-switched Nd:YAG microchip laser pulses having a FWHM of less than 250 ps and a peak power of several kilowatts are feasible. This model assumes that the Q of the laser cavity can be switched in a time that is less than the pulse buildup time and that the optical efficiency of the Q-switched microchip laser is comparable to that of a CW microchip laser.

We are using a novel Q-switching method that exploits the large mode spacing of the microchip laser cavity. The output coupler of a CW microchip laser is replaced by a tunable etalon. At the lasing wavelength, which is determined by the fixed optical distance between the pump mirror and the first of two partially reflecting mirrors forming the tunable etalon, the reflectivity of the etalon is a strong function of the etalon's optical length. By changing this length, we can switch the Q of the laser cavity. If the free spectral range of the etalon is approximately the same as the mode spacing of the microchip laser, all potential lasing modes of the laser see the same reflectivity, and lowering the Q of one mode will lower the Q of all modes so that no mode can reach threshold. Figure 2-1 illustrates this concept. A large population-inversion density results in a short output pulse when the laser cavity is switched to the high-Q state.

To demonstrate this technique a Q-switched microchip laser, shown in Figure 2-2, was constructed from a CW 1.064- μm Nd:YAG microchip laser; a discrete, flat partially reflecting mirror; and an annular piezoelectric actuator. The CW microchip laser consists of a 650- μm -long piece of 1.3-wt.% Nd:YAG with two flat mirrors (a pump and a partially reflecting mirror) [4],[5]. The discrete partially reflecting mirror is mounted on the piezoelectric actuator and held parallel to the mirrors of the CW laser. The piezoelectric actuator has a nominal response of 0.5 $\mu\text{m}/\text{kV}$. The partially reflecting mirror of the CW device, the discrete partially reflecting mirror, and the piezoelectric actuator form the tunable etalon. To Q-switch the device, the voltage applied to the piezoelectric actuator is changed.

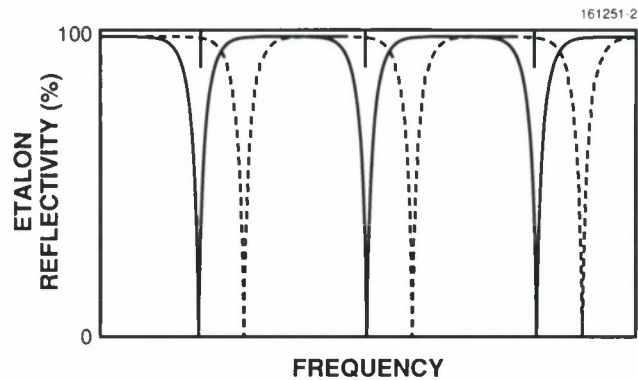


Figure 2-1. Reflectivity of an etalon as a function of frequency. The potential lasing wavelengths of a microchip laser (determined by the cavity modes) are indicated by the tic marks at the top of the figure. For the present device, they are spaced by ~ 127 GHz. The length of the etalon has been chosen so that its free spectral range is the same as the mode spacing of the microchip laser. The etalon can be tuned to be highly transmitting (solid curve) or highly reflecting (dashed curve) at the potential lasing frequencies of the microchip laser.

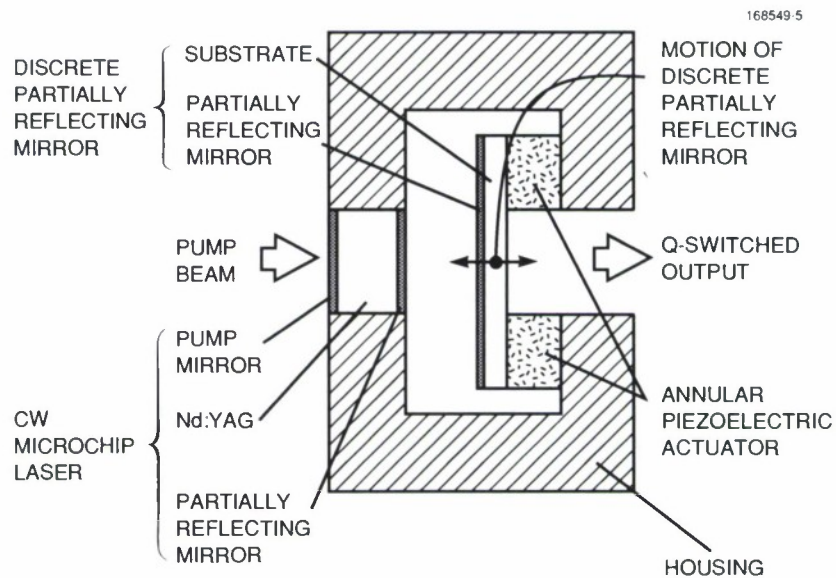


Figure 2-2. Cross section of a piezoelectrically Q-switched microchip laser. In these experiments the Nd:YAG crystal is $0.65 \times 1.0 \times 1.0$ mm, and the total distance between the pump mirror and the discrete partially reflecting mirror is ~ 1.8 mm. The piezoelectric actuator is 2.5 mm thick and has an outer diameter of 20 mm.

The Q-switched microchip laser is pumped with 120 mW of incident 808-nm light from a Ti:Al₂O₃ laser; this pump power can be easily obtained from a diode laser. Q-switching is performed by driving the piezoelectric actuator with the superposition of a dc component and a 100-V (peak-to-peak) triangular wave at a repetition rate of 40 kHz. The dc component and the repetition rate of the triangular wave were selected to give the minimum pulse width, while the magnitude and shape of the ac component of the drive signal were dictated by the repetition frequency and the slew rate of our voltage supply. The microchip laser maintains operation at a single frequency and polarization in the fundamental transverse mode during Q-switching. During each drive period two output pulses are produced. As shown in Figure 2-3, the FWHM of these pulses is ~ 6 ns, and no after-pulsing is observed. These are already among the shortest Q-switched pulses obtained from a Nd:YAG laser, but there is much room for improvement. The pulse-to-pulse amplitude fluctuations are < 5 percent. The averaged output power of the Q-switched device is 3.5 mW, which gives a peak output power of ~ 7 W. Most of the output (70 percent) is through the pump mirror.

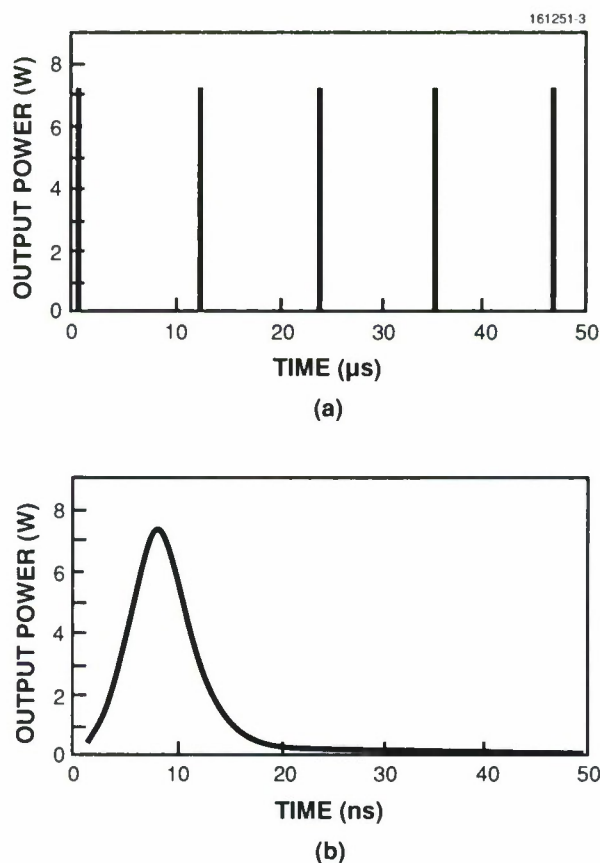


Figure 2-3. Output obtained from a 1.064- μm Q-switched Nd:YAG microchip laser showing (a) a train of pulses and (b) one pulse on an expanded time scale.

The pump mirror of the CW microchip laser used to construct the Q-switched device transmits the pump light and has a reflectivity of ~ 99.9 percent at $1.064\ \mu\text{m}$; the partially reflecting mirror of the CW device reflects the pump light and has a reflectivity of ~ 98.5 percent at the lasing wavelength. The discrete partially reflecting mirror has a reflectivity of ~ 99.7 percent at $1.064\ \mu\text{m}$. These high reflectivities result in most of the energy being lost within the Q-switched laser cavity rather than being coupled to the output beam. A better choice of reflectivities for the partially reflecting mirrors should lead to power efficiencies up to 33 percent, comparable to those obtained with CW microchip lasers [4],[5], provided that the time between Q-switched pulses is shorter than the spontaneous relaxation time of the gain medium. Lower-reflectivity partially reflecting mirrors will also result in a shorter cavity lifetime, leading to shorter output pulses. In addition, with lower reflectivities most of the output power can be obtained through these mirrors instead of the pump mirror.

J.J. Zayhowski
R.C. Hancock

2.3 POLARIZATION SWITCHING OF MICROCHIP LASERS

By introducing a birefringent element between the two partially reflecting mirrors of the tunable etalon in the Q-switched microchip laser discussed earlier [9], it is possible to transform the device into a polarization-switchable laser. The birefringent element breaks the polarization degeneracy of the cavity such that the two polarization states belonging to a single longitudinal and transverse mode see a low-Q cavity at different times as the etalon is swept across its free spectral range. With the application of the proper voltages to the piezoelectric actuator, the laser can be switched between the two polarizations.

Using this polarization-switchable device, we obtained complete polarization switching of the laser when the voltage applied to the (properly biased) piezoelectric actuator was changed by 200 V [10]. The switching time was $\sim 50\ \mu\text{s}$ and was limited by the response time of the actuator. To enhance the performance of the device, the piezoelectric actuator was eliminated and a $1 \times 1 \times 2\text{-mm}$ electrooptic birefringent element (LiTaO_3) was used. The LiTaO_3 was oriented with its x axis (the long dimension of the crystal) along the cavity axis and had electrodes deposited on the two z faces. Such an electrooptically controlled polarization-switchable microchip laser is illustrated in Figure 2-4. Complete polarization switching of the device still required an applied voltage change of $\sim 200\ \text{V}$, but the switching time was reduced to $< 5\ \mu\text{s}$, as shown in Figure 2-5. We suspect that this switching time, which was less than the time required for our voltage supply to switch between the high and low states, was limited by our electronics.

The cavity lifetime of the microchip laser is typically $< 1\ \text{ns}$, which suggests that much faster polarization switching should be obtainable. Since the laser is always oscillating in one of the two polarization states, except for the short time required to switch polarizations, the inversion of the laser is always clamped at its threshold value, and there is no significant relaxation spiking when the laser is switched between states.

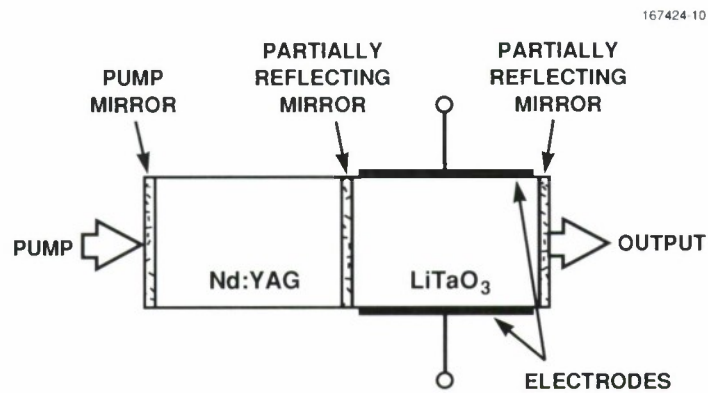


Figure 2-4. Illustration of an all-solid-state polarization-switchable microchip laser. Typical dimensions for such a device would be $1 \times 1 \times 2$ mm, with the longest dimension corresponding to the total cavity length.

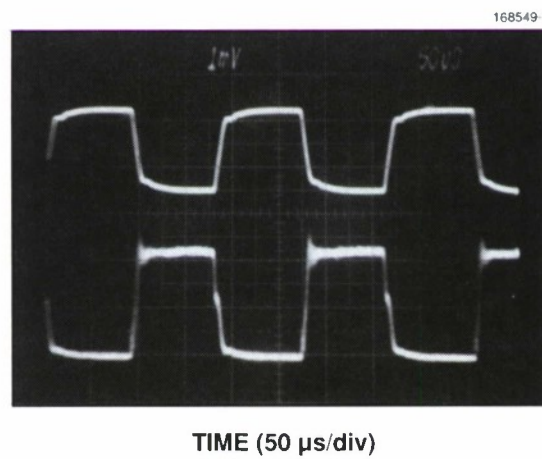


Figure 2-5. Traces showing (top) a square wave applied to the polarization-switchable microchip laser and (bottom) the intensity of its output in one polarization.

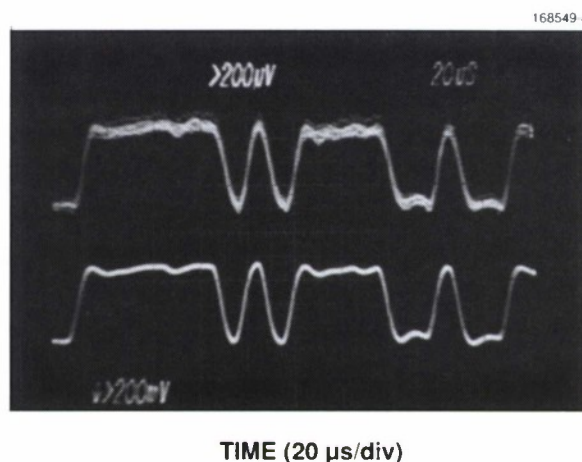


Figure 2-6. Traces showing (top) a pseudorandom binary waveform applied to the polarization-switchable microchip laser and (bottom) the intensity of its output in one polarization.

A binary data stream can be used to control the polarization of a polarization-switchable microchip laser. The digital information can be recovered by passing the output of the laser through a polarizer. To demonstrate this concept, a pseudorandom binary waveform with a 100-kHz bit rate was applied to the electrooptic element of the laser. (The bit rate was limited by our high-voltage electronics.) The output of the laser was passed through a polarizer and focused onto a detector. The detector output was then passed through a 100-kHz low-pass filter so that its frequency response was similar to that of the driving electronics. The resulting waveform was almost identical to the driving waveform, as shown in Figure 2-6. If sufficiently fast switching can be obtained, polarization-switchable microchip lasers may find applications in optical communications.

J.J. Zayhowski
R.C. Hancock

2.4 FREQUENCY-MODULATED Nd:YAG LASER

We describe the frequency-modulated performance of a compact Nd:YAG laser [11] having linear voltage-to-frequency conversion and frequency excursions of 1 GHz in < 1 ns. Other important features of this laser include single-frequency operation, sensitive electrooptic tuning, and a simply constructed stable cavity. The single-frequency operation is achieved by placing the thin (1 mm) Nd:YAG crystal at one end of the short laser cavity. A large frequency sweep at relatively low voltages is produced by a thin electrooptic modulator located in the laser cavity. Damping the acoustic resonances in the electrooptic material with external damping elements allows nearly constant tuning sensitivity for modulation frequencies below, near, and above the acoustic resonances.

The Nd:YAG laser is a two-mirror cavity contained in a 3-cm-long stainless steel cylinder as described in a previous report [11]. The 8-mm cavity contains a small (1×1 -mm cross section by 3-mm

length) LiTaO₃ modulator crystal. A voltage applied across the LiTaO₃ in the z direction tuned the laser at 12 MHz/V in agreement with the value calculated using the r_{33} coefficient [12]. To test the extent of the frequency sweep at low modulation rate, a high-voltage amplifier was used to generate a 1-kV triangular wave at 1 kHz. The frequency was found to sweep over 12 GHz, equal to the longitudinal-mode separation. Recently, 370-mW output power from an electrooptically tuned single-frequency Nd:YAG ring laser was obtained [13]. However, the tuning sensitivity was 0.32 MHz/V over a range of 3 GHz and was tested only at modulation frequencies below 1 kHz. The small size of our modulator crystal gives low capacitance, which is important for extending the electrooptic tuning to higher frequencies.

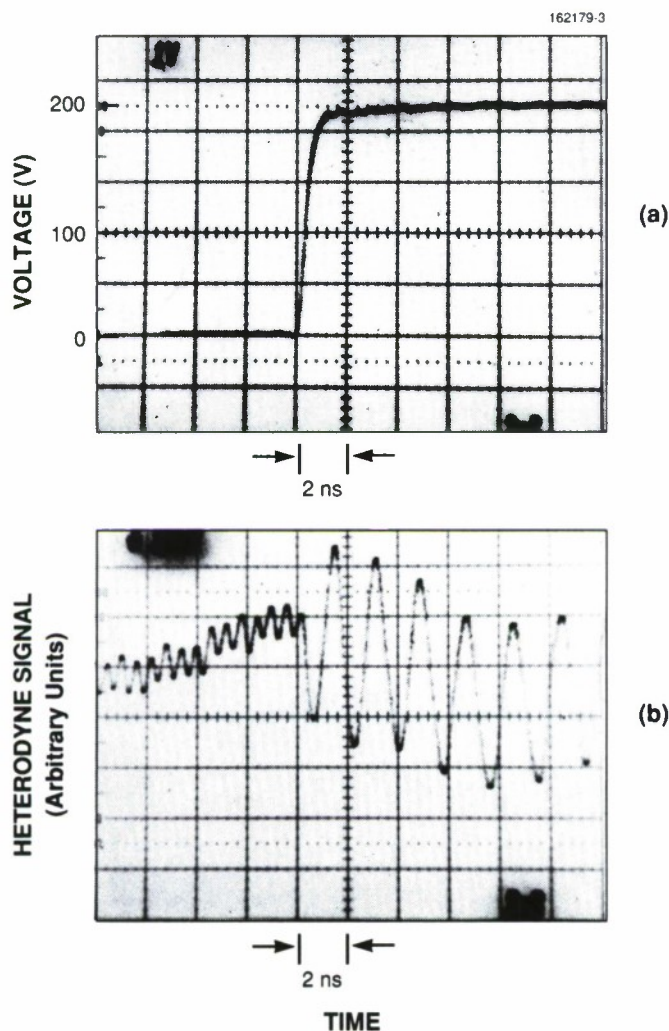


Figure 2-7. (a) High-voltage step applied to the LiTaO₃ crystal. The voltage change is 200 V and the electrical rise time is 0.5 ns. (b) Beat signal obtained in heterodyning the frequency-modulated Nd:YAG laser with a Nd:YAG local oscillator. Initially, the two lasers are offset by 1.7 GHz. The voltage step gives rise to a frequency difference of 550 MHz. The undulation of the trace is caused by noise pickup from the pulser.

A 200-V voltage step with a 1-ns rise time [Figure 2-7(a)] was applied to the LiTaO_3 to test the modulation speed of a second Nd:YAG laser design with a tuning sensitivity of 6 MHz/V. The outputs of the frequency-modulated laser and a stable single-frequency laser were combined on a 0.7-GHz InGaAs photodiode. The resulting heterodyne beat signal was displayed on a 1-GHz oscilloscope [Figure 2-7(b)]. Prior to the voltage step the two frequencies were separated by 1.7 GHz. The transition to ~ 550 -MHz separation took place within 1 ns; this transition time was limited by the 0.5-ns rise time of the voltage step [see Figure 2-7(a)].

The laser frequency was being modulated on a long time scale, compared with the round-trip time, so a linear voltage-to-frequency conversion occurred [14]. The round-trip time in our cavity was 150 ps. Calculations showed that the voltage-to-frequency conversion should have a maximum fractional nonlinearity of $t_r/2T$, where t_r is the rise time of the voltage step and T is the round-trip time in the laser cavity. For the experimental results shown in Figure 2-7, the maximum fractional nonlinearity of 15 percent should occur 0.5 ns after the start of the voltage rise; we could not measure this nonlinearity.

A precision measurement was made of the linearity of the voltage-to-frequency conversion on a longer time scale using the experimental measurement shown in Figure 2-8. In this case, a 42-V, 570-ns linear voltage ramp was applied to the frequency-modulated laser, which generated a frequency-chirped heterodyne beat signal at the photodetector. This beat signal was compressed with a surface-acoustic-wave (SAW) dispersive delay line. The SAW device delayed the output relative to the input by an amount

168549-10

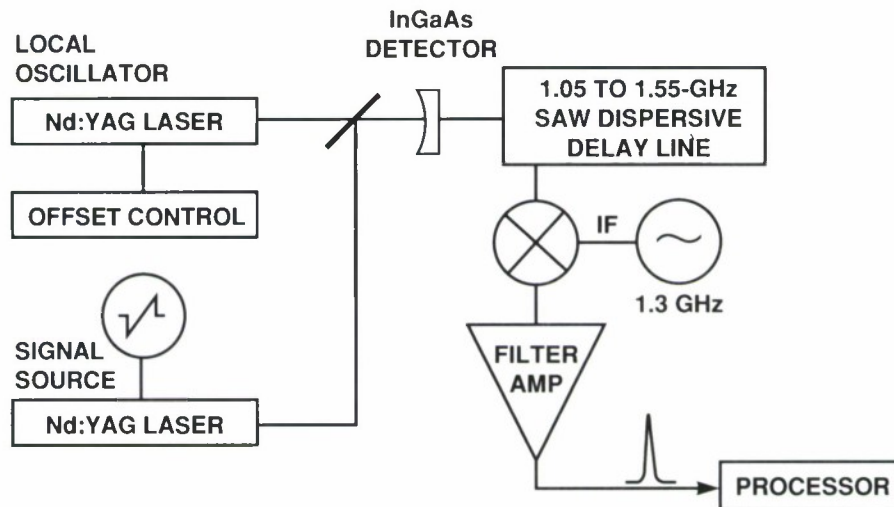
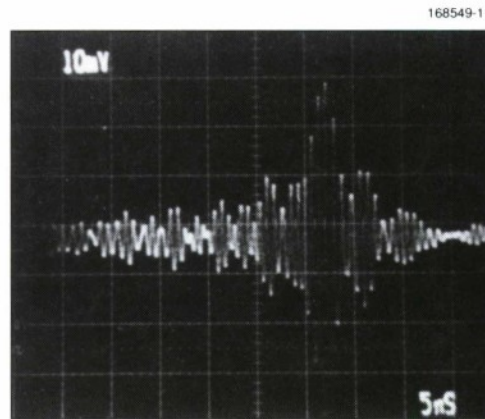
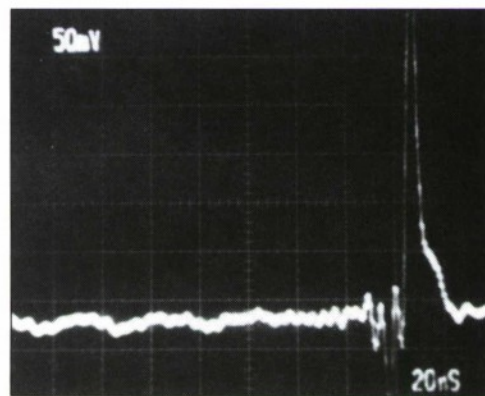


Figure 2-8. Schematic of an experiment to measure the linearity of the voltage-to-frequency conversion. The heterodyne signal of a 500-MHz linearly frequency-chirped Nd:YAG laser with a stable local oscillator is compressed with a SAW device to generate a ~ 2.5 - μ s, 1.3-GHz pulse. The output is mixed to zero frequency, amplified, and filtered.

linearly proportional to the input frequency for frequencies between 1.05 and 1.55 GHz. These SAW devices had a nonlinearity of less than 0.3 percent. The linear frequency chirp of our 12-MHz/V Nd:YAG laser was adjusted to 0.88 MHz/ns to match the SAW device, the goal being to generate a pulse whose duration would be the inverse of the bandwidth of the chirp. The SAW output consisted of a 1.3-GHz, 2.5-ns FWHM pulse, as shown in Figure 2-9(a), which is very close to the 2-ns limit imposed by the signal bandwidth. Thus, the voltage-to-frequency nonlinearity of the Nd:YAG laser is less than 0.5 percent as given by the ratio of the 2.5-ns pulse width to the 570-ns chirp duration.



(a)



(b)

Figure 2-9. Compression of a 500-MHz linearly frequency-chirped heterodyne signal. (a) Direct output from the SAW device demonstrating 2.5-ns FWHM pulse width, but with large sidelobes. (b) Output after frequency mixing to dc, amplifying, and filtering. This trace shows broadening and sidelobe rejection caused by the limited bandwidth of the amplifier. The sidelobes are -30 dB of the main peak. The FWHM pulse width is 4 ns.

Further signal processing consisted of mixing the signal with a 1.3-GHz intermediate frequency oscillator and amplifying the mixed output over a band from 0 to 100 MHz. Limiting the bandwidth increases the pulse width but reduces noise in the wings. The resulting signal [Figure 2-9(b)] was a 4-ns pulse with temporal sidelobes down by 30 dB and was near the 3-ns, 40-dB sidelobe limit [15] imposed by the 0.5-GHz chirp with Taylor filtering. The low sidelobes and good linearity bode well for the use of this technique in an analog, frequency-multiplexed coherent communications system where crosstalk between channels must be small. For coherent laser radar, a linearly chirped transmitter waveform is commonly used to obtain range-Doppler images of targets.

P.A. Schulz
S.R. Henion

2.5 ROOM-TEMPERATURE InGaAs-PUMPED Yb:YAG LASER

An efficient room-temperature ytterbium-doped YAG laser operating at $1.03\ \mu\text{m}$ has been developed, which is pumped by an InGaAs strained-layer diode laser operating at 968 nm. The Yb:YAG laser, which is made using a monolithic cavity design, has an external slope efficiency of 25 percent with 23-mW output power obtained for 430-mW incident pump power.

InGaAs-pumped Yb:YAG offers a number of advantages over AlGaAs-pumped Nd:YAG, including broader absorption features and lower thermal loading of the gain medium. A previous report [16] described an InGaAs-diode-pumped Yb:YAG laser that operated at low temperature (77 to 210 K). We now report efficient room-temperature operation of the InGaAs-pumped Yb:YAG laser, the first time to our knowledge that a bulk Yb^{3+} laser has been operated at 300 K.

The Yb:YAG laser was pumped with a single $100\text{-}\mu\text{m}$ -wide broad-area InGaAs diode laser emitting at 968 nm. The diode laser was mounted on a thermoelectric cooler for temperature control, and a gradient-index collimating lens with a numerical aperture of 0.6 and a focal length of 0.13 cm was positioned near the output facet of the diode (Figure 2-10). A 3.8-cm-focal-length cylindrical lens was used to compensate partially for the astigmatism caused by the difference between the diode far-field emission angles in the vertical and horizontal planes. The entire assembly was enclosed in a nitrogen-purged box so that the diode could be tuned from 960 to 975 nm by varying the temperature. The pump beam was focused into the Yb:YAG crystal by a 0.8-cm-focal-length lens. The antireflection coatings on the lenses were not optimized for 968 nm, so only half of the output of the diode laser was incident on the input face of the crystal.

The Yb:YAG laser consisted of a 1.65-mm-thick crystal with the surface facing the diode laser polished flat and the other surface ground to a 5-cm radius of curvature. The coating on the flat surface was greater than 99 percent reflective at $1.03\ \mu\text{m}$ and about 85 percent transmissive at 968 nm. The coating on the curved surface was 97 percent reflective at both $1.03\ \mu\text{m}$ and 968 nm, so that at least some of the pump light was double-passed through the gain region. The calculated TEM_{00} -mode radius for this cavity was $40\ \mu\text{m}$ and the pump spot at the crystal was measured to be anamorphic with equivalent $1/e^2$ radii of approximately 90 and $75\ \mu\text{m}$ in the horizontal and vertical planes, respectively.

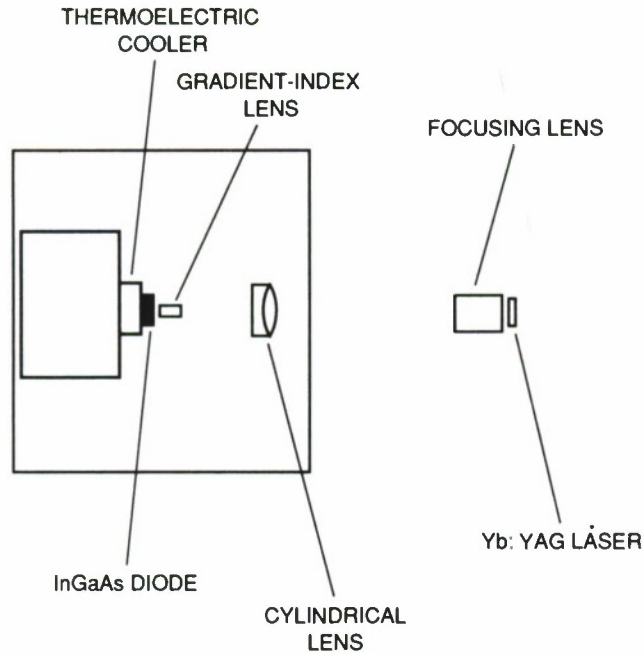


Figure 2-10. Diagram of the diode-pumped Yb:YAG laser.

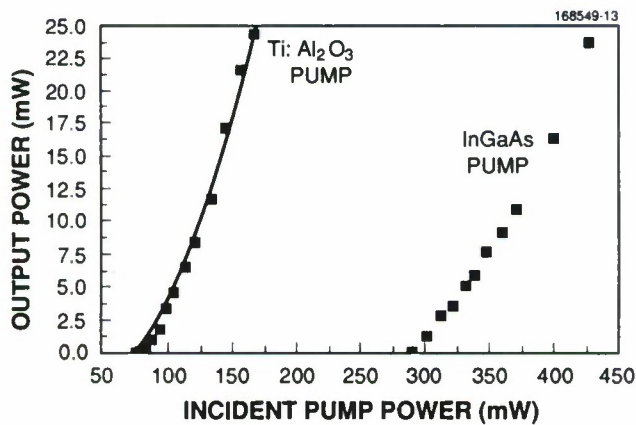


Figure 2-11. Output power versus input power for the monolithic Yb:YAG laser pumped by a Ti:Al₂O₃ laser and an InGaAs diode laser. The solid line is from the quasi-three-level laser model.

The output versus input of the Yb:YAG laser is shown in Figure 2-11. Note that the pump power is uncorrected for the transmission of the coating on the input surface of the crystal. The external slope efficiency was limited to about 25 percent because of the mismatch between the pump spot and the cavity mode sizes, the unoptimized output coupling, and the fact that the laser was only about 50 percent above threshold. Quasi-three-level lasers have lower slope efficiency close to threshold than four-level lasers, but their slope efficiency well above threshold approaches that of four-level lasers; as a result, slope efficiency for this laser will increase when additional pump power is available. Recabsorption loss dominates the laser threshold for the doping level, crystal length, and output coupling used in this work, so the slope efficiency can also be increased with only slightly higher threshold by raising the output coupling.

To model the Yb:YAG laser it is useful to examine the performance of the laser with a well-characterized pump, such as a TEM₀₀-mode Ti:Al₂O₃ laser. Figure 2-11 shows the output versus input for pumping at 941 nm, with the pump beam focused to a 20- μ m spot in the crystal. As shown in the figure, there is close agreement between the measured output and that predicted for the laser using the quasi-three-level laser theories of Fan and Byer [17] and Risk [18]. The exact value of the Yb³⁺ concentration in the model was varied to match the measured threshold. The best fit was obtained for a concentration of 8 at.%, somewhat higher than the nominal concentration of 6.5 at.%. With the pump power available, we achieved 33 percent external slope efficiency, limited mainly because the pump spot was smaller than the cavity mode [18]. Theory predicts that for matched pump and cavity modes the room-temperature Yb:YAG laser would have a slope efficiency of 70 percent at 3 times threshold.

In conclusion, we have demonstrated a room-temperature InGaAs-pumped Yb:YAG laser with 25 percent external slope efficiency. With Ti:Al₂O₃ pumping, an external slope efficiency of 33 percent was obtained. Higher-efficiency diode-pumped operation should be possible by optimizing the output coupling and by pumping many times above threshold with multiple diode lasers [19]. In this regime the advantages of Yb:YAG over Nd:YAG, including the absence of concentration quenching, longer fluorescence lifetime, and much smaller thermal loading, will outweigh the disadvantage of Yb³⁺ being a quasi-three-level laser.

P. Lacovara
T.Y. Fan

2.6 SINGLE-TRANSVERSE-MODE OPTICALLY PUMPED GaAs LASER WITH 500-W PEAK POWER

An optical converter to transform optical radiation with undesirable mode qualities into a more coherent optical beam is a device concept particularly relevant to high-power diode lasers. While diode laser arrays are capable of hundreds of watts of total output, the optical power in any single transverse mode is only a few watts. A fundamental limitation associated with the thin-film waveguide geometry of most diode lasers is the damage due to high optical intensity at the edge facets arising from the tight optical confinement in the dimension vertical to the junction. This results in a low rate of power scaling in the lateral dimension that is currently limited to ~ 0.1 W per micrometer of lateral wavefront. Even if successful control of the lateral mode can be achieved, the resulting vertical-lateral astigmatism is highly inconvenient. Using the geometry shown in Figure 2-12, we have developed an optical converter in a disk

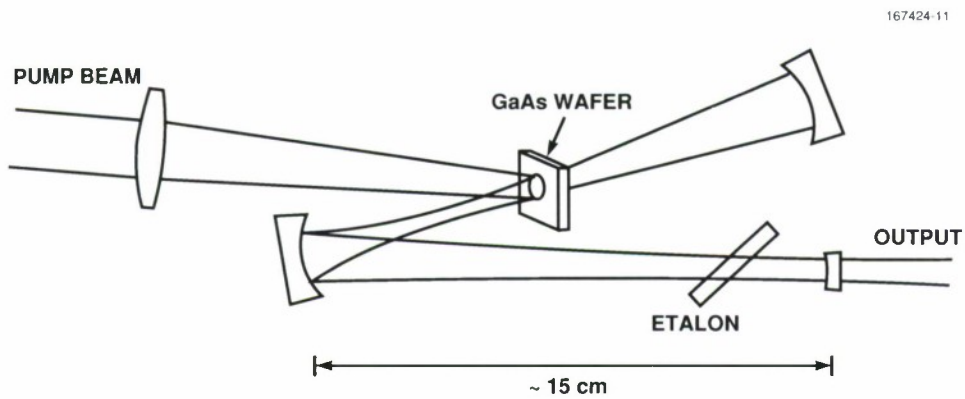


Figure 2-12. Diagram of a folded-cavity GaAs disk laser.

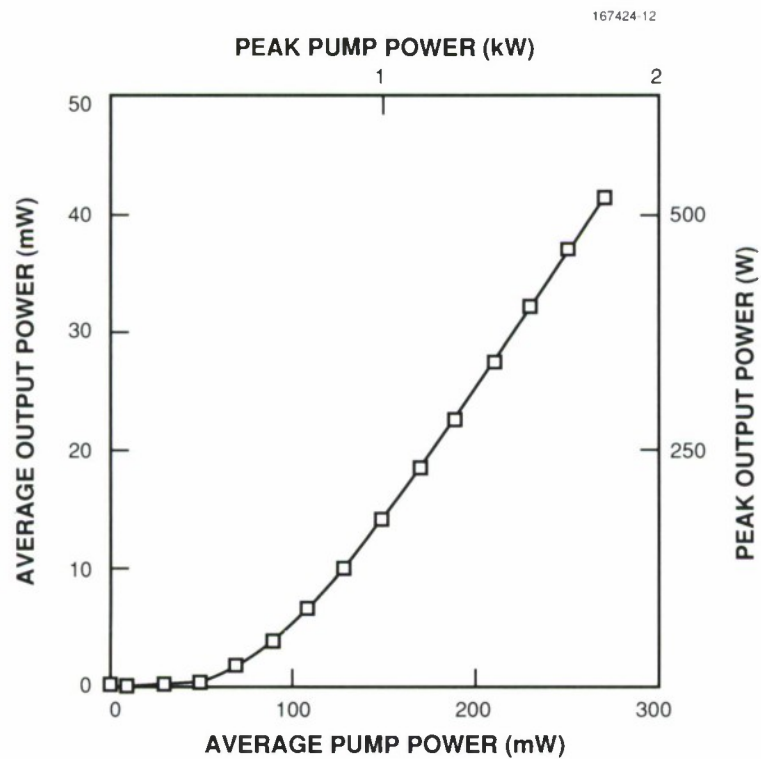


Figure 2-13. GaAs laser output power versus input pump power for a 120- μm -diam. pump spot. Peak power is derived using the measured pulse duration.

geometry that allows two-dimensional power scaling and avoids large astigmatism. Ideally, the optical power of a diode laser array can be focused into a circular region on a thin semiconductor platelet, which then serves as the gain medium in an external cavity, allowing control of the transverse mode.

The thin platelet is made from an n^+ -GaAs wafer, which is lapped to a thickness of $135\text{ }\mu\text{m}$ and antireflection coated at 890 nm on both sides. The wafer is mounted on an air-cooled copper heat sink with a 2-mm window. Simulated diode-laser-array pumping is obtained using a gain-switched $\text{Ti:Al}_2\text{O}_3$ laser with a 4-kHz repetition rate. The pump pulse duration is $\sim 38\text{ ns}$, which is much longer than the GaAs carrier lifetime, resulting in quasi-CW pumping conditions. The pump spot size is controlled by varying the position of the input lens, and the overlap between the optically excited gain region and laser cavity mode is controlled by moving the platelet along the laser axis. Power scaling is achieved by increasing the pump spot size while maintaining the intensity below the catastrophic damage threshold.

A nearly circularly symmetric output beam has been obtained with peak power up to 500 W and angular spread $< 0.5^\circ$. A plot of the output power versus pump power is shown in Figure 2-13, demonstrating a slope efficiency better than 20 percent and exhibiting no evidence of output saturation. The typical output intensity profile is shown in Figure 2-14 and is nearly symmetric. The spectral properties are shown in Figure 2-15. The $130\text{-}\mu\text{m}$ $1/e^2$ diameter of the pumped spot together with the $135\text{-}\mu\text{m}$ thickness result in an active volume equivalent to that of a hundred $200 \times 50 \times 1\text{-}\mu\text{m}$ laser diodes.

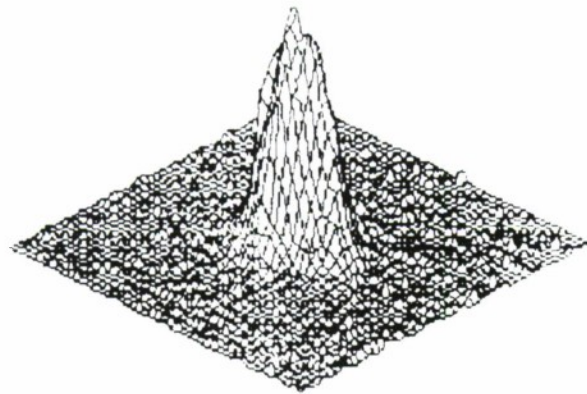
The peak power output of 500 W in a near- TEM_{00} mode is 2 orders of magnitude higher than the best previous results [20],[21] obtained in optically pumped III-V semiconductors. This laser design shows promise as a high-power optical converter. A key issue is the required pump density at threshold; for the 35 percent output coupler employed, the threshold density is only $4 \times 10^4\text{ W cm}^{-2}$ per micrometer of wafer thickness. Thus, for an epitaxially grown wafer of, say, $25\text{-}\mu\text{m}$ thickness, the required pump intensity is 10^6 W cm^{-2} , which is readily attainable with a linear laser array. Several optically excited disks can be integrated in an amplifier configuration, as shown in Figure 2-16, to convert the power of several laser diode bars into a high-power beam with desirable transverse-mode quality.

S. DiCecca
H.Q. Le
A. Mooradian

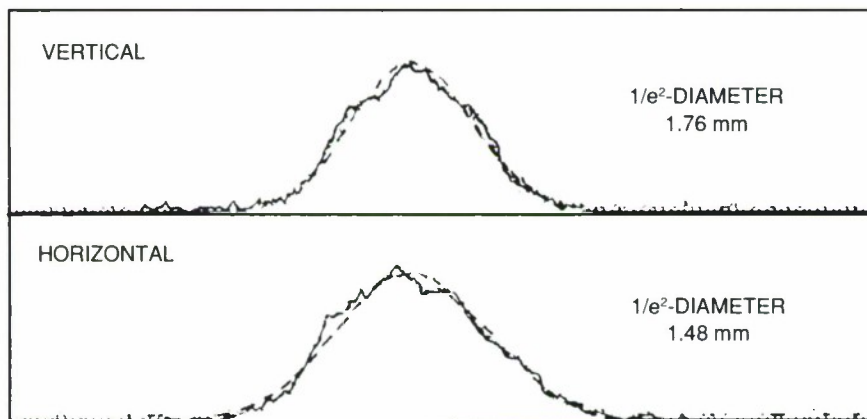
2.7 EFFICIENT COUPLING OF MULTIPLE HIGH-POWER DIODE LASER ARRAYS INTO A MULTIMODE OPTICAL FIBER

Five high-power diode laser arrays have been coupled into an optical fiber having a core-diameter/numerical-aperture product of $48\text{ }\mu\text{m}$, with 68 percent efficiency and 2.6-W output. An increase in the output power should be achievable from the same fiber with more arrays, and improvements in the optical system could lead to efficiency > 80 percent.

Diode lasers are efficient sources of laser radiation but have been limited to applications requiring relatively low power. Here, we demonstrate that five high-power diode laser arrays can be efficiently coupled into a multimode optical fiber by using an angular multiplexing technique [22]. In principle, many more than five arrays could be employed, and tens of watts of power could be obtained from a single fiber with incoherent multiarray input. This should allow diode lasers to be used in applications that require high power and a convenient delivery system.



(a)



(b)

Figure 2-14. (a) Intensity profile of output beam. (b) Cross-sectional intensity profile in the vertical and horizontal axes through the beam center. The dotted curves are Gaussian fits.

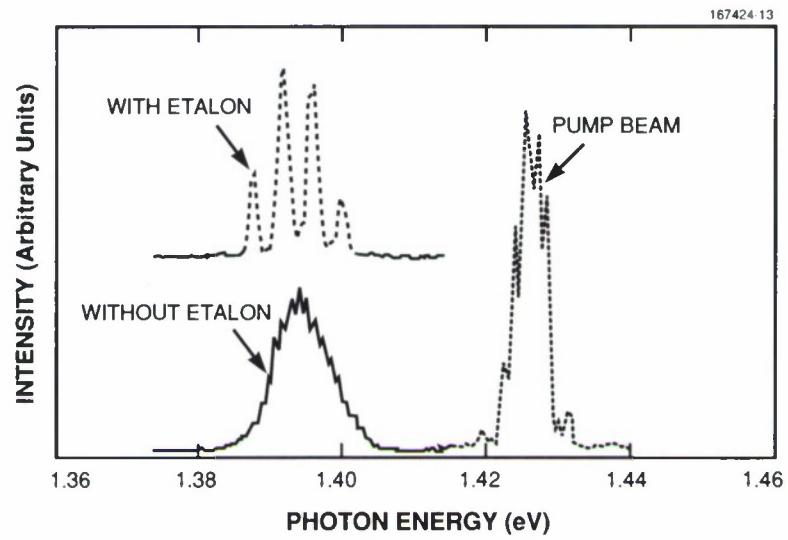


Figure 2-15. Output spectra of the GaAs laser with and without an etalon.

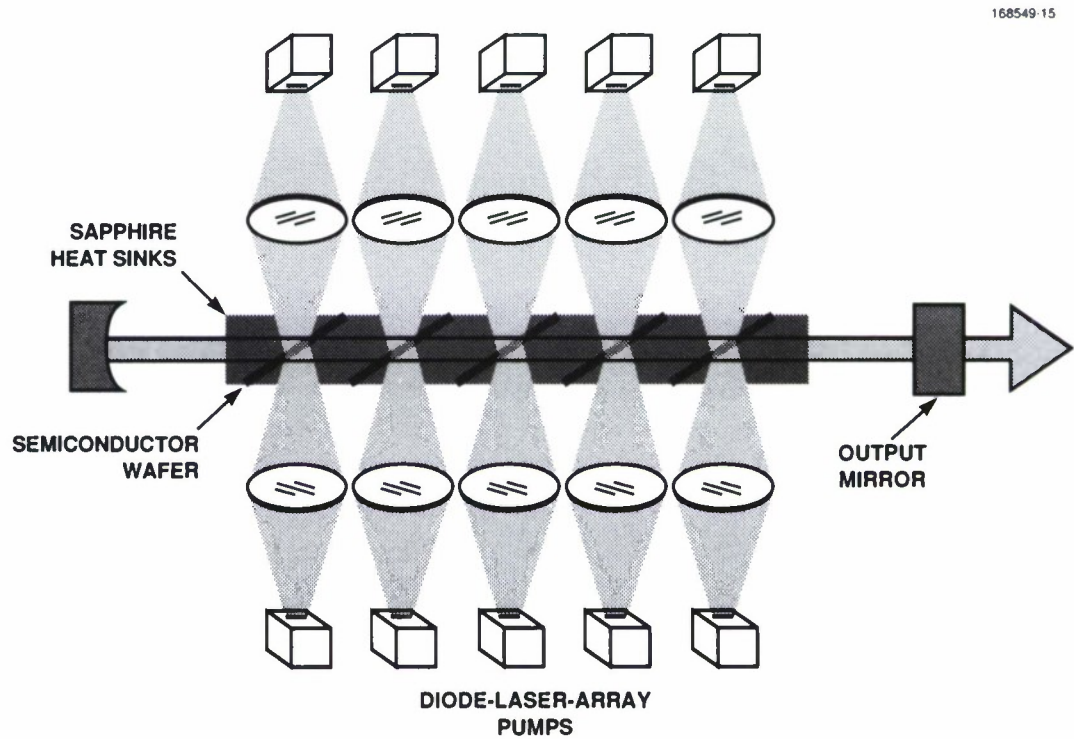


Figure 2-16. Schematic of a multiple-disk laser.

A schematic of the experiment using five GaAlAs diode laser arrays operating at 810 nm is shown in Figure 2-17. Each of these arrays is rated at nominally 1 W from a 200- μm -wide aperture and is collimated with a gradient-index lens having a numerical aperture of 0.6. The arrays are separated by 0.52 cm in the plane perpendicular to the junctions, and the collimating lenses are 0.18 cm in diameter. The beams pass through a 10-cm-focal-length doublet lens and a 6-cm-focal-length cylindrical lens that focus the beams into an optical fiber having a 400- μm core diameter and 0.12 numerical aperture. The results for coupling each array individually are shown in Table 2-1. For all arrays, 2.6 W of output was attained with 3.8 W incident on the fiber, for 68 percent overall coupling efficiency. Note that one diode laser array has lower power and coupling efficiency than the others; this array was not working properly. It should be possible to improve the coupling efficiency with antireflection coatings on the fiber input and output and the use of better coupling optics. Antireflection coatings would eliminate ~ 4 percent reflection loss at both the input and output of the fiber. It should also be possible to improve the optical alignment to achieve an overall efficiency as high as the best demonstrated from an individual array in this experiment. With these two improvements the overall efficiency would approach 85 percent.

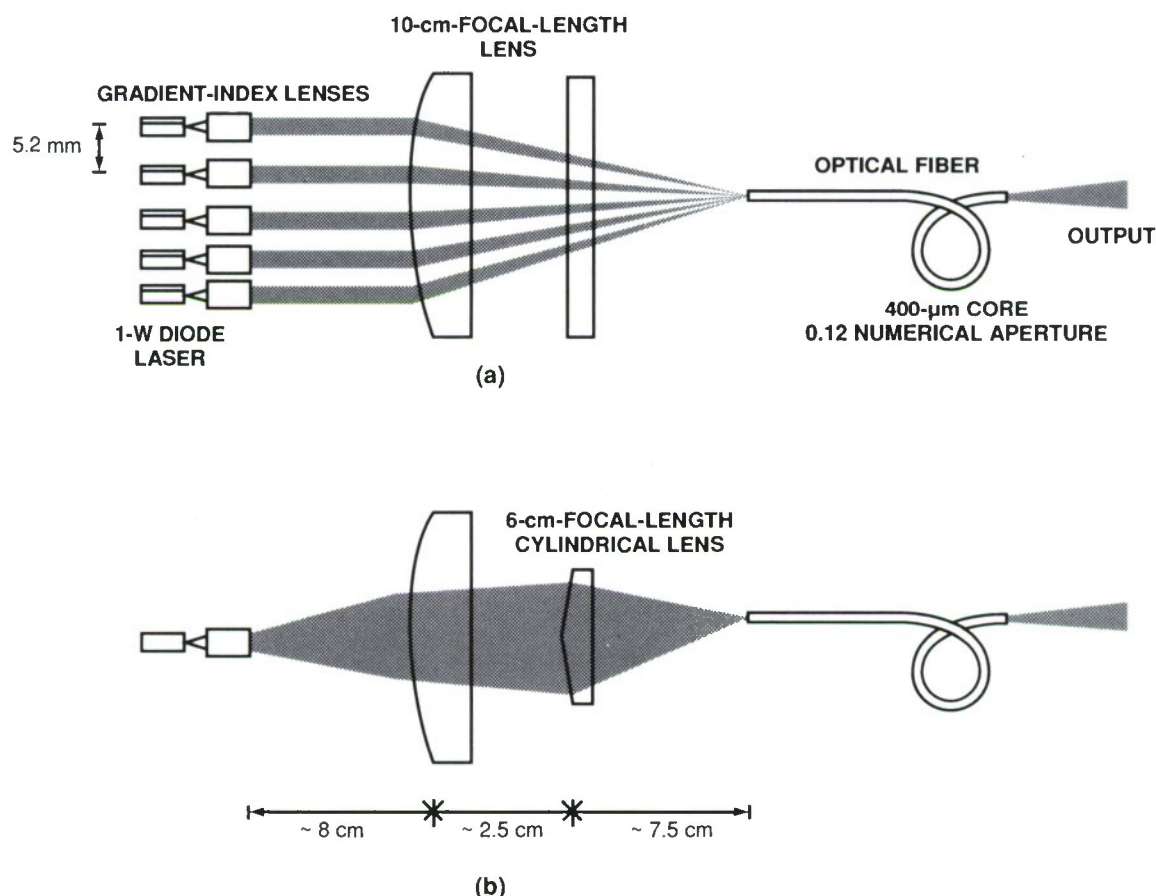


Figure 2-17. Schematic of multiple diode laser arrays coupled into a multimode fiber in planes (a) perpendicular and (b) parallel to the junctions of the diode laser arrays.

TABLE 2-1**Power and Efficiency Obtained with Coupling of Diode Laser Arrays to a Fiber**

Diode Laser Array	Input Power (W)	Output Power (W)	Efficiency (%)
1	0.835	0.620	74
2	0.880	0.630	72
3	0.820	0.545	66
4	0.840	0.540	64
5	0.430	0.240	56
All	3.8	2.6	68

Higher power can be expected with little change in the optical system shown here. A factor-of-2 higher power can be obtained by using a polarization beam combiner. We are also working on reducing the spacing between diode arrays in the plane perpendicular to the junction to allow higher packing density and fill factor. The theoretical upper bound for the number of these diode arrays that can be efficiently coupled to this particular fiber is of the order of 100 [22].

T.Y. Fan

REFERENCES

1. A.L. Schawlow and C.H. Townes, *Phys. Rev.* **12**, 1940 (1958).
2. M. Lax, in *Physics and Quantum Electronics*, P.L. Kelley, B. Lax, and P.E. Tannenwald, eds. (McGraw-Hill, New York, 1966), p. 735.
3. T.S. Jaseja, A. Javan, and C.H. Townes, *Phys. Rev. Lett.* **10**, 165 (1963).
4. J.J. Zayhowski and A. Mooradian, *Opt. Lett.* **14**, 24 (1989).
5. J.J. Zayhowski and A. Mooradian, *OSA Proc. Tunable Solid State Lasers* (Optical Society of America, Washington, D.C., 1989), p. 288.
6. J.J. Zayhowski, to be published in *OSA Proc. Advanced Solid State Lasers* (Optical Society of America, Washington D.C., 1990).
7. J.J. Zayhowski, J. Ochoa, and A. Mooradian, *Opt. Lett.* **14**, 1318 (1989); Solid State Research Report, Lincoln Laboratory, MIT, 1989:2, p. 21.

8. Solid State Research Report, Lincoln laboratory, MIT, 1990:3, p.19.
9. Solid State Research Report, Lincoln Laboratory, MIT, 1990:4, p. 18.
10. J.J. Zayhowski, to be published in *Lincoln Lab. J.*
11. Solid State Research Report, Lincoln Laboratory, MIT, 1990:2, p. 13.
12. A. Yariv and P. Yeh, *Optical Waves in Crystals* (Wiley, New York, 1984), p. 232.
13. I. Schulz, H. Welling, and R. Wallenstein, *OSA Proc. Advanced Solid State Lasers* (Optical Society of America, Washington, DC, 1990), p. 119.
14. This conclusion was obtained by integrating Equation (35) on p. 987 in A.E. Siegman, *Lasers* (University Science, Mill Valley, Calif., 1986).
15. E.C. Farnett and G.H. Stevens, in *Radar Handbook*, M. Skolnik, ed. (McGraw-Hill, New York, 1990), p. 10.31.
16. Solid State Research Report, Lincoln Laboratory, MIT, 1990:3, p. 17.
17. T.Y. Fan and R.L. Byer, *IEEE J. Quantum Electron.* **QE-23**, 605 (1987).
18. W.P. Risk, *J. Opt. Soc. Am. B* **5**, 1412 (1988).
19. T.Y. Fan, A. Sanchez, and W.E. DeFeo, *Opt. Lett.* **14**, 1057 (1989).
20. S.R. Chinn, J.A. Rossi, C.M. Wolfe, and A. Mooradian, *IEEE J. Quantum Electron.* **QE-9**, 294 (1973).
21. R.S. Putnam, C.B. Roxlo, M.M. Salour, S.H. Groves, and M.C. Plonko, *Appl. Phys. Lett.* **40**, 660 (1982).
22. Solid State Research Report, Lincoln Laboratory, MIT, 1990:1, p. 17.

3. MATERIALS RESEARCH

3.1 AlInGaAs/AlGaAs SEPARATE-CONFINEMENT HETEROSTRUCTURE STRAINED SINGLE-QUANTUM-WELL DIODE LASERS

Semiconductor diode lasers incorporating a strained InGaAs quantum-well active layer and AlGaAs confining layers grown on a GaAs substrate can exhibit significantly better performance [1] and reliability [2] than lasers that are similar in structure but have a lattice-matched, unstrained GaAs or AlGaAs active layer. Because the bulk bandgap of GaAs is reduced by the substitution of In for Ga, the InGaAs/AlGaAs lasers cannot have values of the emission wavelength λ less than about 890 nm. One proposed explanation for the improvement in reliability is that the propagation of defects in the active layer is retarded because the In atom is larger than the Ga, Al, and As atoms, which are almost the same size. On the basis of this explanation, we recently proposed [3] that it might be possible to improve the reliability of lasers with λ below 900 nm by using strained AlInGaAs active layers, in which the Ga in InGaAs is partially replaced by Al to increase the electron transition energy. As the first step in investigating this possibility, we fabricated [3] graded-index separate-confinement heterostructure single-quantum-well (GRIN-SCH SQW) $\text{Al}_y\text{In}_x\text{Ga}_{1-x-y}\text{As}/\text{AlGaAs}$ diode lasers with $0.05 \leq y \leq 0.17$ and $x = 0.13 \pm 0.01$. These devices, which had values of λ that decreased from 890 to 785 nm with increasing y , were comparable in pulsed performance to lasers with AlGaAs active layers.

We have now extended our investigation of AlInGaAs/AlGaAs strained-layer lasers by fabricating SCH SQW devices with an $\text{Al}_{0.18}\text{In}_{0.20}\text{Ga}_{0.62}\text{As}$ quantum-well active layer. These lasers, which emit at 814 to 818 nm, have lower values of threshold current density J_{th} than the earlier GRIN-SCH SQW devices. The results of initial reliability tests on the new lasers operated in the CW mode are quite encouraging.

To guide the development of the $\text{Al}_y\text{In}_x\text{Ga}_{1-x-y}\text{As}/\text{AlGaAs}$ lasers, we have calculated the energy at 300 K of the $n = 1$ electron to heavy hole transition as a function of AlAs mole fraction y and InAs mole fraction x for 10-nm-thick quantum wells with $\text{Al}_{0.3}\text{Ga}_{0.7}\text{As}$ confining layers. In Figure 3-1, the wavelength corresponding to the transition energy is plotted against x for values of y from 0 to 0.30 at intervals of 0.025. The wavelength values range from 660 nm to 1 μm . The calculations assume the following expression for the unstrained energy gap of $\text{Al}_y\text{In}_x\text{Ga}_{1-x-y}\text{As}$ alloys:

$$E_g = 1.42 + 1.455 y + 0.191 y^2 - 1.614 x + 0.55 x^2 + 0.043 xy \quad . \quad (3.1)$$

For $x = 0$, $y = 0$, and $x = 1 - y$, respectively, this equation gives reasonable agreement with the published expressions for the dependence of energy gap on composition for the $\text{Al}_y\text{Ga}_{1-y}\text{As}$ [4], $\text{In}_x\text{Ga}_{1-x}\text{As}$ [5], and $\text{Al}_y\text{In}_{1-y}\text{As}$ [6] alloys. The calculations take account of the increase in bulk energy gap resulting from the biaxial compressive strain and the increase in electron-hole transition energy associated with the quantization of the conduction and valence band energy levels. Unstrained lattice constants, elastic constants, and deformation potentials for the quaternary AlInGaAs alloys were obtained by linear interpolation from the published values for AlAs, InAs, and GaAs. The band offsets were obtained by linear interpolation from the offset values for GaAs/AlGaAs suggested by the data of [7] and for InGaAs/GaAs suggested by [5].

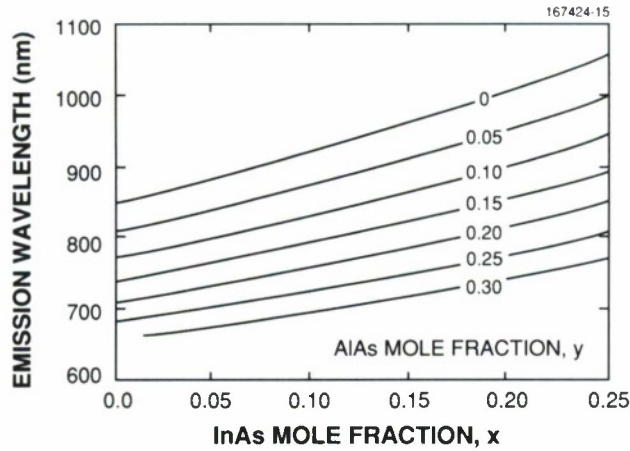


Figure 3-1. Dependence on x and y of wavelength corresponding to calculated electron-hole-transition energy for 10-nm-thick $\text{Al}_y\text{In}_x\text{Ga}_{1-x-y}\text{As}$ quantum wells with $\text{Al}_{0.3}\text{Ga}_{0.7}\text{As}$ confining layers.

The structure of the AlInGaAs/AlGaAs SCH-SQW lasers, which is shown schematically in Figure 3-2, consists of 1- μm -thick n - and p - $\text{Al}_{0.7}\text{Ga}_{0.3}\text{As}$ cladding layers, 85-nm-thick nominally undoped $\text{Al}_{0.25}\text{Ga}_{0.75}\text{As}$ confining layers, a nominally undoped 10-nm-thick $\text{Al}_{0.18}\text{In}_{0.20}\text{Ga}_{0.62}\text{As}$ active layer, a 20-nm-thick n^+ -GaAs buffer layer, and a 0.1- μm -thick p^+ -GaAs contact layer. All the interfaces except those of the quantum well were graded to reduce the series resistance. The structure was grown by organometallic vapor phase epitaxy in a vertical rotating-disk reactor operated at low pressure [8]. The substrates, source materials, and dopants were the same as those used in growing the AlInGaAs/AlGaAs GRIN-SCH SQW structures [3]. The SCH SQW laser structures were grown with a smaller difference in growth temperature between the AlGaAs cladding layers and the AlInGaAs active layer. As before, the AlGaAs cladding layers were grown at 800°C. During the growth of the lower confining layer, the temperature was reduced over a period of several minutes to a temperature T_a of 700, 725, or 750°C. The AlInGaAs active layer was grown at T_a , after which the temperature was raised to 800°C while the upper confining layer was being grown. Finally, the p^+ -GaAs cap layer was grown at 625°C to enhance Zn incorporation. Growth rates were typically 30 nm/min for the active, confining, and cap layers and 65 nm/min for other layers.

Broad-stripe lasers, with cavity widths of 150 or 200 μm and cavity lengths L ranging from 280 to 1500 μm , were fabricated by the same procedures used for the GRIN-SCH SQW devices [3]. The lasers were probe tested using 100-ns pulses at 1 kHz. Single-ended optical output power was measured with a calibrated Si photodiode detector.

From curves of light output versus pulsed current measured for three lasers with $L = 700 \mu\text{m}$ fabricated from wafers with active layers grown at $T_a = 700, 725, \text{ or } 750^\circ\text{C}$, the values of J_{th} were found to be

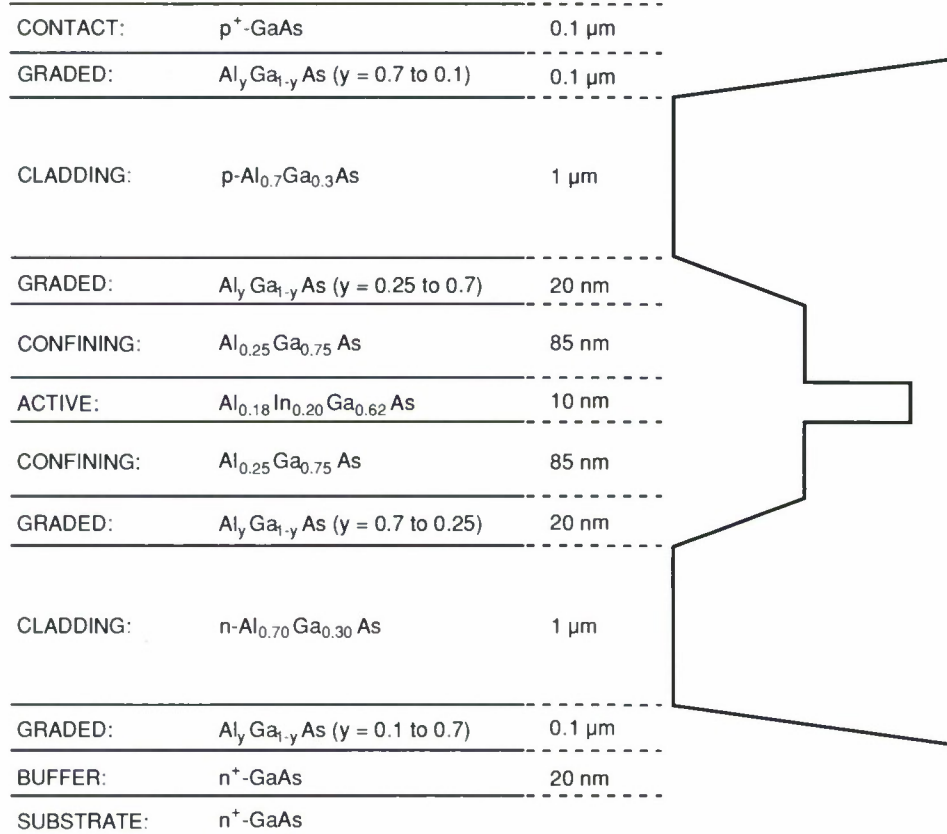


Figure 3-2. Schematic structure and energy diagram of AlInGaAs/AlGaAs SCH SQW diode laser.

146, 143, and 146 A cm⁻², respectively, and the values of the differential quantum efficiency η_d were 77, 74, and 79 percent, respectively. Thus, J_{th} and η_d are not significantly affected by T_a . The value of λ was 814 nm for the devices with $T_a = 725$ and 750°C , and 818 nm for the one with $T_a = 700^\circ\text{C}$. The difference in λ is probably due to a decrease in In incorporation with increasing T_a . The data reported below were obtained for devices with $T_a = 750^\circ\text{C}$.

The variation of J_{th} with $1/L$ is shown in Figure 3-3 for our best GaAs/AlGaAs and In_{0.2}Ga_{0.8}As/AlGaAs GRIN-SCH SQW lasers, with $\lambda = 852$ and 991 nm, respectively, and for Al_{0.18}In_{0.20}Ga_{0.62}As/AlGaAs SCH SQW lasers with $\lambda = 814$ nm. In all three cases, J_{th} exhibits the usual decrease with increasing L as a result of the decrease in end losses. For the AlInGaAs/AlGaAs device with $L = 1500 \mu\text{m}$, $J_{th} = 103$ A cm⁻². Although the structures differ somewhat in confinement and active layer thickness, we believe that the systematically lower J_{th} values of the AlInGaAs/AlGaAs lasers in comparison to the GaAs/AlGaAs devices show the basic advantage of the quaternary material, which is expected because of the effect of biaxial compressive strain on the valence band structure [5].

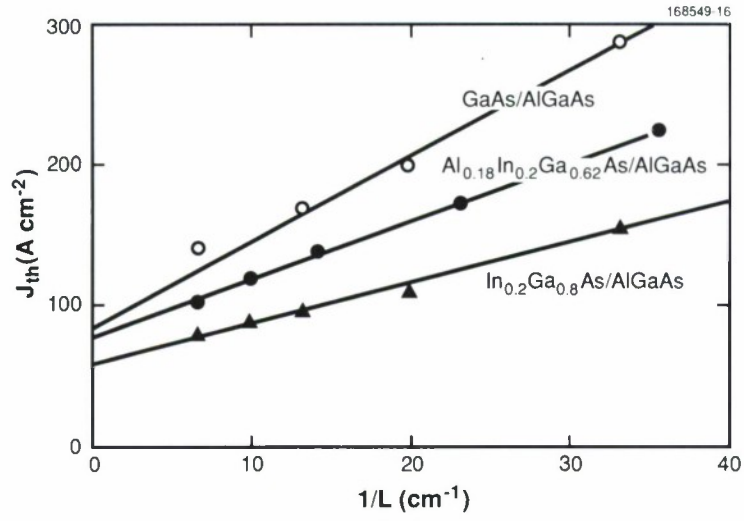


Figure 3-3. Threshold current density J_{th} of GaAs/AlGaAs, $Al_{0.18}In_{0.2}Ga_{0.62}As/AlGaAs$, and $In_{0.2}Ga_{0.8}As/AlGaAs$ diode lasers as a function of reciprocal cavity length $1/L$.

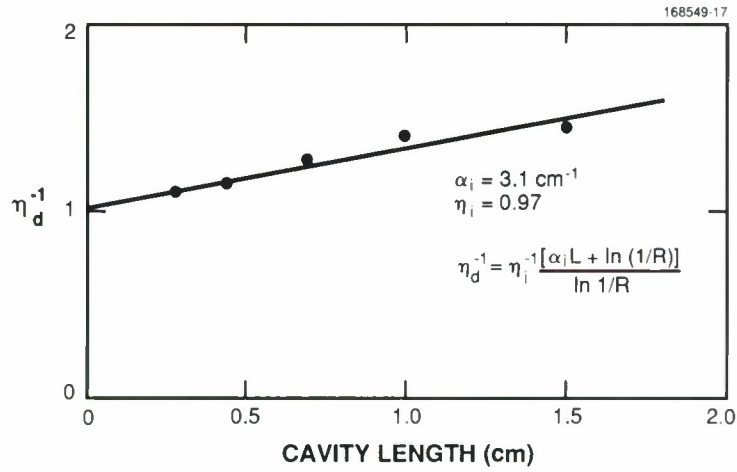


Figure 3-4. Reciprocal differential quantum efficiency η_d^{-1} as a function of cavity length L . The solid line is a least-squares fit.

In Figure 3-4, the reciprocal of η_d is plotted versus L for the AlInGaAs/AlGaAs SCH SQW lasers. The internal quantum efficiency η_i and the intrinsic mode loss coefficient α_i are found to be 0.97 and 3.1 cm^{-1} , respectively. These values are typical of our GaAs/AlGaAs and InGaAs/AlGaAs GRIN-SCH SQW lasers. From the measured temperature dependence of J_{th} for AlInGaAs/AlGaAs SCH SQW lasers with $L = 700 \text{ }\mu\text{m}$, the characteristic temperature T_0 in the expression $J_{th} = J_0 \exp(T/T_0)$ is found to be 214 K for the range from 10 to 40°C and 159 K for the range from 40 to 60°C. These values are comparable to those for GaAs/AlGaAs quantum-well lasers.

In preliminary reliability tests of the SCH SQW lasers, uncoated broad-area devices were tested under both low and high CW power. A device with saw-cut side walls was mounted junction side down and operated at a constant current of 180 mA, 1.18 times the initial threshold current. During 163 hours of operation, J_{th} changed from 152 to 162 mA, an increase of 6.6 percent. High-power operation of a device measuring $500 \text{ }\mu\text{m} \times 1 \text{ mm}$ with wet-etched sidewalls was performed at a constant output power of 1 W/facet. After 50 h, the current had increased from its initial value of 2.64 A, 3.5 times the initial threshold current, to 2.76 A, a change of only 4.5 percent. These results suggest that AlInGaAs/AlGaAs lasers will prove to be significantly more reliable than GaAs/AlGaAs or AlGaAs/AlGaAs devices.

C.A. Wang	J.P. Donnelly
J.N. Walpole	H.K. Choi
L.J. Missaggia	

3.2 TIME DEPENDENCE OF AlGaAs MBE GROWTH RATES DETERMINED BY FREQUENCY-DOMAIN ANALYSIS OF RHEED OSCILLATION DATA

For the analysis of reflection high-energy electron diffraction (RHEED) oscillation data obtained during growth by molecular beam epitaxy (MBE), frequency-domain techniques [9],[10] such as the fast Fourier transform offer a number of advantages over the conventional time-domain method, which utilizes graphical analysis of intensity-versus-time plots. The frequency-domain techniques permit the oscillation frequency to be determined more rapidly and precisely, to be evaluated from even a single oscillation, and to be extracted from data that cannot be analyzed by the conventional technique because the oscillations are too weak to be detected by visual inspection. The latter capability permits the assessment of the validity of an assumption that is often made in performing MBE growth experiments, namely, that the growth rate determined from RHEED oscillations observed in the early stages of growth is the same as the rate during the later stages, when oscillations are no longer visible. In the investigation reported here, we have found that this assumption is not valid for the MBE growth of AlGaAs at temperatures above 700°C, since the RHEED oscillation frequency decreases substantially during deposition of the first few monolayers.

A 75-mm MBE system was used for the growth of AlGaAs and GaAs layers on semi-insulating GaAs substrates bonded with In to Mo mounting blocks. The substrates were prepared by chemical cleaning and etching followed by oxide desorption at $\sim 600^\circ\text{C}$ in the MBE growth chamber under an As flux. Substrate temperatures were measured with a narrow-band optical pyrometer positioned to view the substrate in the growth position. Relative substrate temperatures were monitored with a thermocouple located below the mounting block. The steady-state Ga and Al source fluxes were adjusted to give GaAs growth rates of 0.9 to $1.0 \text{ }\mu\text{m/h}$ and AlAs growth rates of 0.3 to $0.4 \text{ }\mu\text{m/h}$. Beam-equivalent pressures for the Ga, Al, and As fluxes were determined from readings on an ion gauge located in the growth position.

Initial Ga and Al flux transients were determined by computerized recording of the ion gauge readings for a few minutes after the opening of the source shutters. The Ga and Al fluxes decreased by less than 2 and 5 percent, respectively. The As_4 flux was varied to give uncorrected V/III ratios between 7 and 20.

The computerized measurement system used for frequency-domain analysis has been described previously [9]. Briefly, the system is based on the observation of RHEED intensities by a television camera focused on the phosphor screen. The intensity data for a selected pixel are digitized and read into a desktop computer for frequency analysis. In each frequency determination, data are collected for 30 or 60 s at rates of 70 and 30 samples/s, respectively, then analyzed to obtain the power spectrum, after which a simple peak location algorithm is employed to extract the frequency. For these times and sampling rates it is predicted that the frequency can be measured with an uncertainty as low as ± 0.003 Hz. The uncertainty is higher for especially noisy spectra.

In performing a set of oscillation frequency measurements, a GaAs buffer layer at least $1\text{ }\mu\text{m}$ thick was first deposited on the substrate at $\sim 550^\circ\text{C}$, followed in most cases by deposition of $\sim 0.1\text{ }\mu\text{m}$ of AlGaAs at this temperature. The Al and Ga shutters were then closed for ~ 30 s, data collection was started, the Al and Ga shutters were reopened, and intensity data for the specular reflection in the (011) azimuth were collected for the desired time. The substrate temperature was then increased and allowed to stabilize, the Al and Ga shutters were closed, and the procedure was repeated. As-stabilized surface reconstructions were maintained. Generally, the experiments were performed at a series of successively higher temperatures. In experiments at temperatures below 700°C , the frequency was found to be the same for AlGaAs growth directly on GaAs as for growth on an AlGaAs layer; at higher temperatures, growth could not be performed directly on GaAs because of the difficulty of maintaining an As-stabilized GaAs surface.

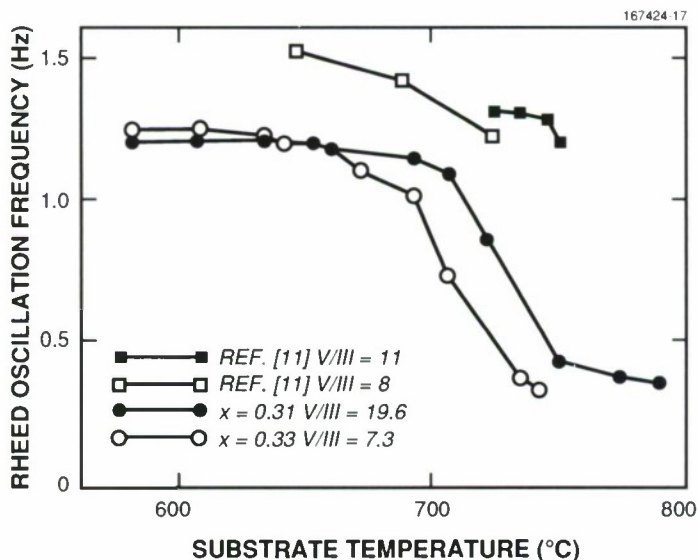


Figure 3-5. RHEED oscillation frequency versus substrate temperature for growth of AlGaAs. For data represented by circles and squares, frequencies were obtained by frequency-domain and time-domain analyses, respectively.

In Figure 3-5, the RHEED oscillation frequencies measured in two sets of AlGaAs growth experiments are plotted against substrate temperature over the range from 580 to 790°C. In one set of experiments the V/III beam-equivalent pressure ratio was 7.3 and the ratio of Al flux to the total group III flux was 0.31 (yielding $\text{Al}_x\text{Ga}_{1-x}\text{As}$ layers with $x = 0.31$ if the sticking coefficient is unity for both Ga and Al), while in the other set these ratios were 19 and 0.33, respectively. The frequency values were obtained by analysis of data collected for 60 s after opening the Ga and Al shutters. As previously reported [3], the persistence of the observed oscillations varied with substrate temperature, with the oscillations most clearly visible in the high-temperature and low-temperature regimes. With increasing temperature, the measured frequency is nearly constant up to $\sim 650^\circ\text{C}$, then decreases strongly as the growth rate decreases because of Ga desorption from the growing surface. The ratio of the growth rates at the highest and lowest temperatures approximates the ratio of the Al flux to the total group III flux, showing that the layers grown at the highest temperatures probably consist almost entirely of AlAs. This variation in growth rate with temperature is not shown as clearly by the earlier data of Ralston et al. [11], which are plotted in Figure 3-5 for comparison.

In another set of AlGaAs growth experiments, which were performed under conditions similar to those used in obtaining the results shown in Figure 3-5 for the lower V/III ratio, data were collected for 30 s after opening the Ga and Al shutters. For each substrate temperature, oscillation frequencies were determined by analyzing the data collected from 10 to 30 s as well as by analyzing the data for the entire 30 s. The results are shown in Figure 3-6. For temperatures below 700°C the frequencies obtained for the

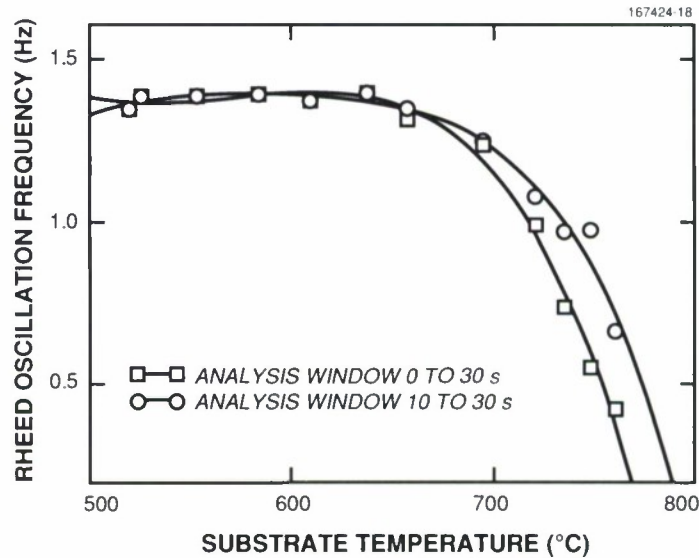


Figure 3-6. RHEED oscillation frequency versus substrate temperature for growth of AlGaAs. For data represented by circles and squares, frequencies were obtained by frequency-domain analysis of data collected for 0 to 30 s and 10 to 30 s, respectively, after opening the Al and Ga source shutters.

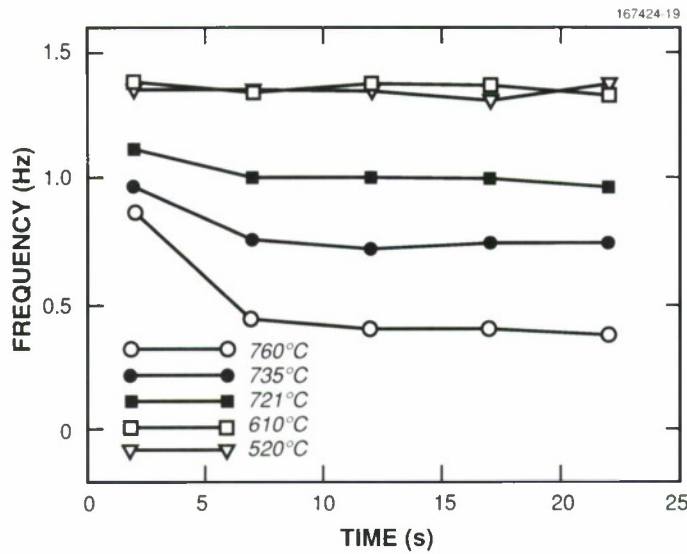


Figure 3-7. RHEED oscillation frequency versus time following source-shutter opening for AlGaAs growth at substrate temperatures from 520 to 760°C. Frequencies were obtained by frequency-domain analysis of data collected for 5-s periods.

two analysis windows are the same. For higher temperatures, however, the values are lower for the 10- to 30-s window than for the 0- to 30-s window, showing that the growth rate during the first 10 s was greater than the steady-state rate.

To investigate the time evolution of the growth rate in greater detail, experiments were performed at temperatures from 520 to 760°C in which analysis windows of 5 s were used in analyzing data taken for 30 s after opening the Ga and Al shutters. The results are shown in Figure 3-7. At temperatures below 700°C the growth rate does not change with time, but at the higher temperatures the initial rate is higher than the steady-state value by an amount that increases with increasing temperature. At 760°C, the initial rate is about twice the steady-state value. The changes in growth rate (and therefore in composition) are much too large to be attributed to flux transients. This observation indicates the existence of complex interactions among the surface atoms that should be addressed in future investigations of the epitaxial growth of AlGaAs layers, and it suggests that frequency-domain analysis of RHEED oscillation data should also be used to measure the time evolution of epitaxial growth for other materials systems.

G.W. Turner
S.J. Eglash

REFERENCES

1. H.K. Choi and C.A. Wang, *Appl. Phys. Lett.* **57**, 321 (1990).
2. D.P. Bour, D.B. Gilbert, K.B. Fabian, J.P. Bednarz, and M. Ettenberg, *IEEE Photon. Technol. Lett.* **2**, 173 (1990).
3. C.A. Wang, J.N. Walpole, H.K. Choi, and L.J. Missaggia, to be published in *IEEE Photon. Technol. Lett.*
4. T.F. Kuech, D.J. Welford, R. Potemski, J.A. Bradley, K.H. Kelleher, D. Yan, J.P. Farrell, P.M.S. Lesser, and F.H. Pollak, *Appl. Phys. Lett.* **51**, 505 (1987).
5. R.M. Kolbas, N.G. Anderson, W.D. Laidig, Y. Sun, Y.C. Lo, K.Y. Hsieh, and Y.J. Yang, *IEEE J. Quantum Electron.* **24**, 1605 (1988).
6. H.C. Casey, Jr. and M.B. Panish, *Heterostructure Lasers Part B: Materials and Operating Characteristics* (Academic, New York, 1978), p. 16.
7. K.W. Goossen, S.A. Lyon, and K. Alavi, *Phys. Rev. B* **36**, 9370 (1988).
8. C.A. Wang and H.K. Choi, *J. Electron. Mater.* **18**, 1695 (1989).
9. G.W. Turner, B.N. Nechay, and S.J. Eglash, *J. Vac. Sci. Technol. B* **8**, 283 (1990).
10. J.S. Resh, K.D. Jamison, J. Strozier, and A. Ignatiev, *Rev. Sci. Instrum.* **61**, 771 (1990).
11. J. Ralston, G.W. Wicks, and L.F. Eastman, *J. Vac. Sci. Technol. B* **4**, 594 (1986).

4. SUBMICROMETER TECHNOLOGY

4.1 DIFFUSION PROCESSES DURING RESIST SILYLATION

Advances in optical lithography to resolutions below $0.5\ \mu\text{m}$ have required the development of new resist technologies. Among these, surface-imaging techniques [1], exemplified by silylation processes, are being pursued extensively. In initial work, materials and processes have been developed for g- and i-line lithography based on novolac/diazoquinone photoresists [2]. The mechanism for selective silylation has been studied [3],[4] and is essentially due to thermal crosslinking by the diazoquinone in the unexposed areas of the resist film. These materials may also be used at 248 nm [5] since the strong absorption of novolac is not a detriment for surface imaging. Additional silylation processes for deep-UV lithography have been developed that rely upon acid-catalyzed crosslinking [6],[7] and are thus positive tone, exhibiting high sensitivity.

We have developed a silylation process for 193-nm-based lithography that is also positive tone because of resist crosslinking by the exposing radiation [8],[9]. Crosslinking occurs in acid-catalyzed and novolac/diazoquinone-type photoresists as well as in novolac resins without additives.

Conventional silylation processes such as the DESIRE (diffusion-enhanced silylated resist) system [2] use hexamethyldisilazane (HMDS) as a silylating reagent and require high temperatures to provide adequate crosslinking of the unexposed areas and rapid diffusion of the HMDS. For the 193-nm process, however, thermal crosslinking must be avoided, so a smaller silylating agent is used. Generally, dimethylsilyldimethylamine is employed since it diffuses to an adequate extent at temperatures below 100°C . This report examines the silylation process developed for 193-nm lithography in greater detail. In particular, the mechanism of the diffusion process and phenomena that may affect process control are discussed.

Figure 4-1 shows schematically the difference between negative- and positive-tone silylation processes. For a negative-tone process, the presilylation baking step thermally crosslinks the material in the areas in which light has not converted the diazoquinone to a carboxylic acid. During the silylation process the silicon diffuses readily into the uncrosslinked regions but does not diffuse appreciably into the unexposed regions that are thermally crosslinked. The profile of the silylated regions is therefore defined by the exposure image and becomes a function of the projection tool used for patterning.

For the positive-tone process, the crosslinked regions are confined to the vicinity of the resist surface. The depth of crosslinking depends upon the absorbance of the resist at the exposing wavelength; for typical novolac resists exposed to 193-nm radiation this corresponds to about $750\ \text{\AA}$ of crosslinking [8]. As the silylating agent diffuses into the film, the crosslinking at the surface serves as a screen to prevent diffusion into the exposed areas. If the film is silylated to a depth greater than the depth of crosslinking, however, the isotropic nature of the diffusion process should lead to diffusion beneath the surface-crosslinked regions. After reactive ion etching, this would lead to an inability to pattern small features (those comparable to the diffusion depth) or to poor linewidth control for larger features.

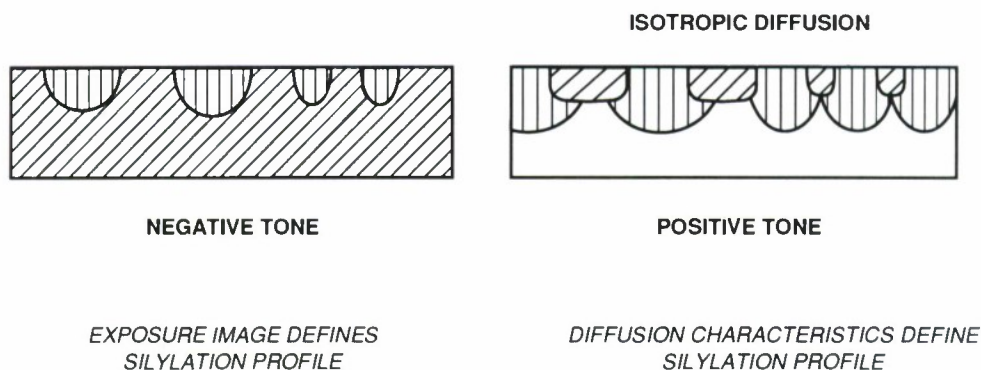


Figure 4-1. Schematic of silicon profiles for negative- and positive-tone silylation processes. Regions of crosslinking are shown by diagonal shading, and the silylated areas are represented by vertical shading.

In this investigation, scanning Auger electron spectroscopy measurements were made on a grating structure patterned in a pure novolac resin (FSC). The grating had nominally 5- μm lines and spaces and was contact printed. The width of the silylated regions could be determined from the Auger signal for silicon, and this width was measured at different depths by sputtering the sample between scans. The measured profile is shown in Figure 4-2, along with a representation of isotropic diffusion (the dashed line appears anisotropic because of the difference in scale between the x and y axes).

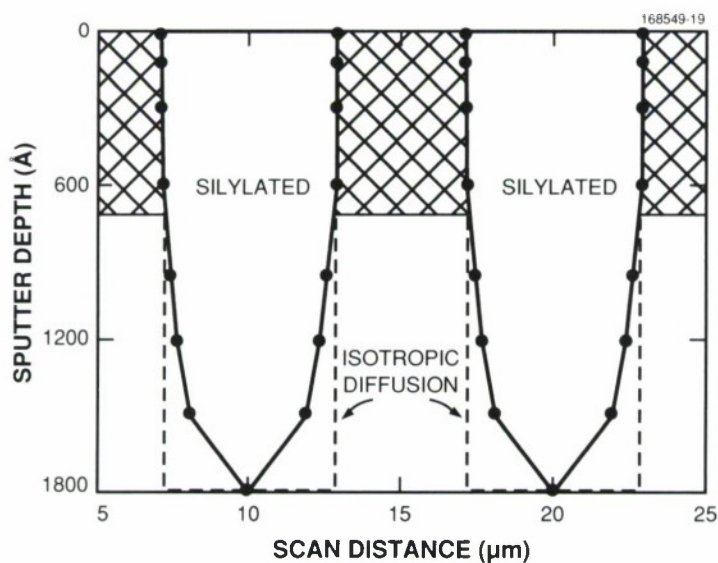


Figure 4-2. Scanning Auger depth-profile of a grating structure with 5- μm lines and spaces patterned in FSC resist, exposed at 100 mJ cm^{-2} , and silylated at 100°C for 1 min at 10-Torr pressure. The crosslinked region, denoted by crosshatching, extends 75 nm into the film.

It is apparent from Figure 4-2 that the diffusion occurs most rapidly in the center of the grating structure and is slower near the boundary between the crosslinked and uncrosslinked regions. One possible explanation for this behavior is that the diffusion is hindered in the unexposed material adjacent to the crosslinked regions, although the unexposed material is not itself crosslinked. If relaxation of the polymer plays an important role in the diffusion process, the crosslinked regions could restrict the chain mobility in the unexposed regions to a degree sufficient to retard the diffusion process. The polymers also show some swelling as the silylating agent penetrates, and the crosslinked regions can restrict the amount of swelling. This effect is shown schematically in Figure 4-3.

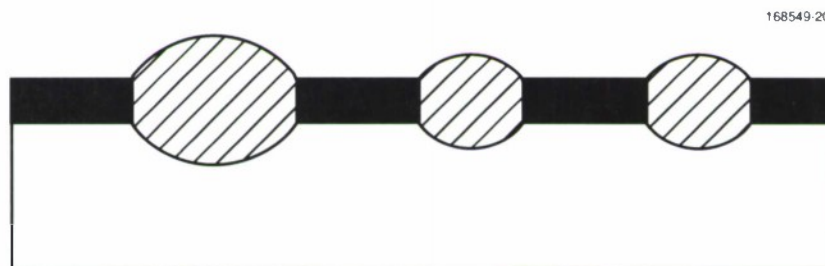


Figure 4-3. Schematic of swelling constraints imposed by the exposed crosslinked regions. The filled areas represent the crosslinked regions and the diagonal shading denotes the swollen silylated areas.

The diffusion of organic vapors into polymers is often controlled by the relaxation rate of the polymer, which must reorient to accommodate the diffusing species. If the time scale for this process is on the order of the time scale for diffusion, then anomalous diffusion occurs, generally termed case II diffusion. The diffusion rate for case II diffusion is no longer determined by the diffusion constant but by the amount of stress created between the swollen surface layer and the unswollen original polymer film. Since the crosslinked regions restrict the amount of swelling that occurs, this will limit the penetration of the silylating agent. The restriction depends on the distance of a particular region from the crosslinked site, and thus swelling and diffusion are maximum at the midpoint between crosslinked regions, where this restriction is minimized. This result also leads to a proximity effect, where the amount of silicon that diffuses into a given unexposed area is a function of the size of that area and the proximity of a crosslinked region.

The extent of the crosslinking in the exposed regions should also limit the amount of swelling, and therefore diffusion, that will occur. As a means of verifying this, a series of gratings was patterned into SAL 601 resist at different doses. While the nominal exposure dose required to prevent silylation is 10 mJ cm^{-2} , additional samples were exposed at doses as high as 100 mJ cm^{-2} . A previous study [10] has shown that the nominal dose for exposure reacts only a fraction of the photoacid generator and melamine crosslinking agent in a similar resist, and the conversion is roughly linear up to 500 mJ cm^{-2} . Thus, a ten-fold increase in crosslinking should be seen by increasing the dose from 10 to 100 mJ cm^{-2} .

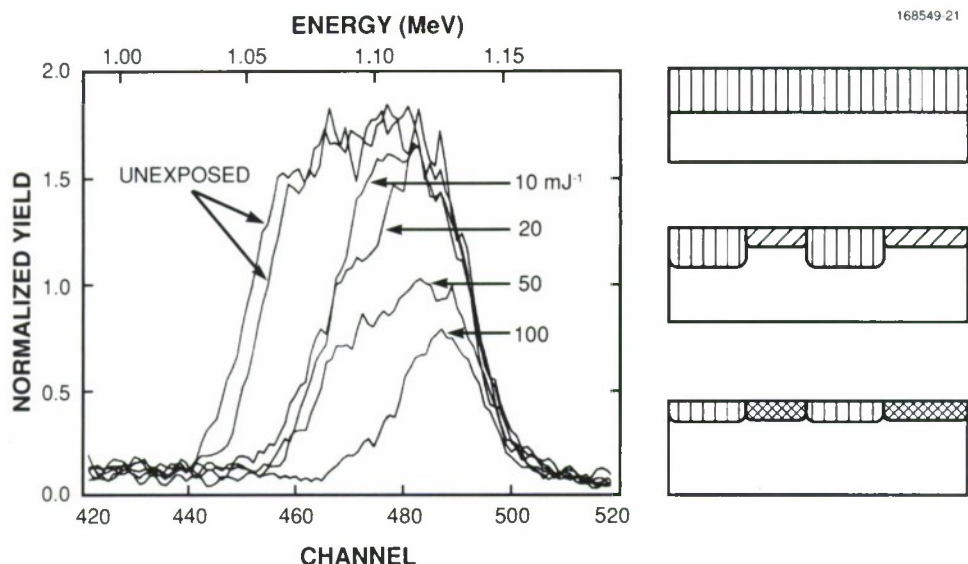


Figure 4-4. Comparison of Si yield from RBS spectra for a grating structure with 3- μm lines and spaces patterned in SAL 601, exposed at doses from 10 to 100 mJ cm^{-2} , and silylated at 90°C for 1 min at 10-Torr pressure. Schematic diagram of diffusion profile based on RBS interpretation is shown at the right, with the diagonal shading denoting crosslinking, the crosshatching representing a higher degree of crosslinking, and the vertical shading denoting silylated areas.

Rutherford backscattering spectra (RBS) for the samples exposed at different doses, as well as for unexposed samples, are shown in Figure 4-4. The silylation conditions resulted in incorporation of silicon to a depth of 225 nm in the unexposed resist. The amount of silicon incorporation shown in Figure 4-4 decreases as the dose used to expose the grating increases. The decrease in yield represents the fraction of the surface area that is crosslinked by the exposure. Scanning electron microscopy measurements were made of the grating structures after oxygen reactive ion etching, and good agreement was found between the measured linewidths and the decrease in the RBS signal. More significant is the shallower depth of silicon incorporation found at higher doses, particularly at 100 mJ cm^{-2} . At this dose, the silicon penetrates only 120 nm in the unexposed areas. Three schematic cross sections are shown in Figure 4-4, depicting the interpretation of the RBS spectra. From these data it is clear that the diffusion in unexposed regions of the film can indeed be affected by crosslinking in adjacent areas.

In summary, the silylation process developed for 193-nm-exposed resists differs significantly from the typical negative-tone process used for longer-wavelength exposure. The silylation profile in the resist for a positive-tone process is determined by the diffusion characteristics rather than the latent exposure image. The incorporation of silicon does not occur isotropically but is faster in the center of unexposed regions. This behavior appears to be due to the restriction in swelling caused by the crosslinked areas. Increased crosslinking in the exposed sites further restricts the diffusion in the nearby unexposed portions of the resist.

M.A. Hartney

4.2 EXCIMER-LASER-INDUCED CHANGES IN FUSED SILICA

The short wavelength and high spectral brightness of excimer lasers have made them attractive as potential photon sources for deep-UV optical lithography. Several groups have demonstrated sub-0.5- μm printing capabilities using 248-nm (KrF) and 193-nm (ArF) lasers. Recently, 248-nm steppers have become commercially available from several manufacturers. Research is now under way to explore the feasibility of producing steppers at 193 nm. However, a major area of uncertainty is the degree of stability of the optical elements on prolonged excimer irradiation.

In earlier work [11], two 193-nm-induced effects were observed in fused silica, as seen Figure 4-5. One was the growth of absorptive features in the UV, mainly a structure peaked at ~ 215 nm. This peak was correlated to the formation of point defects commonly referred to as E' centers. These centers are

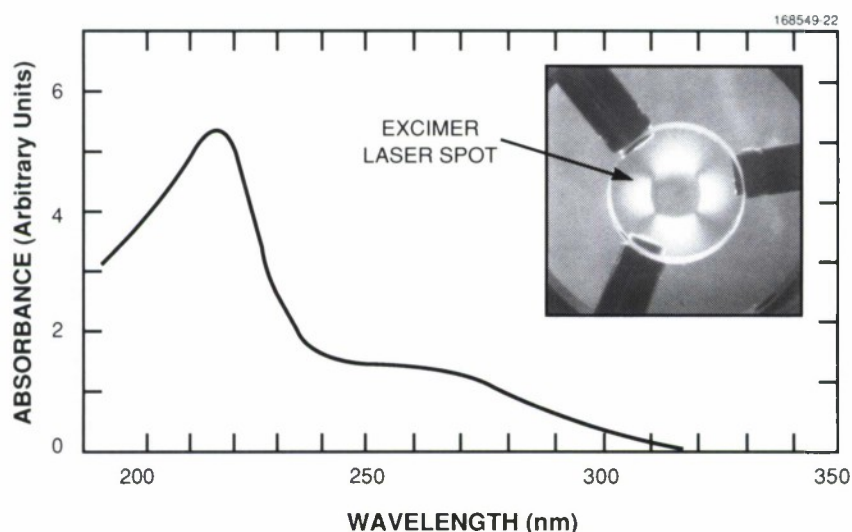


Figure 4-5. Excimer-laser-induced absorption spectrum in fused silica and (inset) birefringence as evidenced by the transmitted 633-nm light when the sample was placed between two crossed linear polarizers. Note that the birefringent zone surrounds the excimer laser spot.

positively charged oxygen vacancies and can be generated by x-ray or e-beam exposure. The other effect was birefringence in areas adjacent to the irradiated volume. The birefringence was attributed to compressive stresses, and from this result it was inferred that the laser-irradiated zone undergoes compaction. The relationship between the formation of E' centers and compaction has been the subject of further studies, the results of which are reported here.

Samples of fused silica grown and annealed under various conditions were exposed to a 193-nm laser. The samples, typically 25-mm-diam., 10-mm-thick disks, were irradiated at a 100-Hz pulse repetition rate. The laser spot was a rectangle with dimensions of $\sim 5 \times 8$ mm. The laser-induced density of point

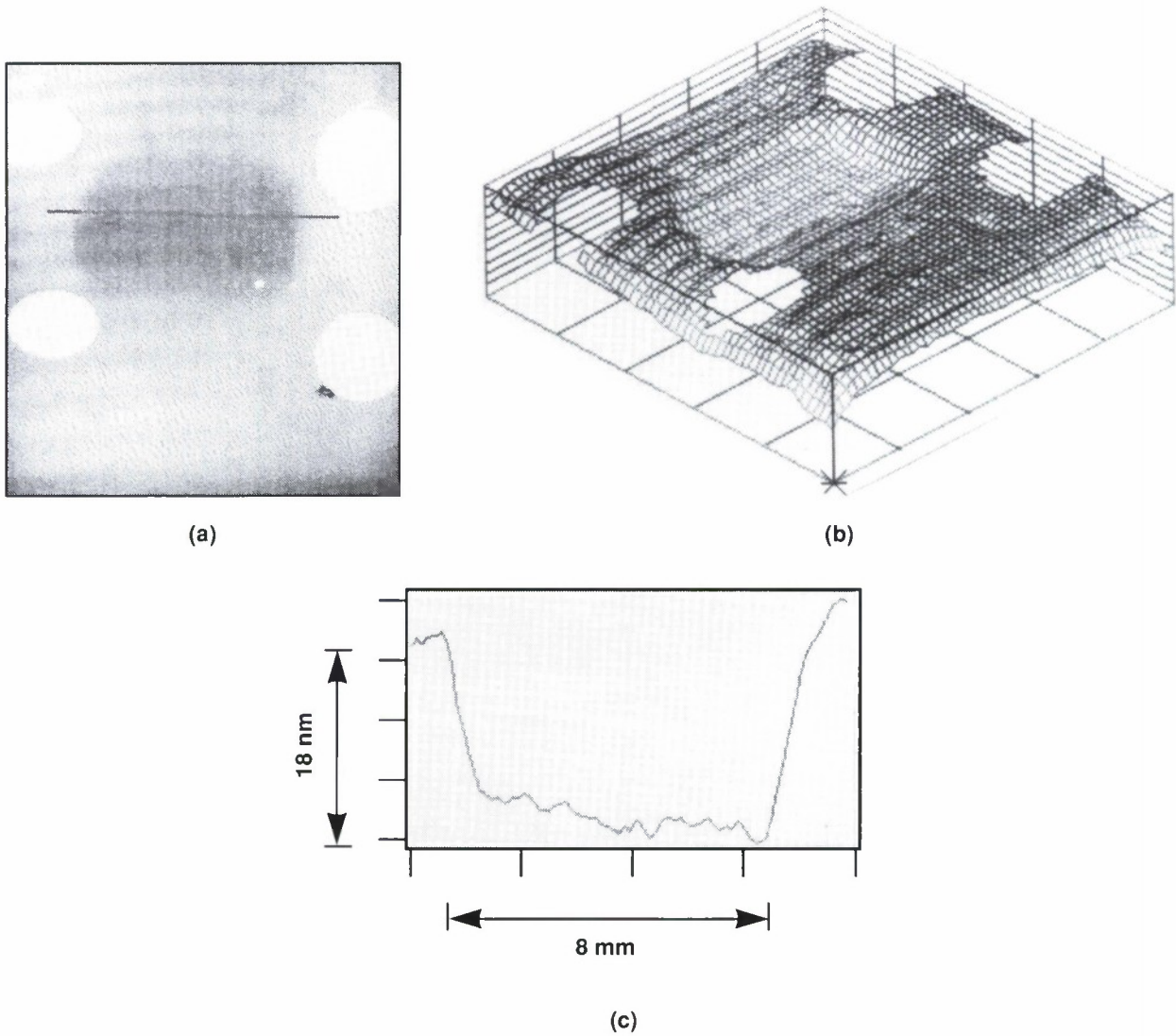


Figure 4-6. PMI output mapping the transmission of a 193-nm-irradiated sample of fused silica: (a) top and (b) three-dimensional views of the sample and (c) a two-dimensional trace. Compaction in the $\sim 5 \times 8$ -mm laser spot is clearly seen (the four blank circles are absorptive dots drawn on the sample for visual demarcation of the laser spot).

defects was determined from UV transmission measurements of irradiated and unirradiated sections of each sample. The laser-induced compaction was measured with a phase-measuring interferometer (PMI). The PMI was used to measure two separate quantities: changes in surface topography and changes in the optical path of a 633-nm beam transmitted through the sample. The former relates directly to the axial shrinkage of the material, whereas the latter reflects the combined effect of axial shrinkage and increased index of refraction. An example of the PMI output is shown in Figure 4-6. The irradiated area is clearly seen, and a change in optical path of less than 2 ppm (18 nm out of 10 mm) is easily measured.

A linear correlation has been established between the peak UV absorbance and the degree of compaction (determined indirectly from stress birefringence measurements and directly from PMI data) under a wide range of fluences and number of laser pulses. This result indicates that both the compaction and E'-center formation are initiated by the same process. The initiating process is in all likelihood a two-photon absorption, which at 193 nm has an absorption coefficient of $\sim 2 \times 10^{-3}$ cm/MW. Following this absorption, an exciton is formed whose decay may lead to atomic rearrangements that manifest themselves as E' centers and macroscopic compaction. As expected for a two-photon process, the observed defects have a quadratic dependence on laser fluence (below ~ 100 mJ cm $^{-2}$ per pulse). Furthermore, the defect formation is largely additive, i.e., it is linear with respect to the number of pulses. Saturation effects were observed only at very high doses. Under most exposure conditions the UV absorption and the compaction are proportional to the number of pulses and to the square of the fluence, and are therefore proportional to each other.

The relationship between the two effects is, however, complex. For instance, the E' centers can be thermally annealed at $\sim 350^\circ\text{C}$, whereas the compaction is reduced to ~ 20 percent of its initial value only at $\sim 600^\circ\text{C}$. Furthermore, while the E' centers are partially bleached by exposure to low-intensity 193-nm irradiation, the compaction remains unchanged. Also, the constant of proportionality between E' centers and the degree of compaction strongly depends on the growth conditions of the fused silica and on subsequent annealing steps. This point is illustrated in Figure 4-7, where the optical path difference (OPD) between exposed and unexposed samples as measured by the PMI at 633 nm is plotted versus the peak UV absorbance of the respective materials. The nine data points represent a matrix of three growth processes and three annealing conditions used at Heraeus-Amersil, Inc. to grow the materials. Figure 4-7 shows that for a fixed set of 193-nm exposure conditions the density of E' centers can be varied by orders of magnitude, depending on the material processing conditions, whereas the OPD is relatively insensitive to those conditions and is changed by at most a factor of 3.

Radiation-induced formation of point defects, such as color centers, is a well-documented effect in both glassy and crystalline materials. However, compaction is understood to a much lesser degree. In fused silica, compaction can be caused by several external sources, including cooling, application of compressive forces, neutron bombardment, and UV irradiation. In general, the observed change in index of refraction δn is related to the fractional change of volume $\delta V/V$ by the following expression [13]:

$$\delta n = -\frac{(n^2 + 2)(n^2 - 1)}{6n} \left(1 - \frac{\delta R/R}{\delta V/V} \right) \frac{\delta V}{V}, \quad (4.1)$$

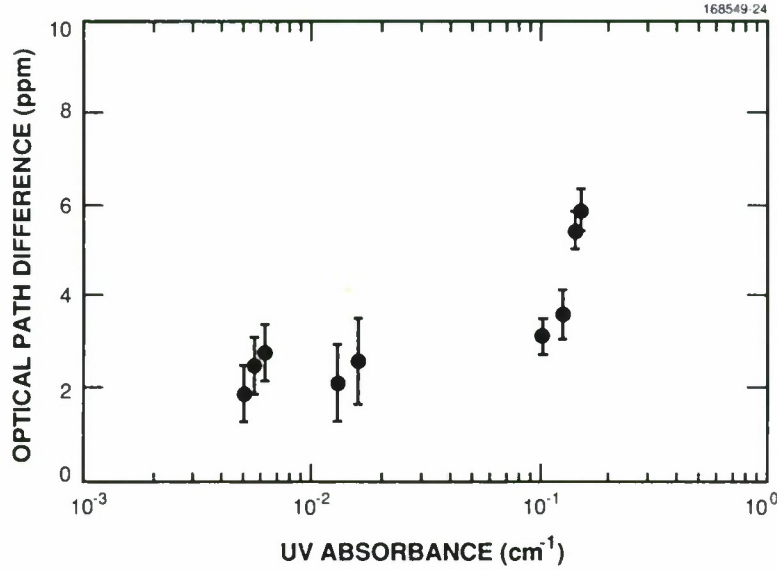


Figure 4-7. Interferometrically measured optical path difference versus ~ 215 -nm absorbance for nine samples of fused silica. All samples were irradiated at 193 nm, 78 mJ cm^{-2} per pulse with 2×10^6 pulses. They differ in growth conditions and post-growth annealing conditions. The material processing can have a significant effect on UV absorbance but much less influence on the compaction as measured with an interferometer.

where n is the refractive index and R is the refractivity, which for fused silica may be interpreted as the ionic volume of oxygen per unit mass of material. At 633 nm,

$$\delta n = -0.53 \left(1 - \frac{\delta R/R}{\delta V/V} \right) \frac{\delta V}{V} . \quad (4.2)$$

The quantity in parentheses represents changes in the relative ionic volume of oxygen during the compaction. It was shown by Primak and Post [13] that its value depends on the cause of compaction; the values are ~ -13 for thermal compaction, ~ 0.6 for elastic compaction, and ~ 0.7 for neutron-induced compaction. Our interferometric measurements of OPD and axial shrinkage of 193-nm-laser-induced compaction indicate that the above quantity is in the range 0.2 to 0.8. Thus, it seems that the oxygen ions, in addition to being brought closer together, are compressed. The details of the atomic rearrangements leading to the compaction are still unclear. One possibility is that radiation-induced bond breaking is followed by changes in the intermediate-range structure of fused silica. Such a structure apparently exists [14] in the form of a network of rings, which consist of SiO_4^{2-} tetrahedra. If thermodynamic or steric reasons drive the redistribution of ring sizes to values other than the pre-irradiation ones, then the amount of microcavities is changed, and this process manifests itself as compaction (or expansion).

M. Rothschild
J.H.C. Sedlacek

REFERENCES

1. G.N. Taylor, L.E. Stillwagon, and T. Venkatesan, *J. Electrochem. Soc.* **131**, 1658 (1984).
2. F. Coopmans and B. Roland, *Proc. SPIE* **633**, 262 (1986).
3. B. Roland, R. Lombaerts, C. Jakus, and F. Coopmans, *Proc. SPIE* **771**, 69 (1987).
4. R-J. Visser, J.P.W. Schellekens, M.E. Reuhman-Huisken, and L.J. van Ijzendoorn, *Proc. SPIE* **771**, 111 (1987).
5. M. Op de Beeck, N. Samarakone, K.H. Baik, L. Van den hove, and D. Ritchie, *Proc. SPIE* **1262**, 139 (1990).
6. J.P.W. Schellekens and R-J. Visser, *Proc. SPIE* **1086**, 220 (1989).
7. J.W. Thackeray, J.F. Bohland, E.K. Pavelchek, G.W. Orsula, A.W. McCullough, S.K. Jones, and S.M. Bobbio, *Proc. SPIE* **1185**, 2 (1990).
8. M.A. Hartney, R.R. Kunz, D.J. Ehrlich, and D.C. Shaver, *Proc. SPIE* **1262**, 119 (1990); Solid State Research Report, Lincoln Laboratory, MIT, 1989:4, p. 55.
9. M.A. Hartney, M. Rothschild, R.R. Kunz, D.J. Ehrlich, and D.C. Shaver, to be published in *J. Vac. Sci. Technol. B* **8**, 1476 (1990).
10. R.A. Ferguson, J.M. Hutchinson, C.A. Spence, A.R. Neureuther, to be published in *J. Vac. Sci. Technol. B* **8**, 1423 (1990).
11. M. Rothschild, D.J. Ehrlich, and D.C. Shaver, *Appl. Phys. Lett.* **55**, 1276 (1989).
12. R.S. Taylor, K.E. Leopold, and R.K. Brimacombe, *Lasers Electro-Optics Society Annual Mtg. Conf. Proc.* (IEEE, New York, 1988), p. 228.
13. W. Primak and D. Post, *J. Appl. Phys.* **30**, 779 (1959).
14. C.S. Mariani and L.W. Hobbs, *J. Non-Cryst. Solids* **119**, 269 (1990).

5. HIGH SPEED ELECTRONICS

5.1 QUASIOPTICAL LOCKING OF A MILLIMETER-WAVE RESONANT-TUNNELING DIODE OSCILLATOR

The oscillation frequency of the double-barrier resonant-tunneling diode (RTD) has recently been extended to 712 GHz [1], which makes it the fastest solid state electronic oscillator demonstrated to date at room temperature. This result was obtained with an RTD made from the InAs/AlSb materials system (InAs quantum well, AlSb barriers). In theory, RTDs made from this system are capable of oscillating in a fundamental mode up to at least 1 THz. A major challenge in operating solid state oscillators at these frequencies is the design of the resonator. Conventional resonators, such as those based on closed cavities or radial transmission lines, exhibit a decreasing unloaded quality factor Q_u with increasing frequency because of increases in the ohmic and scattering losses of metallic surfaces. These factors produce a rapid increase in the frequency-modulated noise linewidth of the oscillator, since this linewidth varies as Q_u^{-2} [2]. At present, the primary application of the RTD oscillator is as a low-noise local oscillator for high-sensitivity radiometers operating in the submillimeter-wavelength region ($f \gtrsim 300$ GHz). In this application the linewidth must be less than about 100 kHz, and the oscillator should be frequency tunable by at least ± 1 percent of the nominal center frequency. We have demonstrated locking of an RTD oscillator to a quasioptical resonator at 103 GHz. This technique provides the required narrow linewidth and tuning range and, in addition, allows easy scaling down for operation at higher frequencies.

The schematic diagram of our quasioptical oscillator designed for the 100-GHz region is shown in Figure 5-1. The RTD is mounted in a standard-height rectangular waveguide in the manner used in all of

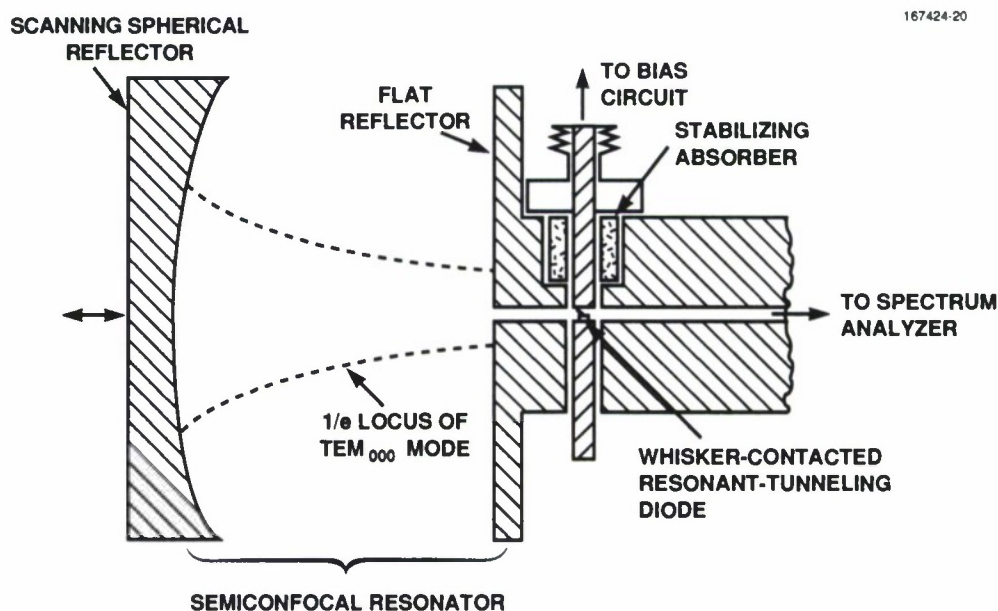


Figure 5-1. Schematic diagram of quasioptical resonant-tunneling diode oscillator designed to operate in the 100-GHz region.

our waveguide RTD oscillators operating above 100 GHz. The diode is dc biased by a coaxial circuit that also suppresses spurious oscillations by placing a very lossy section of transmission line in close proximity to the top wall of the waveguide. The waveguide section terminates abruptly at a flat metallic wall that forms one reflector of a semiconfocal open resonator. The fundamental mode of this resonator is assumed to have a Gaussian transverse intensity profile with a $1/e$ -point locus as shown in Figure 5-1. The spot diameter of this mode at the flat reflector is designed to be about 10 times the height of the rectangular waveguide. This difference, combined with the fact that the radiation pattern from the end of the waveguide is significantly more divergent than the fundamental Gaussian mode, makes coupling between the waveguide and the open cavity fairly weak. Weak coupling is necessary to realize a large Q_u of the open resonator. The output radiation of the oscillator is taken from the opposite end of the waveguide section. The power of the oscillator is measured by a Schottky-diode detector, and the spectrum is resolved by down-converting the oscillator output to the frequency range of a microwave spectrum analyzer.

The experimental power spectrum of the RTD oscillator is shown in Figure 5-2, with and without the benefit of the quasi-optical resonator. The broad spectrum in Figure 5-2(a) results when an absorbing element is inserted into the semiconfocal cavity, fully spoiling the Q_u at 100 GHz. In this case the resonance is a parasitic one formed by the capacitance of the RTD and the inductance of the whisker that contacts the RTD across the waveguide. The width of the spectrum is roughly 10 MHz, which is unsuitable for local oscillator applications. Upon removing the absorber, the spectrum shifts slightly and becomes much narrower. The expansion of this locked spectrum, shown in Figure 5-2(b), yields a linewidth of about 40 kHz. The shift in frequency is a result of the RTD oscillation being locked onto the open-cavity resonance. The narrowing is an indication that locking has occurred and is consistent with the high Q_u of the open resonator compared to that of the parasitic resonance. The center frequency of the cavity resonance is determined, as in all Fabry-Perot-like resonators, by the spatial separation of the reflectors. By varying this separation, we were able to tune the locked power spectrum over a range of ~ 0.3 GHz at a fixed RTD bias voltage. We are presently determining the effect of the open cavity for different RTD bias voltages. For the unlocked oscillator, variation of RTD bias voltage was found to tune the center frequency by ~ 10 GHz.

The power of the cavity-locked oscillation in Figure 5-2(a) (the integral under the power spectrum) was found to be ~ 3 dB less than the unlocked power, which was measured to be $10 \mu\text{W}$. We could obtain significantly more power and maintain the advantage of quasi-optical locking by implementing an array of RTD oscillators rather than the single element demonstrated here. In principle, such an array could consist of a parallel combination of waveguide-mounted RTD structures, such as shown in Figure 5-1. However, a more practical approach for very high frequencies is a planar RTD array based on microstrip circuit techniques. The key point of either approach is for the oscillators to lie in an equiphase plane of the open-cavity mode and thus be synchronized by the high Q_u resonance. This method of power combination has been used to obtain CW power levels up to 20 W from both planar MESFET oscillator arrays [3] and Gunn diode oscillator arrays [4] operating near 10 GHz. It should be a useful technique for obtaining milliwatt levels of power from RTD oscillators in the submillimeter-wave region.

E.R. Brown
C.D. Parker

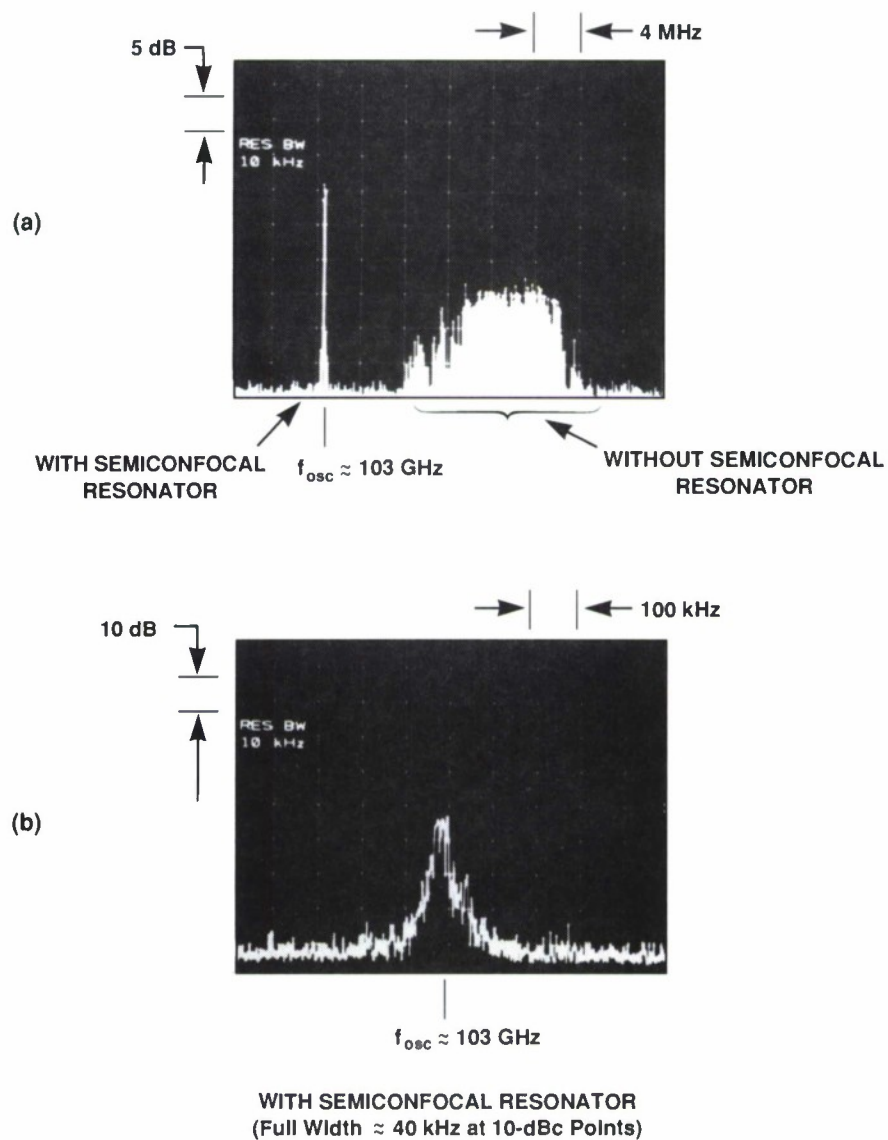


Figure 5-2. (a) Power spectrum of the quasioptical oscillator with and without the semiconfocal open resonator. (b) Horizontal expansion of the power spectrum measured with the semiconfocal open resonator.

REFERENCES

1. E.R. Brown, C.D. Parker, L.J. Mahoney, J.R. Söderström, and T.C. McGill, to be published in *IEEE Trans. Electron Devices*, December 1990.
2. G.D. Vendelin, A.M. Pavio, and U.L. Rohde, *Microwave Circuit Design Using Linear and Nonlinear Techniques* (Wiley, New York, 1990), Sec. 6.7.4.
3. D.B. Rutledge, Z.B. Popovic, R.M. Weikle, M. Kim, K.A. Potter, R.C. Compton, and R.A. York, *1990 IEEE MTT-S Int. Microwave Symp. Dig.* (IEEE, New York, 1990), Vol. 3, p. 1201.
4. R.A. York and R.C. Compton, submitted to *IEEE Trans. Microwave Theory Tech.*

6. MICROELECTRONICS

6.1 REDUCTION OF TRAPPING EFFECTS AT LOW SIGNAL LEVELS IN A BURIED-CHANNEL CCD IMAGER

One of the most serious hazards facing spaced-based charge-coupled device (CCD) imagers operating at low light levels is displacement damage from energetic protons. These particles, which are part of the natural space-radiation environment, have energies ranging upwards of several hundred million electron volts and cannot be stopped by any practical amount of shielding. The principal effect of proton bombardment is displacement damage to the silicon lattice resulting in a variety of crystalline defects that increase the dark current and degrade charge-transfer efficiency (CTE). In a previous report [1], we described measurements that identified the principal defect responsible for CTE degradation as the phosphorus-vacancy (P-V) complex (or center). Here, we describe a simple technique whereby carrier trapping at these defects can be mitigated at low signal levels.

Figure 6-1 illustrates schematically the cross sections of conventional and modified CCD channels and the corresponding potential wells. In a typical channel the charge will occupy most of the available channel width, as shown in Figure 6-1(a). By adding another narrow implant of the buried channel species to the center of the channel, a potential trough can be created. This trough, illustrated in Figure 6-1(b), confines the charge to a smaller volume and thereby reduces the probability of encounters between carriers and trap sites.

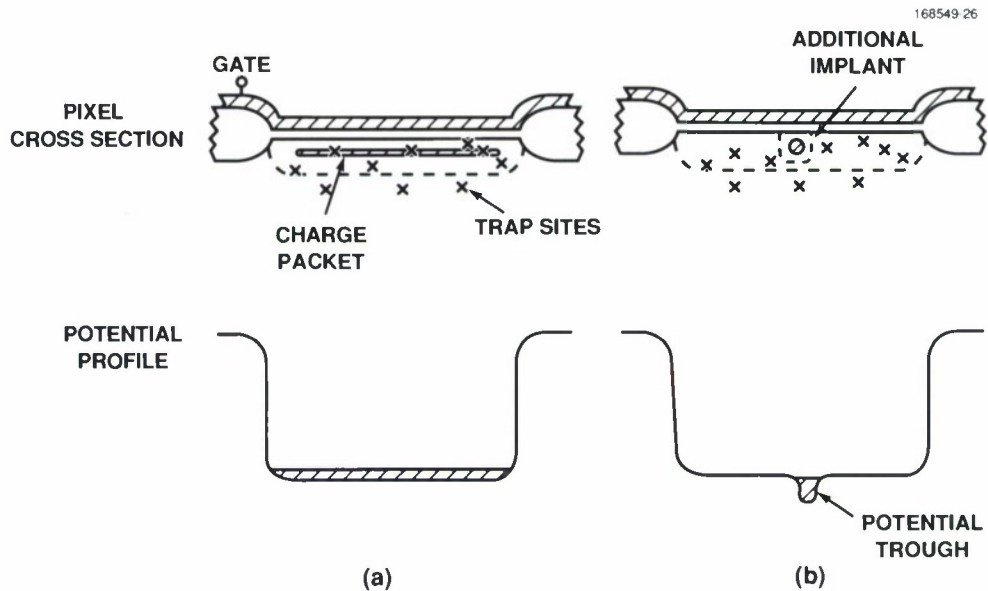


Figure 6-1. Schematic of the cross section of (a) conventional and (b) modified CCD channels and the corresponding potential profiles. Shown in (b) is a concept for reducing trapping effects at low signal levels in a CCD by adding a narrow implant along the channel center to confine the charge packet to a reduced volume.

We have tested this concept on a 420×420 -pixel frame-transfer imager described previously [2],[3]. For this experiment, we designed a photomask for defining the trough implant in which the 420 columns were divided into five groups, each comprising 84 contiguous columns. The first, or control, group had no trough implant, while the remaining groups had drawn trough widths of 5, 4, 3, and 2 μm , respectively. Likewise, the output registers of each die on the wafer had either no trough or a trough having one of the widths used for the columns. The trough implant was phosphorus at an energy of 200 keV and was performed just after the phosphorus buried-channel implant (also 200 keV) but before the deposition of the polysilicon gate layers.

Measurements of the fractional charge loss per transfer, or charge-transfer inefficiency (CTI), were made by irradiating a device with Mn $K\alpha$ x-rays from an Fe^{55} source. Each x-ray photon creates a packet of about 1620 electrons, and the CTI is measured by tracking the amplitudes of such packets as a function of the number of transfers down the columns. Devices were irradiated at the Harvard Cyclotron Laboratory with 40-MeV protons. For the data presented here, the dose was $1.86 \times 10^{10} \text{ cm}^{-2}$ with the imager tilted at an angle of 70° with respect to the beam. The CTI measurements were made at -60°C as the imaging array was being clocked at 417 kHz to transfer the x-ray images into the frame store. The trough potential was about 2.2 V higher than that for the adjacent buried channel.

The CTI data for a device before and after irradiation are shown in Figure 6-2, plotted as a function of the trough width. The total channel width, including trough and non-trough regions, is 21 μm . The pre-irradiation CTI of this device was rather poor (most devices have CTI of less than 10^{-5} without troughs), and

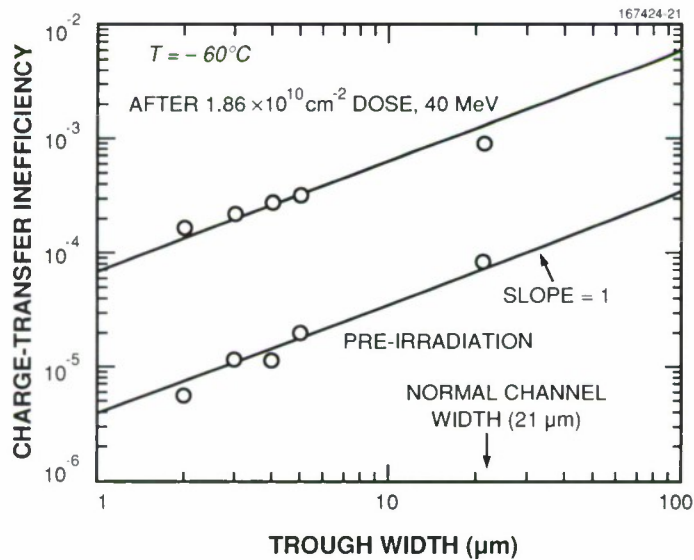


Figure 6-2. Measured data showing the effects of a narrow trough in reducing the charge-transfer inefficiency due to bulk trapping. Measurements were made both before and after bombardment with high-energy protons.

it appears that the epitaxial p/p^+ material on which this device was fabricated had an unusually high bulk trap concentration of unknown origin. Both the pre- and post-irradiation data show that the charge loss scales approximately with the width of the trough, as expected, and that about a tenfold improvement in performance has been achieved by using a $2\text{-}\mu\text{m}$ trough.

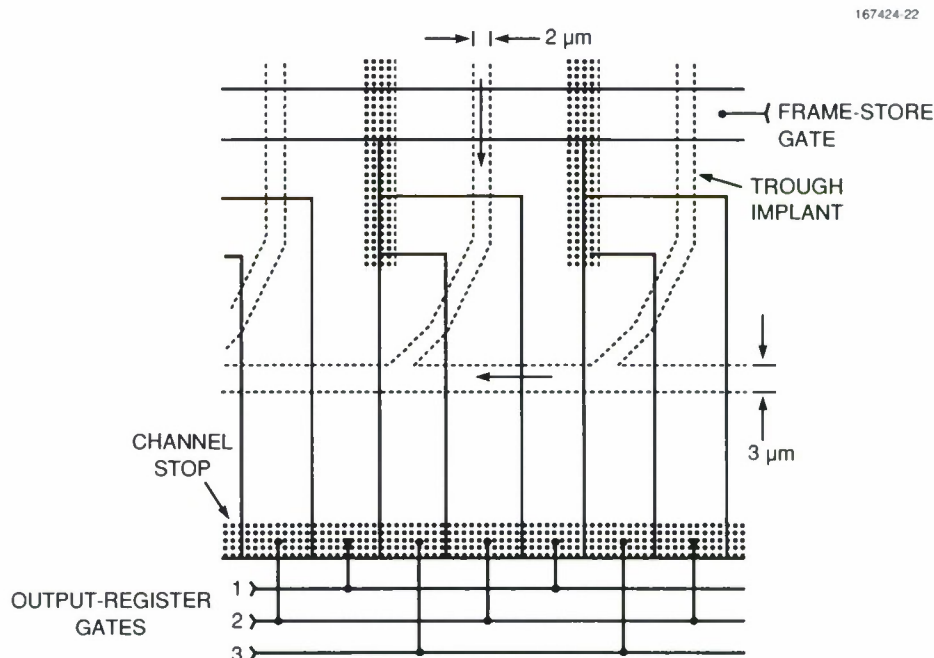


Figure 6-3. Design of the trough implant mask in the region of the CCD where the frame store joins the output register.

One of the difficult design aspects concerns the path of the trough as it merges with a trough in the output register. Such a design should be based on a three-dimensional simulation of the fields at this junction so that the charge flow can be directed for maximum CTE. However, the required simulation tools were not available, and the design used in these experiments was based on an intuitive estimate of the charge flow patterns. This design is shown in Figure 6-3 for the case of a $2\text{-}\mu\text{m}$ trough from the frame store joining a $3\text{-}\mu\text{m}$ trough in the output register. We found that this design worked satisfactorily for all output-register trough widths, although in some cases a $2\text{-}\mu\text{m}$ trough gave very poor CTE. The reasons for this are not known at present.

B.E. Burke
J.A. Gregory
M.J. Cooper

6.2 QUANTUM-EFFICIENCY MODEL FOR A BACK-ILLUMINATED CCD IMAGER

An analytical model has been developed for predicting the spectral response of thinned, p^+ -doped back-illuminated CCD imagers. The governing equations used for modeling the photogenerated carriers in the CCD p^+/p region are very similar to those used for n^+p junction photodiodes. Here, the internal quantum efficiency η of the back-illuminated CCD imager is calculated as a function of the depth X_a of the abrupt p^+ surface layer and the surface recombination velocity S_n of this layer, and these calculations are compared to the experimental results.

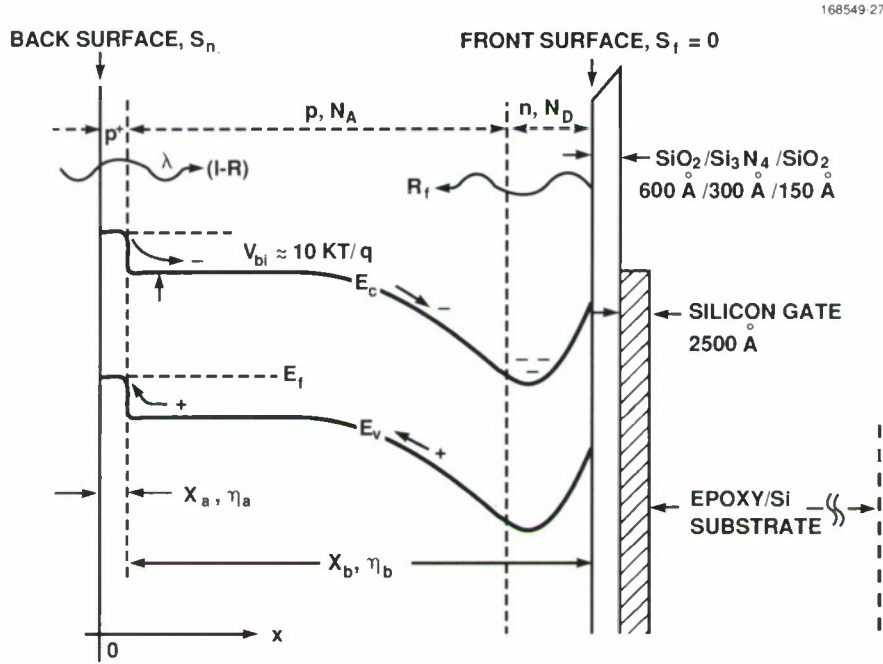


Figure 6-4. Cross-sectional diagram of the band structure of a back-illuminated CCD imager.

Figure 6-4 is a schematic cross section of the back-illuminated CCD imager, showing various parameters included in the model. The p^+ layer, formed by low-energy ion implantation and activated by laser-induced liquid-phase recrystallization, is approximated by the distribution shown in Figure 6-5. This p^+ layer is used not only to shield the p region from external electric fields and surface charges but also to provide a built-in potential V_{bi} at the p^+/p interface to prevent thermalized electrons from reaching the surface. For the quantum efficiency calculations, the CCD is divided into the doped region (0 to X_a) and the bulk region (X_a to X_b). The total internal quantum efficiency η_t is

$$\eta_t = \eta_a + \eta_b, \quad (6.1)$$

where η_a and η_b correspond to the internal quantum efficiency of the doped surface and bulk regions, respectively.

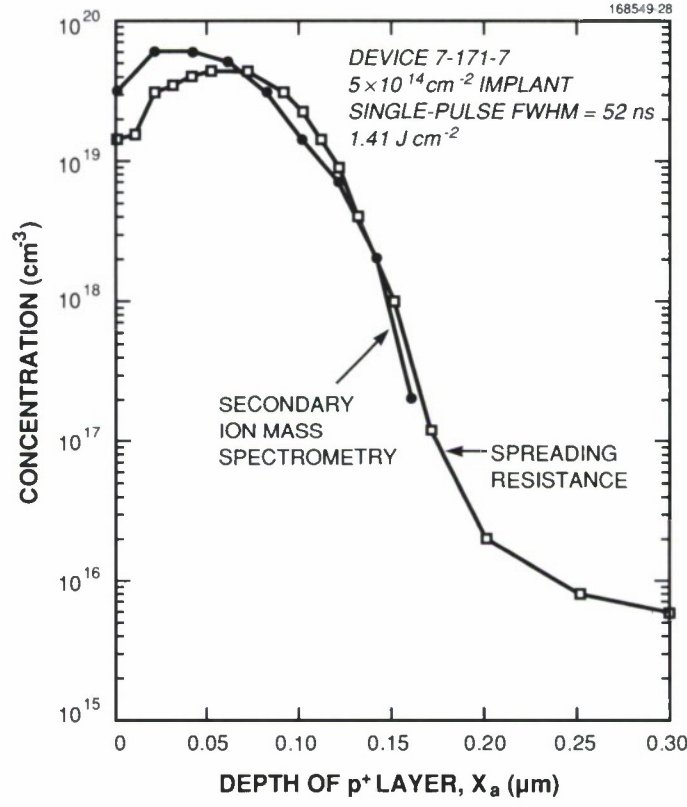


Figure 6-5. Measurements of representative doping profile of p^+ surface layer.

The generation rate of electron-hole pairs by monochromatic light of wavelength λ incident on the back surface and at a distance x from this surface is given by the expression

$$G(\lambda, x) = \alpha(\lambda)F(\lambda)[1 - R(\lambda)]\exp[-\alpha(\lambda)x] , \quad (6.2)$$

where $\alpha(\lambda)$ is the wavelength-dependent absorption coefficient, $F(\lambda)$ is the incident photon flux per unit area per unit wavelength, and $R(\lambda)$ is the reflectance of light at the illuminated surface [4].

Under low-injection conditions, the one-dimensional steady-state continuity equation for electrons in a uniformly doped p region with no external field is

$$D_n \frac{d^2 n_p}{dx^2} + \alpha F(1 - R)\exp(-\alpha x) - \frac{n_p - n_{p0}}{\tau_n} = 0 , \quad (6.3)$$

where D_n is the diffusion coefficient of the electrons, n_p and n_{p0} are the electron concentrations at steady-state and thermal equilibrium conditions, respectively, and τ_n is the lifetime of the electrons.

The general solution to this equation is

$$n_p - n_{po} = A \cosh(x/L_n) + B \sinh(x/L_n) - \frac{\alpha F(1-R)\tau_n}{\alpha^2 L_n^2 - 1} \exp(-\alpha x) , \quad (6.4)$$

where $L_n = (D_n \tau_n)^{1/2}$ is the diffusion length of electrons in p -type silicon.

At the surface, electrons are lost through recombination characterized by a recombination velocity S_n and expressed as

$$S_n(n_p - n_{po}) = D_n d(n_p - n_{po})/dx \quad \text{at } x = 0 . \quad (6.5)$$

At the p^+/p boundary, the built-in field sweeps away almost all the excess carriers:

$$n_p - n_{po} \approx 0 \quad \text{at } x = X_a. \quad (6.6)$$

Using these boundary conditions, we can calculate the electron density and its electron photocurrent density resulting from carriers generated in the p^+ layer. Since the diffusion length of the minority carriers in the p region is much greater than X_b , it can be assumed that all the photoelectrons generated in the p^+ layer that reach X_a are collected by the CCD. Thus, the internal quantum efficiency of the p^+ surface layer is the electron particle photocurrent $J_n/(-q)$ at X_a divided by the total number of photoelectrons generated per second per unit area, $F(1-R)$, which is expressed as

$$\eta_a = \frac{J_n/(-q)}{qF(1-R)} = \frac{-D_n (dn_p/dx)_{X_a}}{F(1-R)} = \frac{\alpha L_n}{\alpha^2 L_n^2 - 1} \times \left[\frac{\left(\frac{S_n L_n}{D_n} + \alpha L_n \right) - e^{-\alpha X_a} \left(\frac{S_n L_n}{D_n} \cosh \frac{X_a}{L_n} + \sinh \frac{X_a}{L_n} \right)}{\left(\frac{S_n L_n}{D_n} \right) \sinh \left(\frac{X_a}{L_n} \right) + \cosh \left(\frac{X_a}{L_n} \right)} - \alpha L_n e^{-\alpha X_a} \right] , \quad (6.7)$$

where L_n is the diffusion length in the p^+ layer. The built-in potential of the p^+/p interface and the long diffusion length in the bulk ensures that all charge generated in the p region is collected by the CCD. Thus, the internal quantum efficiency in this region, η_b , is simply equal to the total normalized flux absorbed in the region [5],

$$\eta_b \approx e^{-\alpha X_a} \left[1 - (1 - R_f) e^{-\alpha X_b} \right] , \quad (6.8)$$

where R_f is the effective reflectance at the front (unilluminated) surface of the silicon due to the multiple reflections of the front dielectrics (all this reflected light is assumed to be absorbed in this region during its second pass).

Table 6-1 summarizes the important parameters used to calculate the total internal quantum efficiency η_i . Since the published values of α and the index of refraction of silicon with respect to λ differ significantly between various sources [6],[7], η_i has been calculated as a function of absorption coefficient for comparison.

TABLE 6-1
Parameters Used To Calculate Total Internal Quantum Efficiency

Parameter	Symbol	Value
Diffusion Coefficient in p^+ Layer	D_n	4.5 cm ² /s
Diffusion length in p^+ Layer	L_n	24 μm
Depth of Si	X_a	0.01 to 0.40 μm
Absorption Coefficient in p^+ Layer	α	10 ¹ to 10 ^{6.4} cm ⁻¹
Surface Recombination Velocity in p^+ Layer	S_n	10 ³ to 10 ⁷ cm s ⁻¹
Doping Level in p^+ Layer		10 ¹⁹ cm ⁻³
Thickness of the Bulk	X_b	10 μm
Diffusion Length in the Bulk		$\gg X_b$
Bulk Diffusion Coefficient		14.5 cm ² s ⁻¹
Front Surface Reflectance	R_f	0.55

Figure 6-6 shows η_i versus α for 0.1- μm -thick p^+ layers and for $S_n = 1 \times 10^7$, 1×10^6 , and 2×10^5 cm s⁻¹. The $\alpha(\lambda)$ and reflectance are taken from Rajkanan et al. [7], and the best match between calculation and experiment is with a surface recombination velocity of $\sim 1 \times 10^6$ and 2×10^5 cm s⁻¹ for data from devices 7-171-7 and 7-171-8, respectively. Figure 6-7 shows a contour plot of calculated η_i versus S_n and X_a at the wavelength of highest absorption coefficient ($\alpha \approx 2.35 \times 10^6$ cm⁻¹ at $\lambda \approx 0.028$ μm). For practical values of the independent variables ($X_a > 0.01$ μm , $S_n > 10^4$), η_i depends more strongly on S_n than on X_a , suggesting that reduction and control of S_n is a primary strategy in improving UV response.

C.M. Huang	J.A. Gregory
J.R. Theriault	B.E. Burke
E.T. Hurley	B.W. Johnson

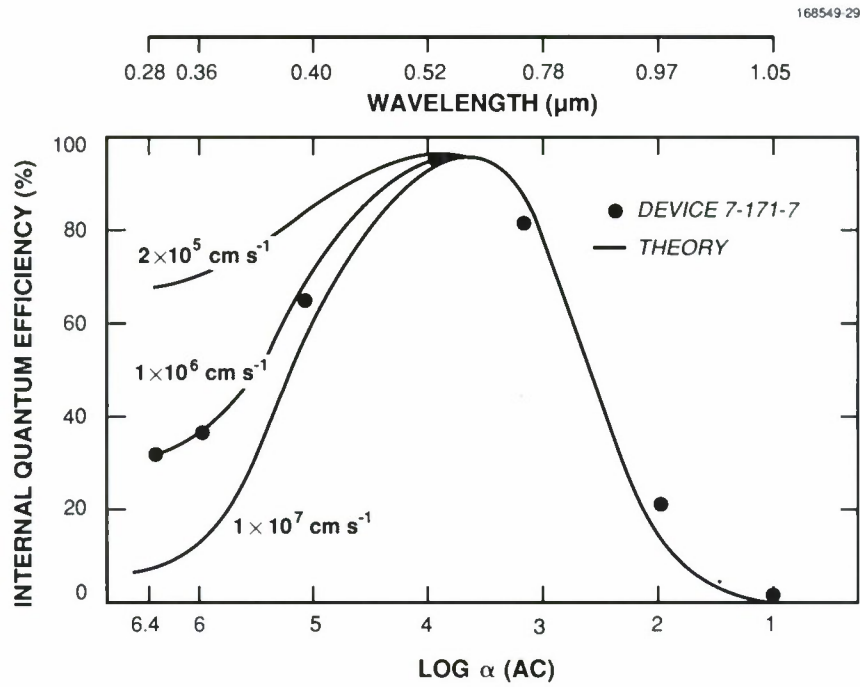


Figure 6-6. Comparison of calculated and measured QE for two different devices, using S_n as a fitting parameter and $X_a \approx 0.1 \text{ mm}$.

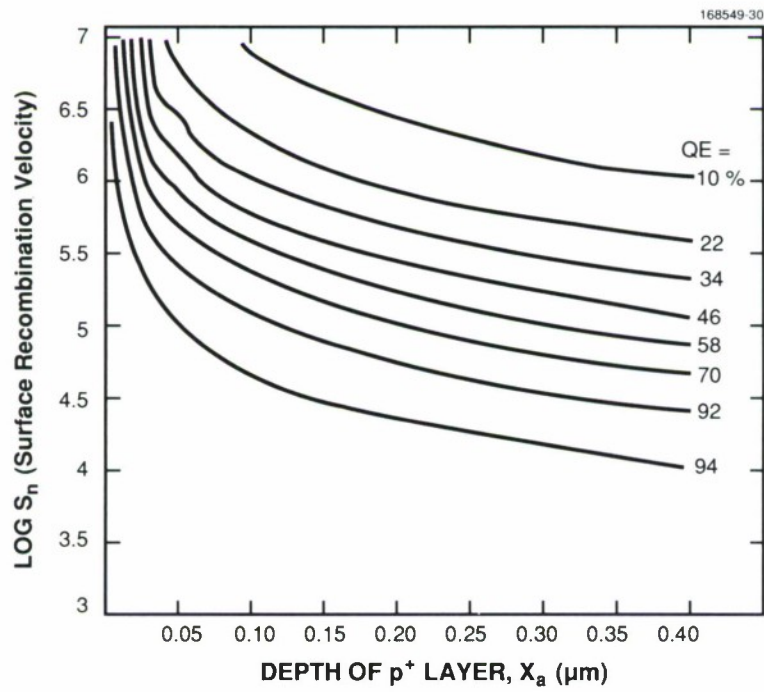


Figure 6-7. Plot of calculated QE versus S_n and X_a .

REFERENCES

1. Solid State Research Report, Lincoln Laboratory, MIT, 1990:2, p. 51.
2. Solid State Research Report, Lincoln Laboratory, MIT, 1988:3, p. 61.
3. B.E. Burke, R.W. Mountain, D.H. Harrison, G.R. Ricker, M.W. Bautz, J.P. Doty, J.H. Reinold, and C.L. Doherty, *Int. Solid-State Circuits Conf. Tech. Dig.* (IEEE, New York, 1989), p. 94.
4. S.M. Sze, *Physics of Semiconductor Devices*, 2nd ed. (Wiley-Interscience, New York, 1981), p. 800.
5. J.R. Janesick, *1986 Int. Electron Devices Mtg. Tech. Dig.* (IEEE, New York, 1986), p. 350.
6. G.E. Jellison, Jr. and F.A. Modine, *J. Appl. Phys.* **53**, 3745 (1982).
7. K. Rajkanan, R. Singh, and J. Shewchun, *Solid-State Electron.* **22**, 793 (1979).

7. ANALOG DEVICE TECHNOLOGY

7.1 SURFACE IMPEDANCE MEASUREMENTS OF $\text{YBa}_2\text{Cu}_3\text{O}_{7-x}$ THIN FILMS IN STRIPLINE RESONATORS

Planar transmission line resonators and especially stripline resonators overcome some of the limitations of cavity resonators [1], since the surface resistance R_s can easily be measured as a function of frequency, temperature, and RF power. Until recently, however, interpretations of stripline measurements were complicated by the nonuniform distribution of currents in the conductors and by the large values of penetration depth of films of the high- T_c materials, which in many cases are comparable to the film thickness. Detailed calculations of the current distributions for several film thicknesses and penetration depths for the stripline geometry used in these measurements have recently been completed using full electromagnetic wave methods [2]. With knowledge of the current distribution, we can calculate accurately the inductance L of the stripline as a function of penetration depth λ . Then, by measuring the resonant frequency (proportional to $1/\sqrt{L}$) as a function of temperature, we can measure λ .

We have characterized three resonators, each fabricated from a set of three sputtered $\text{YBa}_2\text{Cu}_3\text{O}_{7-x}$ films. Sample 1, reported earlier [1], was deposited at a substrate temperature of 680°C. Sample 2 was deposited at 720°C under conditions that produced lower electron and negative-ion bombardment of the sample. Sample 3 was deposited at a substrate temperature of 760°C from a target with higher purity than that used for samples 1 and 2. These films have a resistive transition between 79 and 87 K and are 300 nm thick. The films are granular, and the grains are highly aligned with the c -axis perpendicular to the substrate.

Figure 7-1 shows the measured resonant frequency of the stripline versus temperature using sputtered film 3. The solid line is a least-squares fit to the data using the temperature dependence of λ calculated from the two-fluid model,

$$\lambda(T) = \frac{\lambda(0)}{\sqrt{1 - \left(\frac{T}{T_c}\right)^4}}, \quad (7.1)$$

and the scaling of the resonant frequency f with inductance,

$$f(T) = f_0(T_0) \sqrt{\frac{L(\lambda(T_0))}{L(\lambda(T))}}, \quad (7.2)$$

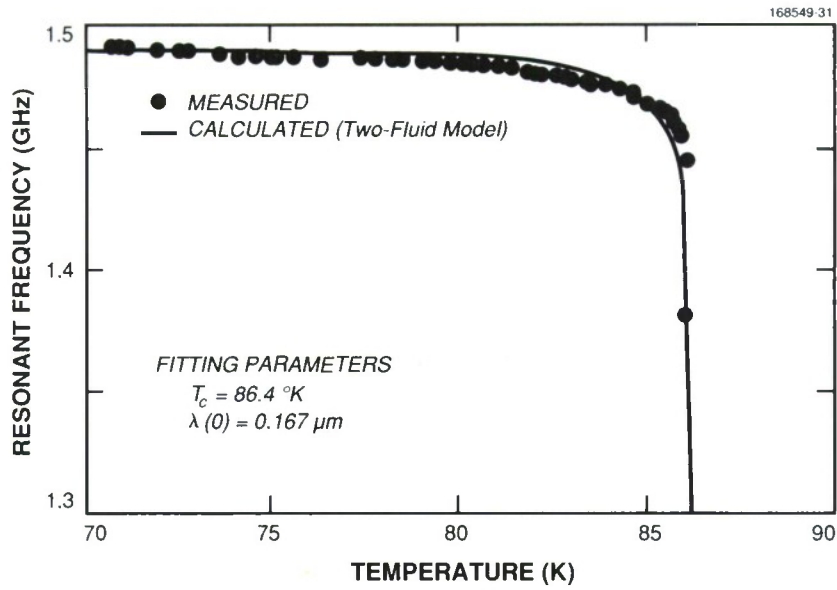


Figure 7-1. Measured and calculated values of resonant frequency of the fundamental mode of the resonator versus temperature for sputtered film 3. The calculated values use the two-fluid model. The best fit is obtained with $T_c = 86.4 \text{ K}$ and $\lambda(0) = 0.167 \text{ } \mu\text{m}$.

where $L(\lambda)$ is derived from the calculated values [2] and T_0 is an arbitrary reference temperature. The best fit, seen in Figure 7-1, is obtained with $T_c = 86.4 \text{ K}$ (which is consistent with the measured resistive transition) and $\lambda(0) = 0.167 \text{ } \mu\text{m}$. The experimental points show some deviation from the two-fluid model, as has been observed by others [3].

TABLE 7-1
Measured Penetration Depth for Sputtered Films

Sample	$\lambda(0) \text{ (}\mu\text{m)}$	$T_c \text{ (K)}$
Sputtered $\text{YBa}_2\text{Cu}_3\text{O}_{7-x}$		
1	0.316	80
2	0.336	80
3	0.167	86.4
Sputtered Nb	0.070	9.2

Table 7-1 summarizes the measured penetration depth for the three sputtered $\text{YBa}_2\text{Cu}_3\text{O}_{7-x}$ films. Included in the table is a measurement of a sputtered niobium film, which serves as a calibration of the method. The values of λ must be understood as an effective penetration depth influenced by field penetration near the grain boundaries. The penetration depth of the grains themselves may be smaller. The larger penetration depth of films 1 and 2 can be explained by the greater influence of grain boundaries in these films than in film 3, which was deposited at higher temperature.

With knowledge of the current distribution, we are able to calculate the peak values of magnetic field for a given position on the stripline. Figure 7-2 shows the dependence of surface resistance R_s on peak RF magnetic field $H_{\text{rf,max}}$ for the three sputtered films and for a postannealed film reported earlier [1]. All were measured at 4 K and at the frequency indicated in the figure caption. The value of $H_{\text{rf,max}}$ can be calculated from the current distribution. For sputtered film 2, $H_{\text{rf,max}}$ is 150 Oe at the point where R_s increases rapidly, and for film 3 it is 225 Oe.

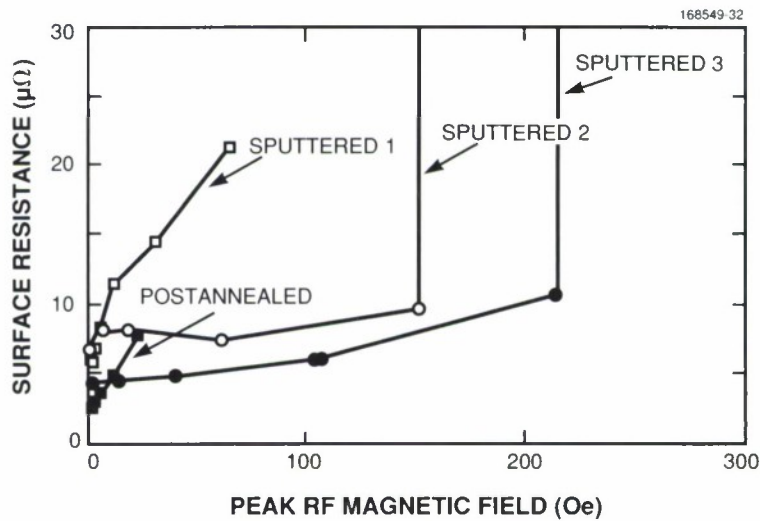


Figure 7-2. Surface resistance versus peak RF magnetic field for four different films as indicated. Lines have been drawn to connect the points. For sputtered films 2 and 3, $f = 1.5$ GHz. For sputtered film 1 and the postannealed film, $f = 1.6$ GHz. All measurements were made at 4.2 K.

The films sputtered at higher temperature (2 and 3) clearly show a greatly reduced dependence of R_s on current and H_{rf} . For both of these films the input power was increased until a sharp increase in R_s was measured, indicating that the critical current or magnetic field was reached. The results and analysis for the low-sputtering-temperature film (1) and the postannealed film have been presented in detail previously [1]. The results showing a linear dependence of R_s on resonator current are explained by flux penetration at the grain boundaries. The lower dependence of R_s on H_{rf} in the newer films is a consequence of lowered contributions from the grain boundaries.

We have demonstrated that the RF properties R_s and λ are better in films produced by single-target sputtering at substrate temperatures of 750°C than in films sputtered at lower temperatures. In previous work [1] we showed that R_s is strongly affected by grain boundaries and intergranular material in postannealed films and films sputtered at lower temperatures. This is because of the linear dependence of R_s on H_{rf} beginning at very low fields, indicating that the flux penetration is occurring at the grain boundaries. The conclusion of strong influence from the weak links at the grain boundaries is strengthened by the measurements of λ reported here. It has been proposed [4] that intergranular weak links increase the effective λ . We conclude that there should be some correlation between larger λ and strong dependence of R_s on H_{rf} , although λ is not the only determinant of R_s . We note that sputtered films 1 and 2 have similar λ , while 2 and 3 have similar $R_s(H_{rf})$. This is not completely understood.

D.E. Oates

A.C. Anderson

7.2 HIGH-TEMPERATURE SUPERCONDUCTIVE CHIRP FILTER

The recently discovered high-temperature superconductors (HTSs) offer great potential for low-loss passive microwave applications, such as long tapped delay line structures for signal processing [5]. Much progress continues to be made in reducing the surface resistance of HTS materials, in particular $\text{YBa}_2\text{Cu}_3\text{O}_{7-x}$. The values of surface resistance at 4 GHz in state-of-the-art films are consistently better than in copper by at least a factor of 10 at 77 K and a factor of 100 at 4.2 K [6]. Design and fabrication efforts have been undertaken to develop HTS chirp-response tapped delay line filters. Because long lines with delay on the order of 10 ns or greater are needed to implement these filters, uniform deposition of HTS thin films on substrates of 2-in. diameter or larger is required.

Currently, only one growth technique is available for the deposition of uniform $\text{YBa}_2\text{Cu}_3\text{O}_{7-x}$ thin films on a 2-in.-diam. substrate. This technique is an ex situ process in which amorphous $\text{YBa}_2\text{Cu}_3\text{O}_{7-x}$ is deposited on a substrate by coevaporation of BaF_2 , Y, and Cu, followed by postdeposition annealing, typically at 850°C, in flowing O_2 containing H_2O vapor [7]. Uniformity is crucial in obtaining low values of surface resistance along the entire length of a patterned delay line. Delay lines with 10 to 20 ns of delay are of the order of 1 m in length. The postannealing process is capable of producing $\text{YBa}_2\text{Cu}_3\text{O}_{7-x}$ films with a transition temperature of 91 ± 0.1 K over an entire 2-in.-diam. LaAlO_3 substrate [8]. The postannealing process can eventually be used to produce films on both sides of a substrate by depositing amorphous $\text{YBa}_2\text{Cu}_3\text{O}_{7-x}$ on each side and then annealing both sides simultaneously. Other techniques for $\text{YBa}_2\text{Cu}_3\text{O}_{7-x}$ film deposition on large-area substrates are under development, such as an in situ growth process using off-axis single-target sputtering [9].

A disadvantage of any postannealing process is that defects and impurities tend to aggregate rather than spread uniformly through the film as in an in situ process [10]. This may result in more weak-link behavior for the postannealed films in addition to more sensitivity to processing steps and environmental conditions. Furthermore, the postannealing process is incapable of growing fully *c*-axis-oriented films of $\text{YBa}_2\text{Cu}_3\text{O}_{7-x}$ at film thicknesses greater than 300 nm. Multilayer HTS film deposition is also precluded for the postannealing process. Thus, an optimized in situ growth process should ultimately provide the best $\text{YBa}_2\text{Cu}_3\text{O}_{7-x}$ thin films.

The design and fabrication of chirp filters made of niobium on silicon have been optimized previously, so very good agreement between design and measured performance has been obtained [11]. However, HTS materials issues require a complete reevaluation of the tapped delay line design. Various transmission line geometries were considered for the HTS chirp filter implementation [12],[13], and stripline was chosen for the first demonstration. The narrow linewidths ($\sim 50 \mu\text{m}$) required for 50- Ω lines in a stripline using LaAlO_3 substrates present a fabrication problem in HTS materials because of defects not only present in the as-deposited HTS film but also introduced during patterning of the delay line. Although 40- μm -wide striplines using niobium on LaAlO_3 could be fabricated easily in lengths exceeding 2 m, these designs could not be successfully transferred to $\text{YBa}_2\text{Cu}_3\text{O}_{7-x}$.

Fabrication of 50- Ω microstrip delay lines 160 μm in width, however, has been successful in $\text{YBa}_2\text{Cu}_3\text{O}_{7-x}$. This design consists of one 7-ns and one 1.5-ns delay line. These lines fabricated in $\text{YBa}_2\text{Cu}_3\text{O}_{7-x}$ are used along with a GaAs track-and-hold circuit to simulate a pretrigger function (both the delay line and the track-and-hold circuit operate at 77 K) [12]. The success of the design has led to the stripline chirp filter shown in Figure 7-3. The design uses 40- Ω , 120- μm -wide signal lines in the tapped portion of the device. A Klopfenstein-taper impedance transformer makes the transition from narrow 50- Ω , 50- μm -wide input/output lines to the much wider 40- Ω lines. This greatly reduces the length of narrow line required and results in a successful demonstration with $\text{YBa}_2\text{Cu}_3\text{O}_{7-x}$. The bandwidth of this chirp

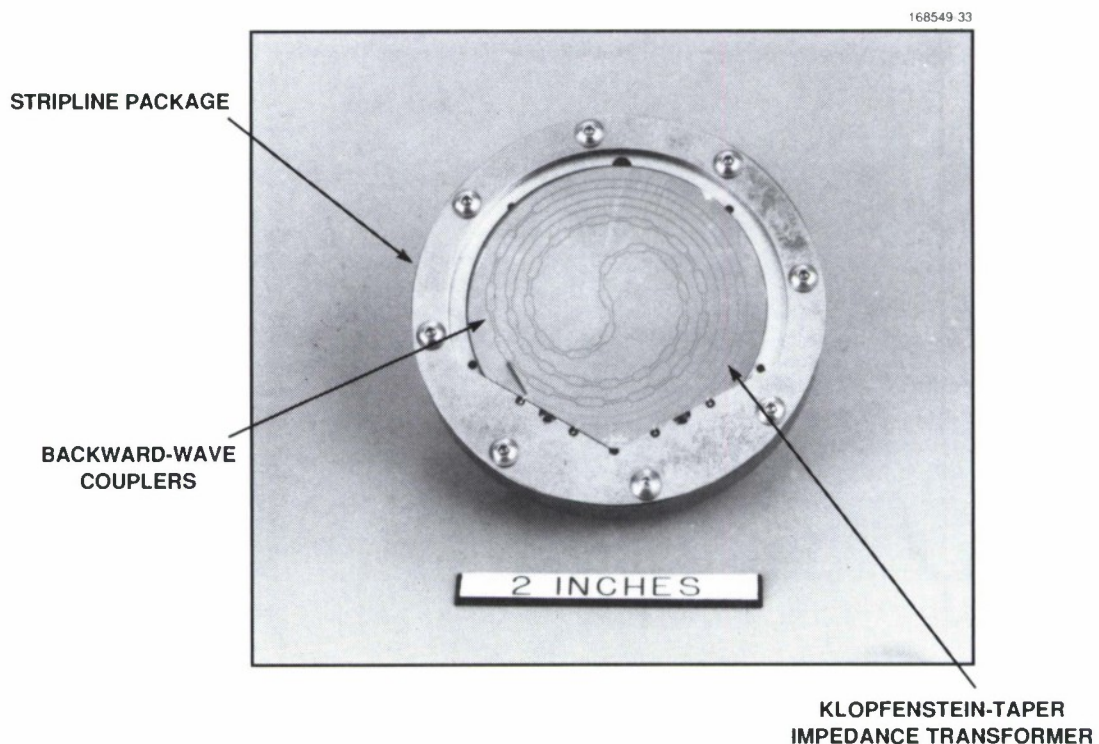


Figure 7-3. Photograph of a superconductive stripline chirp filter. The filters were fabricated on 2-in.-diam. LaAlO_3 substrates using either $\text{YBa}_2\text{Cu}_3\text{O}_{7-x}$ signal lines and silver ground planes or niobium signal lines and niobium ground planes.

filter is 2.6 GHz centered on 4 GHz, and the length of dispersive delay is 8 ns. The filter is flat weighted so that the response is constant across the frequency bandwidth.

The HTS delay line processing begins with formation of 300 nm of $\text{YBa}_2\text{Cu}_3\text{O}_{7-x}$ on a 2-in.-diam., 500- μm -thick LaAlO_3 substrate using a coevaporation and postdeposition annealing process. Patterning of the $\text{YBa}_2\text{Cu}_3\text{O}_{7-x}$ signal line is accomplished with standard AZ photoresist and a spray etch of 0.25 percent H_2PO_4 . This spray etch has been found to be successful in preventing the residual film formation typically seen with other wet etching techniques. Undercutting of 1 to 2 μm is observed with this etch, but this is not significant since the linewidth of the tapped portion of the filter is 120 μm . A trilayer resist (PMMA/Ti/AZ1470) and liftoff process are used to pattern 1.5- μm -thick silver contacts on the signal line. Low-resistance ohmic contacts to the signal line are produced by annealing the structure at 400°C in flowing O_2 . Final packaging is performed using ultrasonic wedge bonding of aluminum ribbon directly to the annealed silver ohmic contacts on the signal line to form highly reliable contacts. A 4- μm -thick, e-beam-evaporated silver film is used for the ground plane. Figure 7-3 shows a photograph of the final packaged filter. In addition, an all-niobium version of the chirp filter has been fabricated to verify device performance. For the all-niobium filter, niobium is deposited by sputtering and the signal line is patterned by reactive plasma etching.

The designed and measured downchirp transmission responses of the chirp filter as a function of frequency are shown in Figure 7-4. The designed response is calculated assuming lossless transmission lines.

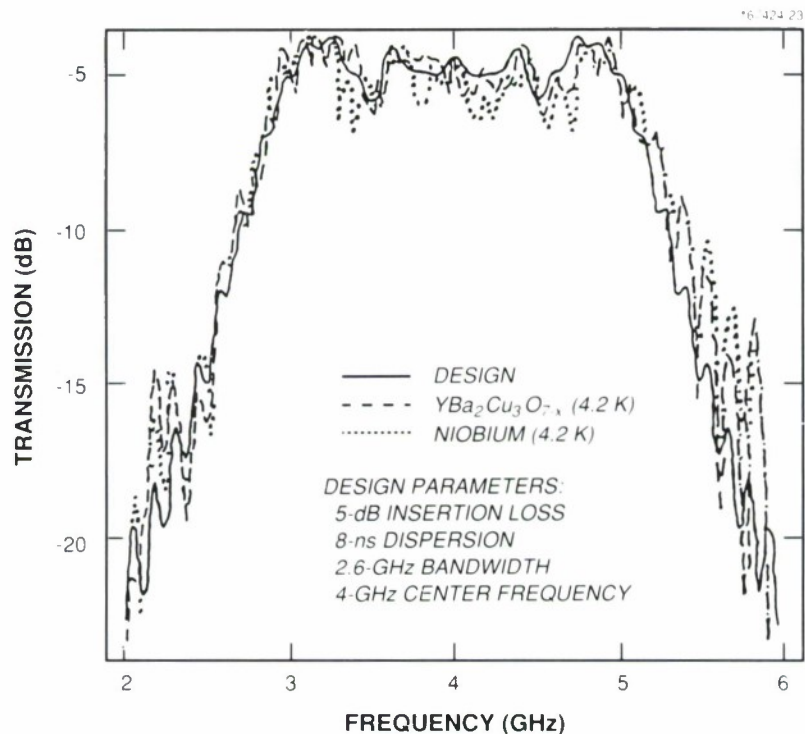


Figure 7-4. Comparison of the designed and measured transmission response of the superconductive chirp filter. The designed response was calculated assuming lossless transmission lines. The measured transmission response at 4.2°K is shown for both $\text{YBa}_2\text{Cu}_3\text{O}_{7-x}$ and niobium versions of the filter.

For comparison, the measured transmission responses of both the all-niobium version of the chirp filter on LaAlO_3 and the $\text{YBa}_2\text{Cu}_3\text{O}_{7-x}$ version with silver ground planes are measured at 4.2 K. The agreement between design and actual performance is striking considering the relatively small number of couplers used in this design. Figures 7-5(a) and 7-5(b) show the $\text{YBa}_2\text{Cu}_3\text{O}_{7-x}$ filter downchirp and upchirp response, respectively, to a 250-mV step input. The response of each of the 32 couplers is clearly visible. Because the filter is flat weighted, the taps are more strongly coupled at the lower frequencies, resulting in a larger output at the end of the response as seen in Figure 7-5(a). In Figure 7-5(b), the flat-weighted nature of the designed filter response again results in a stronger response from the low-frequency couplers.

In summary, a superconductive $\text{YBa}_2\text{Cu}_3\text{O}_{7-x}$ stripline chirp filter has been demonstrated on a 2-in.-diam. LaAlO_3 substrate. The chirp filter design includes a Klopfenstein-taper impedance transformer so that the dispersive, i.e., the tapped-delay-line, portion of the filter can be implemented with 40- Ω , 120- μm -wide lines, while 50- Ω , 50- μm -wide lines are used for each of the input/output lines. The chirp filter has a 2.6-GHz

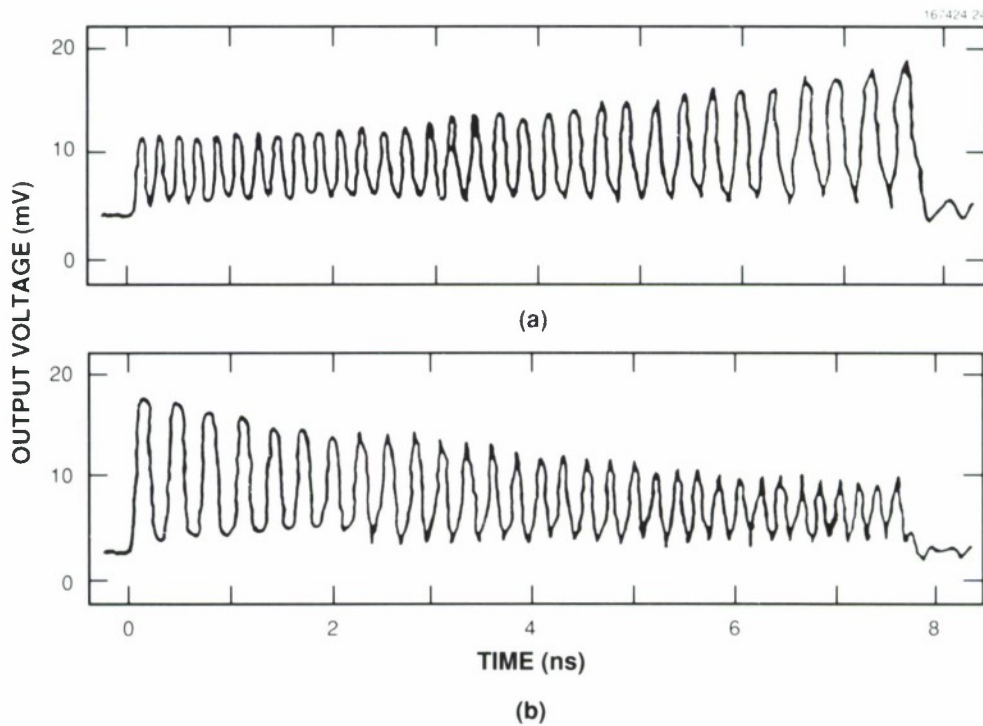


Figure 7-5. (a) Downchirp response and (b) upchirp response to a 250-mV step input measured at 4.2 K for the $\text{YBa}_2\text{Cu}_3\text{O}_{7-x}$ filter.

bandwidth, a 4-GHz center frequency, 12 ns of total delay (including impedance transformers), and 8 ns of dispersive delay, giving a time-bandwidth product of 21. These results have demonstrated that complex tapped delay line devices can be designed and implemented using HTS materials and compatible substrates.

W.G. Lyons	*P.M. Mankicwich
J.M. Hamm	*M.L. O'Malley
R.S. Withers	*R.E. Howard
A.C. Anderson	

7.3 SERIAL-PARALLEL-SERIAL CCD FOR HIGH-SPEED SIGNAL ACQUISITION

An analog memory chip based on a charge-coupled device (CCD) has been designed for high-speed data acquisition and slow readout (fast-in, slow-out mode). While all-digital systems require many components, the CCD memory is compact and consumes very little power (< 50 mW). The chip has a serial-parallel-serial (SPS) architecture, as described in [14]. The memory consists of a high-speed input register, a parallel array, and a low-speed output register, and it can hold 128×128 (16 K) analog samples. A photograph of the chip is shown in Figure 7-6, and a functional schematic is shown in Figure 7-7. All sections of the device are shallow-buried-channel CCDs operating with two-phase 5-V clocks [15]. During the fast-in time, the top register acquires 128 samples of the incoming signal. When the top register is full, its clocks are stopped, and the charge is transferred one stage down the parallel array at a rate that is 1/128th of the input rate. When the parallel array is full, after 128 parallel transfers, the charge is transferred line by line to the bottom serial register and read out at a slower rate, which is usually determined by the circuitry that follows the memory.

The input serial register is similar to the high-speed shallow-buried-channel linear CCDs described in [15]. It consists of a two-phase CCD, $26\text{ }\mu\text{m}$ wide with $4\text{-}\mu\text{m}$ -long barrier gates and $7\text{-}\mu\text{m}$ -long storage gates. As described in [15], the storage gates have step doping to enhance the transfer speed. Since in the SPS the charge transfer occurs in two dimensions, the step implant was tilted 4.4° . With this step-doping geometry, we expected to enhance the drift fields mostly along the serial register, where maximum speed is desired, but also to some degree in the perpendicular direction, where because of the long gate length ($26\text{ }\mu\text{m}$) the fringing fields are very weak for the serial-to-parallel transfer. Figure 7-7 shows the operation of the SPS schematically. The oscilloscope traces show the high-speed input waveform (two negative-going pulses) and the low-speed output. The horizontal and vertical scales were adjusted so that the two traces could be lined up. The sampling rate was 280 MHz. The top of the input waveform was beyond the input range of the CCD, so that the device was operated with zero represented by zero charge in the well, i.e., no fat zero (worst case condition). The bottom of the output pulses track the bottom of the input pulses very well, while the top is flat because it is pinned at the zero-charge level. Beyond 280 MHz, the charge-transfer efficiency in the top register degrades very rapidly.

*Author not at Lincoln Laboratory.

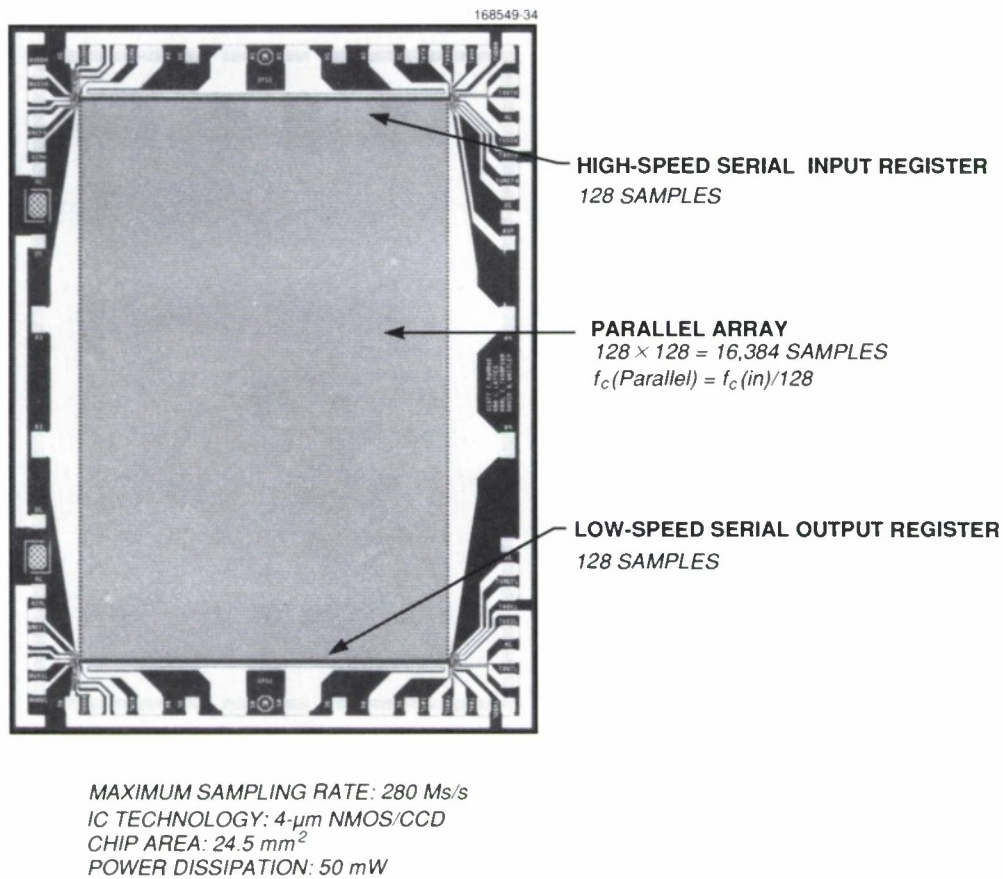


Figure 7-6. Serial-parallel-serial CCD memory.

For comparison, SPS CCDs without the built-in fields were fabricated on the same wafers; the maximum clocking rate in the top registers of the uniformly doped CCDs was only 150 MHz. The serial-to-parallel transfer required at least 125 ns. This is generally consistent with our estimates from two-dimensional simulations [15], and adequate for a serial-to-parallel transfer that is 1/128th of the serial rate. For the parallel transfer rate, there was no measurable difference between the uniform and step-doped CCDs. This result, while disappointing, is understandable, since only a small fraction of the built-in fields are in the serial-to-parallel direction.

We have demonstrated a 16-K monolithic analog memory capable of sampling incoming data at 280 MHz, storing it, and slowing it down so that it can be interfaced with conventional processors. Other CCD-based buffer memories have been demonstrated at hundreds of megahertz, but those speeds are achieved at the expense of memory size and require at least 10-V clocks. The CCDs with built-in drift

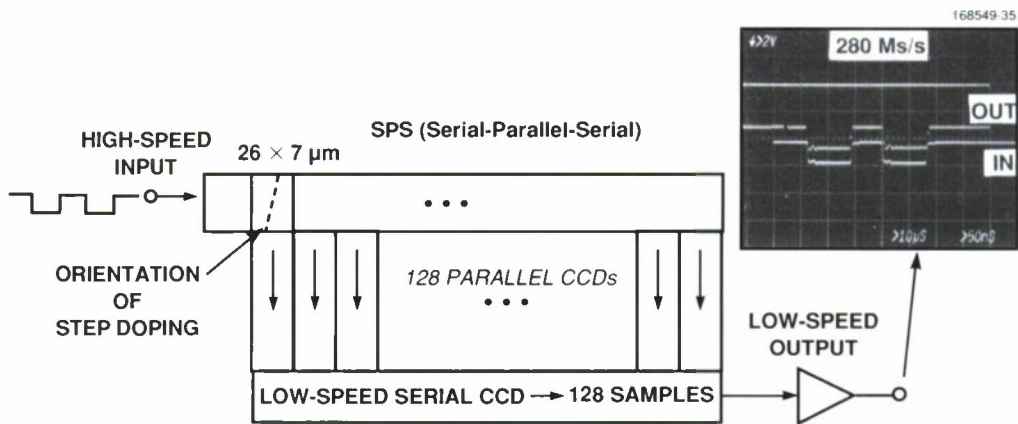


Figure 7-7. Schematic diagram illustrating the operation of the CCD analog buffer memory and the experimental results for a sampling rate of 280 MHz.

fields can be operated at very high speeds with only 5-V clocks. We have so far tested only the basic operation of the device and determined its maximum speed. Other important parameters, such as linearity and dynamic range, remain to be determined.

A.L. Lattes
S.C. Munroe
M.M. Seaver
D.B. Whitley

REFERENCES

1. D.E. Oates, A.C. Anderson, and P.M. Mankiewich, *J. Superconduct.* **3**, 251 (1990).
2. D.M. Sheen, S.M. Ali, D.E. Oates, R.S. Withers, and J.A. Kong, to be published; J. Steinbeck and J. Holtham, to be published.
3. S.M. Anlage, B.W. Langly, H.J. Snortland, E.B. Eom, T.H. Geballe, and M.R. Beasley, to be published in *J. Superconduct.* **3** (1990).
4. T.L. Hylton and M.R. Beasley, *Phys. Rev. B* **13**, 9042 (1989).
5. R.S. Withers, A.C. Anderson, J.B. Green, and S.A. Reible, *IEEE Trans. Magn.* **MAG-21**, 186 (1985).
6. D.E. Oates and A.C. Anderson, *Proc. SPIE* **1187**, 326 (1990).
7. P.M. Mankiewich, J.H. Seofield, W.J. Skoepol, R.E. Howard, A.H. Dayem, and E. Good, *Appl. Phys. Lett.* **51**, 1753 (1987).

8. W.J. Gallagher, private communication.
9. N. Newman, B.F. Cole, S.M. Garrison, K. Char, and R.C. Taber, to be published in *IEEE Trans. Magn.*
10. T. Venkatesan, private communication.
11. M.S. DiIorio, R.S. Withers, and A.C. Anderson, *IEEE Trans. Microwave Theory Tech.* **37**, 706 (1989).
12. W.G. Lyons, R.S. Withers, A.C. Anderson, R.R. Bonetti, A.E. Williams, P.M. Mankiewich, M.L. O'Malley, and R.E. Howard, presented at IEEE Device Research Conf., Santa Barbara, Calif., 25-27 June 1990.
13. W.G. Lyons, R.S. Withers, J.M. Hamm, A.C. Anderson, P.M. Mankiewich, M.L. O'Malley, and R.E. Howard, to be published in *IEEE Trans. Magn.*
14. R. Hayes and D.L. Heidtmann, *Opt. Eng.* **26**, 829 (1987).
15. Solid State Research Report, Lincoln Laboratory, MIT, 1990:2, p. 55.

